

Development and applications of methodologies for the neutronic design of the
Pebble Bed Advanced High Temperature Reactor (PB-AHTR)

by

Massimiliano Fratoni

Laurea (University of Rome “La Sapienza”) 2004
M.S. (University of California, Berkeley) 2007

A thesis submitted in partial satisfaction of the
requirements for the degree of

Doctor of Philosophy

in

Engineering - Nuclear Engineering

in the

Graduate Division

of the

University of California, Berkeley

Committee in charge:

Professor Ehud Greenspan, Chair
Professor Per F. Peterson
Professor Jasmina Vujic
Professor Joonhong Ahn
Professor Jonathan Wilkening

Fall 2008

The dissertation of Massimiliano Fratoni is approved:

Chair	_____	Date	_____
	_____	Date	_____
	_____	Date	_____
	_____	Date	_____
	_____	Date	_____

University of California, Berkeley
Fall 2008

Abstract

Development and applications of methodologies for the neutronic design of the Pebble Bed Advanced High Temperature Reactor (PB-AHTR)

by

Massimiliano Fratoni

Doctor of Philosophy in Engineering - Nuclear Engineering

University of California, Berkeley

Professor Ehud Greenspan, Chair

This study investigated the neutronic characteristics of the Pebble Bed Advanced High Temperature Reactor (PB-AHTR), a novel nuclear reactor concept that combines liquid salt (${}^7\text{LiF-BeF}_2$ —flibe) cooling and TRISO coated-particle fuel technology. The use of flibe enables operation at high power density and atmospheric pressure and improves passive decay-heat removal capabilities, but flibe, unlike conventional helium coolant, is not transparent to neutrons. The flibe occupies 40% of the PB-AHTR core volume and absorbs ~8% of the neutrons, but also acts as an effective neutron moderator.

Two novel methodologies were developed for calculating the time dependent and equilibrium core composition: (1) a simplified single pebble model that is relatively fast; (2) a full 3D core model that is accurate and flexible but computationally intensive.

A parametric analysis was performed spanning a wide range of fuel kernel diameters and graphite-to-heavy metal atom ratios to determine the attainable burnup and reactivity coefficients. Using 10% enriched uranium ~130 GWd/tHM burnup was found to be attainable, when the graphite-to-heavy metal atom ratio (C/HM) is in the range of 300 to 400. At this or smaller C/HM ratio all reactivity coefficients examined—coolant temperature, coolant small and full void, fuel temperature, and moderator temperature, were found to be negative.

The PB-AHTR performance was compared to that of alternative options for HTRs, including the helium-cooled pebble-bed reactor and prismatic fuel reactors, both gas-cooled and flibe-cooled. The attainable burnup of all designs was found to be similar. The PB-AHTR generates at least 30% more energy per pebble than the He-cooled pebble-bed reactor. Compared to LWRs the PB-AHTR requires 30% less natural uranium and 20% less separative work per unit of electricity generated.

For deep burn TRU fuel made from recycled LWR spent fuel, it was found that in a single pass through the core ~66% of the TRU can be transmuted; this burnup is slightly superior to that attainable in helium-cooled reactors.

A preliminary analysis of the modular variant for the PB-AHTR investigated the triple heterogeneity of this design and determined its performance characteristics.

Table of Contents

Table of Contents	i
List of Figures	iv
List of Tables.....	xi
Acknowledgments	xv
1. Introduction	1
1.1 Background review	2
1.1.1 The Pebble Bed Advanced High Temperature Reactor	2
1.1.2 Liquid salt cooling for nuclear reactors.....	6
1.1.3 TRISO fuel particles technology	8
1.1.4 The depletion problem in pebble bed reactors	11
1.2 Scope of the study	13
2. Models and methodologies.....	17
2.1 PB-AHTR design features.....	18
2.1.1 Integral design	21
2.1.2 Modular design.....	22
2.2 MCNP models	24
2.2.1 Materials	28
2.2.2 Temperatures and cross sections	33

2.3 Modeling of fuel heterogeneities.....	34
2.3.1 Double heterogeneity	34
2.4 Depletion methodologies.....	39
2.4.1 Infinite uniform bed method	40
2.4.2 Single pebble in equilibrium bed method	48
2.4.3 Full core method.....	56
3. Results	70
3.1 Neutronics features of the PB-AHTR	70
3.2 Attainable burnup.....	73
3.2.1 Fuel kernel diameter and C/HM.....	74
3.2.2 Power density and total core power	78
3.2.3 Spatial self-shielding effect on attainable burnup	79
3.3 Reactivity coefficients.....	86
3.3.1 SCALE model	87
3.3.2 Results	88
3.4 Summary	116
4. HTRs comparison.....	117
4.1 Helium-cooled Pebble Bed Modular Reactor	118
4.2 Prismatic fuel.....	119
4.2.1 Liquid salt cooled prismatic fuel (LS-VHTR)	122
4.2.2 Gas cooled prismatic fuel (VHTR)	124

4.3 Comparison	125
5. Deep-burn option.....	130
5.1 Deep-burn PB-AHTR.....	131
5.2 TRU transmutation in the DB-MHR.....	134
5.3 Comparison	136
6. Modular PB-AHTR	144
6.1 Triple heterogeneity	145
6.1.1 Steady-state analysis	145
6.1.2 Spatial self-shielding in the channels	151
6.2 Attainable burnup and power peaking factor	153
7. Conclusions	156
References	162
Appendix A. MOCUP	165
Appendix B. Sample inputs.....	169

List of Figures

Figure 1.1 Elevation view of the PB-AHTR integral design.....	3
Figure 1.2 Schematic of the Modular PB-AHTR system.....	5
Figure 1.3 Microscope image of a cracked TRISO particle reveals the structure of the coatings.....	9
Figure 2.1 Pebbles design.....	18
Figure 2.2 Regular pebble and annular pebble cross sections.....	19
Figure 2.3 PB-AHTR integral design vertical view.....	21
Figure 2.4 PCA vertical and horizontal views at multiple levels (Bardet, et al. 2008).	23
Figure 2.5 Horizontal view of the MPB-AHTR with seven PCA units (Bardet, et al. 2008).	24
Figure 2.6 Horizontal and vertical view of the integral PB-AHTR unit cell model. ..	25
Figure 2.7 Horizontal and vertical views of the MPB-AHTR full core model—pebbles are not shown in this figure but are explicitly modeled in MCNP.....	26
Figure 2.8 ^6Li concentration as function of time starting from initial (50 ppm ^6Li) salt composition and corresponding single pebble infinite multiplication factor with clean fuel composition.....	32
Figure 2.9 Comparison of the neutron spectrum in the fuel with initial and equilibrium salt composition.	32
Figure 2.10 Uniform bed methodology flow chart.....	47
Figure 2.11 Neutron spectrum comparison at BOL and EOL as obtained from the infinite uniform bed methodology for 10% enriched uranium (left) and TRU (right) fuels.	49
Figure 2.12 Single pebble in equilibrium bed methodology flow chart.....	51
Figure 2.13 Neutron flux amplitude in the sample pebble as a function of burnup when not constrained to be constant—425 μm fuel kernel diameter, 12.5% TRISOs packing factor, 10% enriched uranium.....	53
Figure 2.14 Normalized neutron spectrum difference between a fresh pebble when in a uniform bed and when in an equilibrium bed—425 μm fuel kernel diameter, 12.5% TRISOs packing factor, 10% enriched uranium.	54
Figure 2.15 Flow chart of the full core depletion methodology.....	63

Figure 2.16 Radial depletion zones distribution in the “3 axial + radial” scheme.	64
Figure 2.17 Effective multiplication factor evolution with iterations from a uniform clean fuel composition to the core equilibrium composition—three axial zones case.	65
Figure 2.18 Power per fuel kernel at each pass and in each zone at equilibrium—3 axial zones case.	68
Figure 2.19 Power per fuel kernel at each pass and in each zone at equilibrium—7 axial zones case.	68
Figure 2.20 Power per fuel kernel in each channel of the outer PCAs from the first to the sixth pass and in each channel of the central PCA at the seventh pass.	69
Figure 3.1 Neutron spectrum in the fuel kernels at BOL for the reference design, with and without coolant.	71
Figure 3.2 Comparison of neutron flux and F total cross section.	72
Figure 3.3 Comparison of neutron flux and total ^6Li cross section.	72
Figure 3.4 Comparison of neutron flux and ^{238}U capture cross section.	72
Figure 3.5 Attainable burnup (GWd/tHM) as a function of fuel kernel diameter and graphite-to-heavy metal atom ratio.	74
Figure 3.6 Residence time (EFPD) as a function of fuel kernel diameter and graphite-to-heavy metal atom ratio.	75
Figure 3.7 Infinite multiplication factor, fractional absorption in the fuel— f , and neutron generated per neutron absorbed in the fuel— η , as a function of graphite-to-heavy metal atom ratio for 425 μm fuel kernels.	76
Figure 3.8 Neutron spectrum at different graphite-to-heavy metal atom ratio for 425 μm fuel kernels.	76
Figure 3.9 BOL multiplication factor, fractional absorption in the fuel— f , and neutron generated per neutron absorbed in the fuel— η , as a function of kernel diameter at a constant graphite-to-heavy metal atom ratio (~ 360).	77
Figure 3.10 Local-to-peak ^{238}U effective 1-g capture cross section as a function of radial position in the kernel and kernel diameter at a constant graphite-to-heavy metal atom ratio (~ 360)—BOL, 10% enriched uranium.	77
Figure 3.11 Local specific power-to-kernel average specific power as a function of average burnup in selected kernel zones.	81
Figure 3.12 Conversion ratio as a function of kernel average burnup in selected kernel zones.	82
Figure 3.13 Zone-dependent burnup as a function of depletion time.	82

Figure 3.14 Comparison of k_{∞} as a function of depletion time for five layers and uniform kernel models.....	83
Figure 3.15 Comparison of burnup as a function of depletion time for five layers and uniform kernel models.....	84
Figure 3.16 Local specific power-to-pebble average specific power as a function of average burnup in selected pebble regions.	85
Figure 3.17 Conversion ratio as a function of kernel average burnup in selected pebble regions.....	85
Figure 3.18 Fuel temperature reactivity coefficient (pcm/K) as a function of fuel kernel diameter and graphite-to-heavy metal atom ratio.....	89
Figure 3.19 Fuel temperature reactivity coefficient as a function of pebble burnup level for selected fuel kernel diameters and ~360 graphite-to-heavy metal atom ratio.....	90
Figure 3.20 Fuel temperature reactivity coefficient as a function of pebble burnup level for selected graphite-to-heavy metal atom ratio and 425 μm fuel kernel diameter.	90
Figure 3.21 Coolant temperature reactivity coefficient (pcm/K) as a function of fuel kernel diameter and graphite-to-heavy metal atom ratio.....	91
Figure 3.22 Coolant temperature reactivity coefficient as a function of burnup for the reference design.....	92
Figure 3.23 Comparison of BOL neutrons spectrum variation when the coolant temperature is increased by 100 K and its density is reduced by 2.49%, when only the coolant void fraction is reduced and when only the temperature is increased—reference design.....	94
Figure 3.24 Fissile nuclides η as a function of neutron energy in the thermal range.	94
Figure 3.25 Burnup dependent variation of the neutrons produced per neutron absorbed in the fuel kernels when the coolant temperature is increased by 100 K and its density is reduced by 2.49%, when only the coolant void fraction is reduced and when only the temperature is increased—reference design.	95
Figure 3.26 Burnup dependent variation of neutron fraction absorbed in the fuel when the coolant temperature is increased by 100 K and its density is reduced by 2.49%, when only the coolant void fraction is reduced and when only the temperature is increased—reference design.....	95
Figure 3.27 Burnup dependent variation of the infinite multiplication when the coolant temperature is increased by 100 K and its density is reduced by 2.49%, when only the coolant void fraction is reduced and when only the temperature is increased—reference design.....	96

Figure 3.28 ^{239}Pu concentration and η variation due to coolant temperature increase as function of pebble burnup for 425 μm fuel kernel diameter and ~ 360 graphite-to-heavy metal ratio.....	96
Figure 3.29 Coolant temperature reactivity effect as function of the pebble burnup level for selected fuel kernel diameters and ~ 360 graphite-to-heavy metal atom ratio.	97
Figure 3.30 Variation of f as a function of burnup due to coolant temperature increase for selected fuel kernel diameters and constant graphite-to-heavy metal atom ratio (~ 360).	97
Figure 3.31 Variation of η as a function of burnup due to coolant temperature increase for selected fuel kernel diameters and constant graphite-to-heavy metal atom ratio (~ 360).	98
Figure 3.32 Concentration of ^{239}Pu in the kernels as a function of burnup for selected fuel kernels diameters and constant graphite-to-heavy metal atom ratio (~ 360).	98
Figure 3.33 Coolant temperature reactivity coefficient as a function of the pebble burnup level for selected graphite-to-heavy metal atom ratio and constant fuel kernel diameter (425 μm).	99
Figure 3.34 Variation of f as a function of burnup due to coolant temperature increase for selected graphite-to-heavy metal atom ratio and constant fuel kernel diameter (425 μm).	99
Figure 3.35 Variation of η as a function of burnup due to coolant temperature increase for selected graphite-to-heavy metal atom ratio and constant fuel kernel diameter (425 μm).	100
Figure 3.36 Coolant void reactivity coefficient (pcm/void%) as a function of fuel kernel diameter and graphite-to-heavy metal atom ratio.	101
Figure 3.37 Variation of the BOL neutron spectrum when the coolant density is reduced by 2.49%—reference design.	101
Figure 3.38 Coolant void reactivity coefficient as a function of the pebble burnup level for selected fuel kernels diameters and ~ 360 graphite-to-heavy metal atom ratio.	102
Figure 3.39 Variation of the fuel neutrons absorption fraction as function of the pebble burnup level due to coolant density drop for selected fuel kernels diameters and ~ 360 graphite-to-heavy metal atom ratio.	102
Figure 3.40 Variation of the number of neutrons produced per neutron absorbed in the fuel as a function of the pebble burnup level due to coolant density drop for selected fuel kernels diameters and ~ 360 graphite-to-heavy metal atom ratio. .	103
Figure 3.41 Coolant void reactivity coefficient as function of the pebble burnup level	

due to coolant density drop for selected graphite-to-heavy metal atom ratio and 425 μm fuel kernel diameter.....	104
Figure 3.42 Variation of the fuel neutrons absorption fraction as function of the pebble burnup level due to coolant density drop for selected graphite-to-heavy metal atom ratio and 425 μm fuel kernel diameter.....	104
Figure 3.43 Variation of the number of neutrons produced per neutron absorbed in the fuel as function of the pebble burnup level due to coolant density drop for selected graphite-to-heavy metal atom ratio and 425 μm fuel kernel diameter.....	105
Figure 3.44 Coolant full void reactivity coefficient (pcm/void%) as a function of fuel kernel diameter and graphite-to-heavy metal atom ratio.....	106
Figure 3.45 Variation of the BOL neutrons spectrum when the coolant is fully voided—reference design.....	106
Figure 3.46 Burnup dependent variation of the multiplication factor, fractional fuel absorption and number of neutrons generated per neutron absorbed in the fuel after the coolant is fully voided—reference design.....	107
Figure 3.47 Coolant full void reactivity coefficient as function of the pebble burnup level after coolant full voiding for selected fuel kernel diameters and ~ 360 graphite-to-heavy metal atom ratio.....	107
Figure 3.48 Coolant full void reactivity coefficient as function of the pebble burnup level after coolant full voiding for selected graphite-to-heavy metal atom ratio and 425 μm fuel kernel diameter.....	108
Figure 3.49 Moderator temperature reactivity coefficient (pcm/K) as a function of fuel kernel diameter and graphite-to-heavy metal atom ratio.....	110
Figure 3.50 Variation of the BOL neutron spectrum when the moderator temperature is increased by 100 K—reference design.....	110
Figure 3.51 Burnup dependent variation of the multiplication factor, fractional fuel absorption and number of neutrons generated per neutron absorbed in the fuel due to moderator temperature increase—reference design.....	111
Figure 3.52 Moderator temperature reactivity coefficient as a function of the pebble burnup level due to moderator temperature increase for selected fuel kernel diameters and ~ 360 graphite-to-heavy metal atom ratio.....	111
Figure 3.53 Variation of the fuel neutrons absorption fraction as a function of the pebble burnup level due to moderator temperature increase for selected fuel kernel diameters and ~ 360 graphite-to-heavy metal atom ratio.....	112
Figure 3.54 Variation of the number of neutrons produced per neutron absorbed in the fuel as function of the pebble burnup level due to moderator temperature increase for selected fuel kernel diameters and ~ 360 graphite-to-heavy metal atom ratio.....	

.....	112
Figure 3.55 Variation of the number of neutrons produced per neutron absorbed in the fuel as function of the pebble burnup level due to moderator temperature increase for selected graphite-to-heavy metal atom ratio and 425 μm fuel kernel diameters.	113
Figure 3.56 Variation of the fuel neutrons absorption fraction as function of the pebble burnup level due to moderator temperature increase for selected graphite-to-heavy metal atom ratio and 425 μm fuel kernel diameters.....	113
Figure 3.57 Variation of the number of neutrons produced per neutron absorbed in the fuel as function of the pebble burnup level due to moderator temperature increase for selected graphite-to-heavy metal atom ratio and 425 μm fuel kernel diameters.	114
Figure 3.58 Moderator and fuel temperature reactivity coefficient (pcm/K) as a function of fuel kernel diameter and graphite-to-heavy metal atom ratio.....	114
Figure 3.59 Moderator and coolant temperature reactivity coefficient (pcm/K) as a function of fuel kernel diameter and graphite-to-heavy metal atom ratio.....	115
Figure 4.1 Horizontal view of the VHTR (left) and LS-VHTR (right) core.....	120
Figure 4.2 Prismatic fuel block model.	121
Figure 4.3 Comparison of HTR designs BOL neutron spectra for C/HM 455.	127
Figure 4.4 Neutrons spectra of the maximum burnup HTR designs.	128
Figure 5.1 DB-MHR core horizontal view with five fuel element rings (Venneri 2007).	135
Figure 5.2 PB-AHTR neutrons spectrum at BOL and EOL.....	137
Figure 5.3 DB-MHR neutrons spectrum at BOL and EOL.....	138
Figure 5.4 Comparison of the conversion ratio as a function of burnup for the PB-AHTR and the DB-MHR.	138
Figure 5.5 Comparison of the ^{241}Pu effective fission cross section as a function of burnup for the PB-AHTR and the DB-MHR.....	141
Figure 5.6 Comparison of ^{241}Pu concentration in fuel kernels as a function of burnup in the PB-AHTR and the DB-MHR.	141
Figure 5.7 Comparison of spent fuel radiotoxicity per metric ton of initial TRU as a function of decay time after discharge.	142
Figure 5.8 Comparison of spent fuel decay-heat per metric ton of initial TRU as a function of decay time after discharge.	143
Figure 6.1 Horizontal cross section of a Pebble Channel Assembly (PCA).	145

Figure 6.2	BOL infinite multiplication factor as a function of graphite-to-heavy metal atom ratio in a unit cell model of the PB-AHTR modular and integral design. .	147
Figure 6.3	Comparison of the fraction of neutrons absorbed by the coolant only, and by the coolant and the PCA structure in the PB-AHTR modular design with the neutrons fraction absorbed by the coolant in the integral design.	147
Figure 6.4	Comparison of the neutron spectrum in the fuel of the PB-AHTR modular and integral designs; the integral design Case 1 features the same C/HM as the modular design, while Case 2 features the TRISO packing factor that maximizes attainable burnup.	150
Figure 6.5	Comparison of the BOL neutron spectrum in the center and in the outermost region of the channel.	152
Figure 6.6	Local kernel power-to-average kernel power ratio as a function of channel radial region and residence time.	152

List of Tables

Table 1.1 Comparison of the major design parameters for the PB-AHTR modular and integral design (Bardet, et al. 2008).	5
Table 1.2 AHTR candidate liquid salts and other nuclear reactors coolants properties ^a (Forsberg, Peterson and Kochendarfer 2008).....	7
Table 1.3 Slowing down parameters of candidates molten salts and typical nuclear reactors moderators ^a (de Zwaan 2005).	7
Table 1.4 AVR fuel performance at very high temperature (>1350 °C) and low fission product release (Pohl 2006).	10
Table 2.1 TRISO coating layers thicknesses (Kim, Taiwo and Yang 2005).	19
Table 2.2 Geometry parameters for the MPB-AHTR design.....	27
Table 2.3 Core effective multiplication factor and fractional power produced in the chute as a function of defueling chute length and composition—clean fuel 10% enriched, 425 µm diameter kernel, 35% TRISO packing factor.	27
Table 2.4 PB-AHTR core materials densities and operating temperatures.....	28
Table 2.5 Salt composition and infinite multiplication factor at different exposure times with constant fuel composition (clean fuel).....	31
Table 2.6 Pebble properties with initial and equilibrium salt composition.	33
Table 2.7 Effect of TRISO particles homogenization—clean fuel 10% enriched, 425 µm diameter kernel, 10% TRISO packing factor, 50 ppm ⁶ Li.....	36
Table 2.8 Infinite multiplication factor as a function of fuel kernel lattice structure—clean fuel 10% enriched, 425 µm diameter kernel, 10% TRISO packing factor, 50 ppm ⁶ Li.	37
Table 2.9 Infinite multiplication factor as a function of pebble lattice structure—clean fuel 10% enriched, 425 µm diameter kernel, 10% TRISO packing factor, and 50 ppm ⁶ Li.	38
Table 2.10 Sensitivity to the flux amplitude of the average pebble power and of the attainable burnup predicted by the uniform bed methodology—425 µm fuel kernel, 10% packing factor.	48
Table 2.11 Sensitivity to the flux amplitude the equilibrium infinite multiplication factor and of the attainable burnup predicted by the single pebble in equilibrium bed methodology—425 µm fuel kernel, 12.5% TRISO packing factor.....	52
Table 2.12 Infinite multiplication factor as a function the equilibrium bed	

size—425 μm fuel kernel diameter, 12.5% TRISOs packing factor, 10% enriched uranium.....	53
Table 2.13 Uniform bed and single pebble in uniform bed methodologies prediction comparison for enriched uranium—425 μm kernel diameter, 12.5% TRISOs packing factor.	55
Table 2.14 Uniform bed and single pebble in uniform bed methodologies prediction comparison for TRU—200 μm kernel diameter, 11% TRISOs packing factor. ...	55
Table 2.15 Neutrons spectrum in the fuel of a pebble near EOL (640 GWd/tHM) when calculated using the uniform bed and the equilibrium bed methodologies; 200 μm kernel diameter, 11% TRISOs packing factor.	55
Table 2.16 Comparison of selected characteristics obtained using the three core subdivision schemes.	66
Table 2.17. Burnup results as a function of total residence time—3 axial zones case.	67
Table 3.1 Fractional neutron absorption in the unit cell components at BOL for the reference design.	73
Table 3.2 BOL kernel average effective 1-g cross sections for selected kernels diameter—360 C/HM graphite-to-heavy metal atom ratio, 10% enriched uranium.	78
Table 3.3 Attainable burnup as function of core power density—reference pebble design.....	79
Table 3.4 Attainable burnup as function of total core power—reference pebble design, 10.2 MW/m ³	79
Table 3.5 BOL pebble properties as a function of kernel layer.....	81
Table 3.6 EOL fuel isotopic composition in each kernel layer (atoms/b-cm).....	83
Table 3.7 EOL fuel isotopic composition in each kernel layer (atoms/b-cm).....	86
Table 3.8 Properties of selected design that for a given fuel kernel diameter, maximize the burnup while maintaining all the reactivity coefficients negative.	116
Table 4.1 PBMR attainable burnup as a function of the TRISO particles packing factor.....	119
Table 4.2 LS-VHTR and VHTR models.	122
Table 4.3 LS-VHTR attainable burnup for selected TRISO particles packing factors for a three-batch refueling scheme.	123
Table 4.4 VHTR attainable burnup for selected TRISO particles packing factors for three-batch refueling scheme.....	124

Table 4.5 Comparison of HTRs designs BOL properties for C/HM 455.....	126
Table 4.6 Comparison of the maximum burnup offered by the HTR design concept examined.....	127
Table 4.7 Comparison of PB-AHTR performance with the PBMR maximum burnup and optimized designs.	129
Table 5.1 Initial TRU composition from LWR spent fuel after 50 GWd/tHM burnup, 5 years cooling and complete removal of U, Cm and fission products (Venneri 2007).....	131
Table 5.2 Transmutation properties of the PB-AHTR as a function of TRISO particles packing factor for 200 μm diameter fuel kernels and initial HM load TRU from LWRs spent fuel.	133
Table 5.3 Core average reactivity coefficients in the deep-burn PB-AHTR for selected graphite-to-heavy metal atom ratio.....	134
Table 5.4 Transmutation properties of the DB-MHR as a function of TRISO particles packing factor for 200 μm diameter fuel kernels and initial HM load TRU from LWR spent fuel.....	136
Table 5.5 PB-AHTR and DB-MHR transmutation properties.	137
Table 5.6 Comparison of feed actinides consumption (%) in the PB-AHTR and in the DB-MHR.	139
Table 5.7 Comparison of the heavy metal composition at the EOL in the PB-AHTR and in the DB-MHR fuel.	140
Table 6.1 Comparison of selected BOL neutronic properties for the PB-AHTR modular and integral design; the integral design Case 1 features same C/HM as the modular design, while Case 2 features the TRISO packing factor that maximizes attainable burnup.	149
Table 6.2 Comparison of neutron absorption in the core components at BOL for the PB-AHTR modular and integral design; the integral design Case 1 features same C/HM as the modular design, while Case 2 features the packing factor that maximizes attainable burnup.	150
Table 6.3 BOL pebbles properties as a function of the channels radial region.	151
Table 6.4 MPB-AHTR properties for selected TRISO particle packing factor—325 μm kernel diameter, 19.9% enrichment, 30 MW/m ³	154
Table 6.5 MPB-AHTR properties for selected TRISO particles packing factor—225 μm kernel diameter, 19.9% enrichment, 30 MW/m ³	155
Table 7.1 Performance comparison of the integral PB-AHTR design with the LWR and the optimized PBMR.	160

Acknowledgments

My most sincere thanks to Professor Ehud Greenspan for all his advises that I will carry in my career as the most precious things. Thanks to Professor Per Peterson for supporting my research. A warm thank to the Nuclear Engineering Department at UC Berkeley, in particular Chair Professor Jasmina Vujic and Lisa Zemelman for creating an extraordinary environment.

Thanks to my parents for their endless support; hoping that this achievement might be a little solace for all the times they missed me.

1. Introduction

The Very High Temperature Reactor (VHTR) is the leading candidate for the Next Generation Nuclear Plant (NGNP). Among the innovative features that it will introduce are the capability to deliver heat at high temperature for multiple industrial applications beyond the classical electricity production (refineries, oil recovery, biomass conversion, hydrogen production), as well as passive safety, and high efficiency. However, the attractiveness of the VHTR is negatively affected by the relatively low power density at which it operates and by the use of a low heat capacity, high pressure coolant—helium—that requires very large core components with a negative impact on costs. The Advanced High Temperature Reactor (AHTR), proposed recently (Forsberg, Peterson and Pickard 2003), aims to overcome those VHTR drawbacks. This concept combines the HTR fuel and moderator designs with liquid salt cooling, following the realization that the better heat capacity and heat transport characteristics of molten salts, as compared to helium, could allow to increase operational power density, to improve efficiency (Brayton cycle), to enhance

passive safety, and to reduce core dimensions for an overall cost reduction. The Pebble Bed-Advanced High Temperature Reactor (PB-AHTR) is the pebble bed variant of this novel concept (de Zwaan 2005).

This Chapter introduces the main features of the PB-AHTR design and presents the two basic technologies it relies on: liquid salt coolants and coated-particles fuel. This is followed by a review of the computational tools available for the neutronic analysis of pebble system. The last section defines the scope of the project and the structure of this manuscript.

1.1 Background review

1.1.1 The Pebble Bed Advanced High Temperature Reactor

The PB-AHTR was developed at the University of California, Berkeley in collaboration with Oak Ridge National Laboratory. It features pebble fuel design filled with TRISO coated fuel particles dispersed in a graphite matrix and utilizes flibe (${}^7\text{LiF-BeF}_2$) as a coolant. The pebble recirculation motion is upward, in contrast with the downward direction in the helium-cooled pebble bed reactor, because pebbles are positively buoyant in liquid salt. The base design studied here (Figure 1.1) is a 2,400 MWth unit that operates with an average core power density of 10.2 MW/m^3 —about 50% greater than the typical power density of a modular helium-cooled reactor (Griveau, et al. 2007). A low-temperature and a

high-temperature design variant are considered. The low temperature variant has core inlet and outlet temperatures of 600 °C and ~710 °C respectively, allowing it to use available, ASME Code qualified materials, like Hastelloy N, for structural components. The primary loop is coupled to a multiple reheat helium Brayton cycle and the net power conversion efficiency reaches 46%, for a net electrical output of 1,100 MWe (Griveau, et al. 2007). The high-temperature PB-AHTR variant has a core outlet temperature between 750 °C and 1000 °C, and is optimized for the production of hydrogen, but its feasibility depends on developing and qualifying materials to operate at higher temperature.

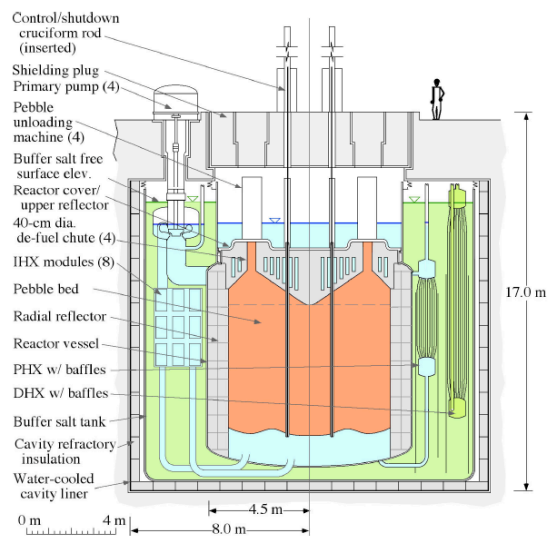


Figure 1.1 Elevation view of the PB-AHTR integral design.

A series of studies addressed key viability issues for the PB-AHTR. The Pebble Recirculation Experiment (PREX) confirmed the viability of pebble recirculation in liquid salts (Bardet, An, et al. 2007). The same experiment verified the feasibility of

injection and extraction of buoyant pebbles, measured the packing density of the bed and pressure losses, and observed pebble landing dynamics and bed formation. Modeling of transients such as loss of forced cooling (LOFC) demonstrated that the natural circulation of liquid salts provides a highly effective passive decay heat removal, allowing the PB-AHTR to operate with power density in the 20-30 MW/m³ range, much higher than in gas-cooled systems, while maintaining passive safety (Griveau, et al. 2007).

More recently a modular design has been proposed for the PB-AHTR (Figure 1.2). The core in this case is composed of hexagonal graphite blocks, called PCAs (Pebble Channels Assemblies) each containing 18 or 19 channels through which pebbles and coolant flow. The baseline design features seven PCAs and total core power of 900 MWth. The core power density was increased to 20-30 MW/m³ in view of the results obtained for the integral design. The Modular PB-AHTR (MPB-AHTR) operates at 50% greater power and has the same 46% power conversion efficiency as the 600 MWth GT-MHR, but with a low-pressure vessel that is one-tenth the volume of the GT-MHR vessel (Bardet, et al. 2008). Table 1.1 compares the main design parameters for the integral and the modular PB-AHTR designs. The MPB-AHTR utilizes smaller pebbles that allow it to operate at greater power density while maintaining the same temperature difference across the pebble.

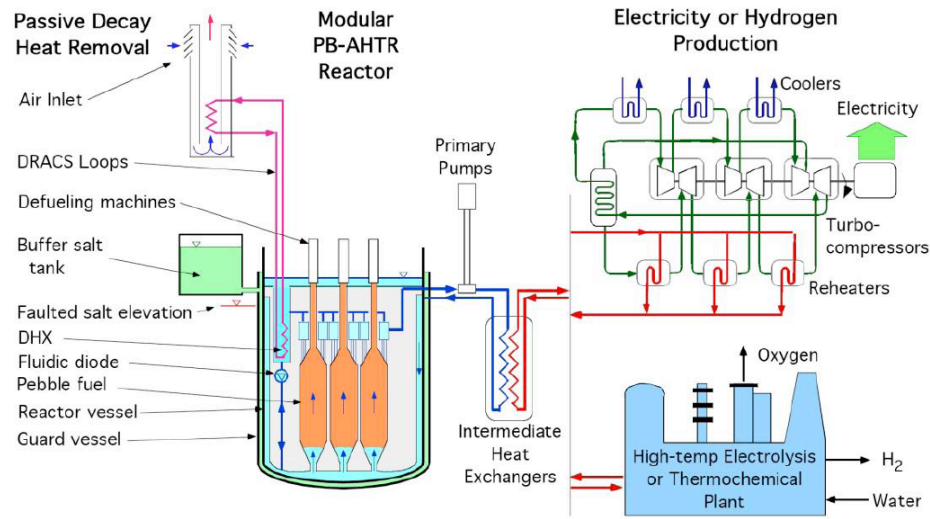


Figure 1.2 Schematic of the Modular PB-AHTR system.

Table 1.1 Comparison of the major design parameters for the PB-AHTR modular and integral design (Bardet, et al. 2008).

Parameter	Modular	Integral
Pebble diameter (cm)	3.0	6.0
Thermal power (MWth)	900	2,400
Average core power density (MW/m ³)	30	10.3
Number of flow channels	127	1
Diameter of flow channels (m)	0.198	6.70
Average height of core (m)	3.20	6.61
Core inlet/outlet temperature (°C)	600/704	600/704
Coolant mass flow rate (kg/s)	3630	9670
Coolant fraction bypassing core	0.2	0.2
Average coolant flow velocity (m/s)	0.38	0.14
Core pressure drop (kPa)	440	73
Core (only) pumping power (kW)	1,200	514
Core (only) specific pumping power (kW/MWth)	1.30	0.21

1.1.2 Liquid salt cooling for nuclear reactors

Studies on cooling nuclear reactors with liquid salt have been carried since the beginning of the nuclear technology development, in particular in the Aircraft Propulsion Project and the Molten Salt Reactor Experiment. Numerous potential liquid salt candidates are being considered for the AHTR and their properties are given in Table 1.2 (Forsberg, Peterson and Kochendarfer 2008). All candidates are fluoride salts, no chloride salts are considered because they are highly corrosive, have high thermal neutron absorption cross section and generate long-lived activation products (^{36}Cl). The mixtures of constituents were determined to optimize the final salt physical properties. All candidate coolants have a melting point between 300 and 500 °C and an atmospheric boiling point above 1,300 °C and, therefore, do not require pressurization. Salts containing lithium are enriched in ^7Li to reduce neutron absorption in the coolant. All these liquid salts are optically transparent.

Flibe ($^7\text{LiF-BeF}_2$) is the preferred liquid salt coolant, both for its high volumetric heat capacity and for its neutronics properties. The light constituents of flibe make it a good neutron moderator (Table 1.3) and in case of coolant voiding accidents the consequent reduced moderation effect can compensate for the reduced absorption effect if the core is designed to be sufficiently under-moderated (a sufficiently low ratio of carbon-to-heavy metal) (de Zwaan 2005) (Clarno and Gehin 2006) resulting in an overall negative reactivity effect.

Table 1.2 AHTR candidate liquid salts and other nuclear reactors coolants properties^a
(Forsberg, Peterson and Kochendarfer 2008).

Coolant (mole%)	T _{melt} (°C)	T _{boil} (°C)	ρ (kg/m ³)	C _p (kJ/kg-°C)	ρC _p (kJ/m ³ -°C)	k (W/m-°C)	ν (10 ⁶ m ² /s)
LiF-BeF ₂ (66-34)	459	1,430	1,940	2.42	4,670	1.0	2.9
NaF-ZrF ₄ (59.5-40.5)	500	1,290	3,140	1.17	3,670	0.49	2.6
LiF-NaF-ZrF ₄ (26-37-37)	436	-	2,790	1.25	3,500	0.53	-
LiF-NaF-BeF ₂ (31-31-38)	315	1,400	2,000	2.04	4,080	1.0	2.5
NaF-NaBF ₄ (8-92)	385	700	1,750	1.51	2,640	0.5	0.5
Na	97.8	883	820	1.27	1,040	62	0.12
Pb	328	1,750	10,540	0.16	1,700	16	0.13
He (7.5 MPa)	-	-	3.8	5.2	20	0.29	11.0
Water (7.5 MPa)	0	290	732	5.5	4,040	0.56	0.13

^a Salt properties are given at 700 °C and 1 atm; NaF-ZrF₄ conductivity is estimated, not measured; the NaF-NaBF₄ must be pressurized above 700 °C; sodium properties are at 550 °C; pressurized water properties are at 290 °C; key: ρ density; C_p specific heat; k thermal conductivity; ν viscosity.

Table 1.3 Slowing down parameters of candidates molten salts and typical nuclear reactors moderators^a (de Zwaan 2005).

Moderator	ξ	ξΣ _s /Σ _a
H ₂ O	0.920	71
C	0.158	1,437
He	0.425	83
LiF-BeF ₂	0.1046	83
NaF-ZrF ₄	0.0809	18
NaF-NaBF ₄	0.1154	23
LiF-NaF-ZrF ₄	0.0784	8.3

^a Key: ξ average neutron lethargy gain per collision;
Σ_s macroscopic elastic scattering cross section;
Σ_a macroscopic absorption cross section.

Flibe has excellent material compatibility and low corrosion rates with nickel alloys and graphite, if maintained very clean. Its activation products have very short half-lives and their radiation levels are low. Disadvantages of flibe are: it is expensive because lithium must be enriched; it contains beryllium that is chemically toxic and requires a monitoring and control system that is integrated with the system for monitoring and control of radioactive contamination; it melts at a high temperature and overcooling transients must be prevented so that all the core components are always maintained above that temperature.

1.1.3 TRISO fuel particles technology

All modern HTRs utilize TRISO fuel particles (Figure 1.3) dispersed in a graphite matrix to form fuel compacts (cylinders) in the prismatic fuel designs or spheres in the pebble bed designs. The term TRISO refers to a tristructural-isotropic particle consisting of a microsphere (kernel) made of fuel material encapsulated by a series of four chemical vapor deposition coatings to form a miniature pressure vessel preventing fission products release.

The fuel kernel can be composed of different materials, either fissile or fertile, in the form of oxides, carbides, or oxy-carbides. The inner coating is the buffer layer; it consists of high porosity carbon, and has the function to attenuate fission recoils, provide adequate void volume to contain fission gases, and accommodate dimensional changes due to kernel swelling and coatings contraction.

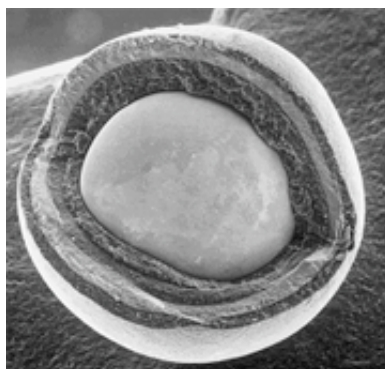


Figure 1.3 Microscope image of a cracked TRISO particle reveals the structure of the coatings.

The buffer is enclosed by the inner isotropic pyrocarbon layer (IPyC), high density carbon that provides structural integrity as internal pressure increases, protects the SiC layer from lanthanides and palladium chemical attack, and provides impermeability to chlorine compounds during deposition of the SiC layer. The SiC is the third coating and functions as the main pressure vessel against internal pressure from fission gases and provides a diffusion barrier for metallic fission products. The last layer, the outer isotropic pyrocarbon layer (OPyC), is again a high density carbon coating with multiple functions: it provides added structural support to the SiC layer; shrinks under irradiation relieving part of the tensile stress on the SiC; creates an additional barrier to gaseous fission product release in case of SiC failure; and provides bonding surface for the graphite matrix (Kovacs, Bongartz and Goodin 1983). The fuel kernel itself, besides containing the fissioning material, is the first diffusive barrier to fission gases release and its chemical form is very important. Carbide fuels

release lanthanide fission products that can react with the SiC layer, whereas oxide fuels bind lanthanides with the free oxygen released after fissions to form stable compounds that do not migrate from the kernel. On the other end, oxide kernels react with carbon to form CO gas, which contributes to internal pressure build up, whereas carbide kernels do not (M. G. Izenson 1987). Oxy-carbide kernels, instead, were found effective for reducing the kernel migration effect that is undesirable because the decentralization of the fuel kernel highly increases the particle failure probability (M. G. Izenson 1987).

Irradiation tests performed at the AVR pebble-bed high-temperature gas-cooled reactor (HTGR) in Juelich, Germany, which operated from 1967 to 1988, showed an excellent fission product retention under severe conditions (Table 1.4)—coolant temperature $>1280^{\circ}\text{C}$, fuel temperature $>1350^{\circ}\text{C}$, average discharge burnup $\sim 20\%$ fima (Fraction of Initial Metal Atoms) (Pohl 2006).

Table 1.4 AVR fuel performance at very high temperature ($>1350^{\circ}\text{C}$) and low fission product release (Pohl 2006).

Fuel	Coating	Burnup
HEU/Thorium – (U,Th)O ₂	BISO ^a	18.2% fima/166 GWd/tHM
HEU/Thorium – (U,Th)O ₂	TRISO	$\sim 16\%$ fima/ ~ 150 GWd/tHM
HEU – UCO, UC ₂	TRISO	77% fima, 690 GWd/tHM
LEU (10%) – UO ₂	TRISO	Average 8.5%, 76 GWd/tHM Max 10% fima, 89GWd/tHM
LEU (17%) – UO ₂	TRISO	Average 11%, 98 GWd/tHM Max 14% fima, 125 GWd/tHM

^a BISO is a simpler fuel particle design with only a single pyrocarbon layer surrounding the buffer; BISO particles have been abandoned in favor of better performing TRISO particles.

1.1.4 The depletion problem in pebble bed reactors

Depletion analysis for pebble bed type reactors needs to account simultaneously for the movement of the fuel and its composition changes. The problem has been studied for a long time and already in 1976 Luigi Massimo defined the basic equation that governs the changing fuel composition coupled to the pebble movement (Massimo 1976). Massimo first recognized that “in any volume element of the core all burnup stages of the fuel are represented and, because of the small size of the fuel elements, the neutron spectrum is determined by the average composition.” For a pebble he proposed to modify the general burnup equation by introducing a convection term to represent the fuel movement, that, if the fuel moves only in the axial direction, is:

$$\text{Equation 1.1} \quad \frac{\partial N_i}{\partial t} + \frac{\partial N_i}{\partial z} v = \phi \sum_{k=1}^m \alpha_{k \rightarrow i} N_k \sigma_k^{abs} + \sum_{k=1}^m \beta_{k \rightarrow i} \lambda_k N_k - \lambda_i N_i - \phi N_i \sigma_i^{abs}$$

where $N_i = N_i(x, y, z, t)$ is the atomic concentration of isotope i , $v = v(z, t)$ the pebble axial speed, $\phi = \phi(x, y, z, t)$ the neutron flux, λ the decay constant, σ_{abs} the total absorption cross section, $\alpha_{k \rightarrow i}$ the probability that an absorption reaction by nuclide k generates nuclide i , and $\beta_{k \rightarrow i}$ the probability that nuclide k decays to nuclide i . The assumption of axial pebble motion is valid for flow in areas of the core with constant cross sectional area, because the pebble motion is plug flow. The main difficult in this approach is to

know the boundary conditions $N_i(0)$ and $N_i(H)$, where H is the height of the core, because the composition of the discharged pebble is not known.

Multiple solutions were proposed for this problem during the years, but here we limit the discussion to those approaches that are applied in the mostly used codes for pebble bed reactors analysis: VSOP and PEBBED.

The VSOP (Very Superior Old Programs) code, widely used for pebble bed reactors analysis, solves the problem tracking batches of pebbles and assuming that they reside for a certain time in successive zones of the core, moving discontinuously from one zone to the next, to eventually reach an equilibrium core (Teuchert, Hansen and Haas 1980). A 2D multigroup finite-difference diffusion equation solver, CITATION, determines the flux in each zone, but this solver is obsolete and slow compared to modern tools (it was called “old” already in 1980!).

PEBBED is a code suite under development at Idaho National Laboratory for the design and analysis of pebble bed high temperature reactor cores (Gougar 2006). Starting from an all-fresh fuel core, a spatial flux distribution is computed and applied for depletion calculations. At each pass through the core the pebbles composition is updated until the burnup reaches the limit value. At this point the new core-wise burnup distribution can be reconstructed by averaging the burnup of the pebbles that cross each predefined constant flux zone. The procedure is iterated until the spatial flux distribution and the burnup at the entry plane of the core reach equilibrium. The original version of PEBBED (Terry 2001) implements some advanced features like

complex recirculation schemes, ex-core nuclides decay, variable mesh-spacing approach, and capability of determining temperature distribution applying a 1D conduction model. At the same time it has many embedded limits: the flux is determined by a finite difference multigroup (eight groups only) diffusion solver, to which cross sections are provided as an external input, without accounting for variation of the cross sections due to variation in temperature and burnup level; only 30 isotopes are depleted, and non-depletable isotopes include only ^{12}C , ^{16}O , and ^{28}Si ; the coolant—helium—is treated as void with cross sections set to zero and a diffusion coefficient computed from the transport theory. At the time the PB-AHTR project started, a series of improvement were under development for PEBBED (Gougar 2006), in particular the introduction of modules to replace constant cross sections with core conditions-dependent cross sections. Even if these more advanced tools would have been available, the applicability of PEBBED to liquid salt cooled system would have to be proved.

Many other deterministic neutronic codes do not provide the capability to treat pebble bed systems, in most of the cases not even for steady state analysis, because not those codes are not capable of accounting for the double heterogeneity effect.

1.2 Scope of the study

This study investigated the neutronic properties of the PB-AHTR, in particular to determine what burnup can be attained in this novel design under the constraint of

maintaining negative fuel and coolant temperature reactivity feedback.

The project was divided into two main parts. The first was dedicated to the development of methodologies applicable to the depletion analysis of pebble bed type reactors. These methods rely on a stochastic code (MCNP) to guarantee high fidelity geometry modeling to well represent the double heterogeneity of the TRISO particles fueled core and to overcome the limited applicability to gas-cooled reactors of currently available pebble bed depletion codes. Furthermore, coupling MCNP with a depletion module enables to automatically account for the cross section changes with burnup.

The methodology development effort was split into two parts. First, we developed a simplified model, capable of preserving the system physical properties and delivering results in a reasonable computational time. Then we focused on a more complex model that considered a full 3D core, capable of including multiple phenomena, but computationally intensive. The simplified model is instrumental for the parametric analysis, in which it was necessary to scan a large number of design parameter combinations. The detailed model, instead, is applied to the design optimization.

The second part of the project focused on the application of the developed tools and results analysis. Beside the attainable burnup, a thorough study of the reactivity feedback mechanisms was carried out. A major concern for the PB-AHTR was to verify the possibility to achieve a negative coolant temperature reactivity coefficient.

In fact, the coolant in a random packed pebble bed occupies 40% of the core volume and flibe is not transparent to neutrons as would be helium, but it is rather an absorber; when the coolant temperature increases, its density and therefore its neutrons absorption decreases causing a positive reactivity feedback. The reactivity coefficient analysis was intended to verify that other mechanism (e.g., neutron moderation) would intervene to reverse the coolant temperature feedback.

The base design fuel is 10% enriched uranium, but the possibility of incinerating TRU from LWRs was also examined. The analysis compares the performance of the PB-AHTR to that of design alternatives for HTRs that feature either pebbles or prismatic fuel, and gas or liquid salt coolant.

The last part of the project was dedicated to studying the modular variant of PB-AHTR. The same tools developed for the integral design were applied with minimum modifications, proving their high flexibility. The analysis of the MPB-AHTR focused on the evaluation of the effects deriving from the third level of heterogeneity introduced in this design concept (coated-particles, pebbles, channels) and on the estimation of fuel kernel power peaking factors.

This manuscript is organized as follows: after the introduction in Chapter 1, Chapter 2 describes each system in detail and illustrates the modeling process together with the theoretical bases and computer code implementation of the proposed methodologies; Chapter 3 analyzes the results obtained for the integral design's attainable burnup and reactivity coefficients; Chapter 4 compares various HTRs

designs in terms of maximum attainable burnup; Chapter 5 investigates the possibility of fueling the PB-AHTR with TRU from LWRs and compares the heavy metal (HM) incineration with that attained in gas-cooled systems; Chapter 6 presents preliminary results for the MPB-AHTR; and Chapter 7 summarizes the achievements and recommends future developments for the project.

2. Models and methodologies

Analysis of the PB-AHTR was carried out using two primary simulation tools. The neutronic code MCNP5 Version 1.40 (X-5 Monte Carlo Team 2003) was applied for steady-state analysis, while the MCNP-ORIGEN2 coupling program MOCUP (Moore, et al. 1995), either directly or after proper modifications, was used for depletion analysis. This Chapter describes in detail the PB-AHTR's design features, for both the integral and the modular designs, and illustrates how these features were represented in the MCNP simulation models. In particular the materials, temperature, and geometry approximations are discussed.

The approaches proposed for depletion analysis of a pebble bed system are then illustrated. Three different methodologies were developed based on different levels of sophistication. Theoretical bases and implementation with available computer tools are presented. These methodologies are compared, and their limits and advantages are discussed.

2.1 PB-AHTR design features

The PB-AHTR is a pebble reactor that combines liquid salt cooling and TRISO particle fuel technology. The coolant selected (Section 1.1.2) is LiF-BeF₂, commonly referred to as flibe. The TRISO particles (Section 1.1.3) are randomly dispersed in a graphite matrix that is enclosed in a hard graphite shell (Figure 2.1).

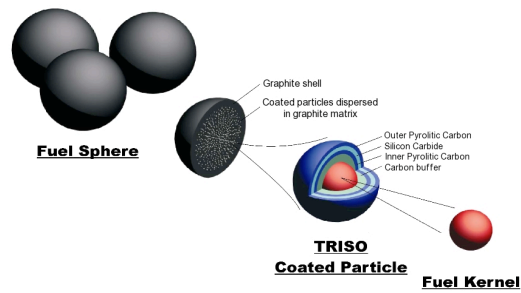


Figure 2.1 Pebbles design.

Literature offers different information on the design of TRISO particles, in particular concerning the dimensions of the coating layers. Table 2.1 reports the thickness of each of the coating layers as adopted for this project. Since the fuel kernel diameter and the number of kernels per pebble are considered design parameters, the conclusions of this study are not affected by the coatings thicknesses in the range that is considered practical.

Variations on the pebble design were also considered. In the PB-AHTR, the center of the pebble contains an inert, low-density graphite kernel that is used to adjust the buoyancy of the pebble (Figure 2.2). Referred to as an “annular” pebble, this design also reduces the temperature drop through the fuel region, which broadens the

range of possible power densities (Bardet, et al. 2008).

Table 2.1 TRISO coating layers thicknesses (Kim, Taiwo and Yang 2005).

Layer	Thickness (μm)
Buffer	100
In PyC	35
SiC	35
Out PyC	35

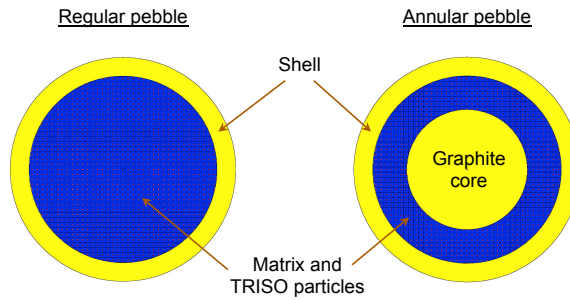


Figure 2.2 Regular pebble and annular pebble cross sections.

In the PB-AHTR pebbles are inserted from the bottom of the core and extracted from the top. The average pebble density must be such that it floats on the salt; in this way the buoyancy force, and the hydrodynamic forces of the upward coolant flow drag the pebbles upwards. The design requirement for the pebble-to-salt density ratio is 0.84 at normal operating conditions, the density ratio matching the ratio of polyethylene to water used in scaled pebble recirculation experiments (Bardet, et al. 2008). The coolant enters the core at 600 °C and leaves at 704 °C (Bardet, et al. 2008); its density at the average core temperature (655 °C) is 1.96 kg/m³ that means the

average pebble density must be 1.65 kg/m^3 .

At the core exit pebbles converge through a conic region into narrow and long channels, called defueling chutes. At the end of those, pebbles are removed by defueling machines and are tested to measure ^{137}Cs content in order to estimate their burnup level. If this is above a pre-set threshold value they are discarded and replaced by a fresh pebble; otherwise they are re-circulated into the core. The threshold burnup value is selected so that the reactor operates with sufficient excess reactivity at 100% power to accommodate the xenon transient associated with a power drop to 40% power. Under normal operation, control rods in the outer radial reflector control the reactor power.

Pebbles motion is mainly vertical as horizontal motion is very limited (Bardet, Franklin, et al. 2007), so radial mixing happens mainly when pebbles are reinserted, where they land randomly on the bottom of the pebble bed, or when channeled into the defueling chutes. The vertical speed only depends on the position of the pebble along the axis of the core and not on its radial position, because the pebbles move in slug flow in regions of constant cross sectional area, sliding along the channel wall. The pebbles near the wall have unordered packing that increases the relative permeability and enhances coolant flow near the wall. The wall-effect on the pebbles packing fraction is detectable only within three pebble's diameters distance from the wall and negligible for large diameter cores (Cogliati and Ougouag 2006).

Features specific to the integral and to the modular design are discussed in the

next two sections.

2.1.1 Integral design

The integral design (Figure 2.3) features 6.0 cm diameter pebbles with a 0.5 cm thick shell. Potentially both regular and annular pebbles are suitable, but in this project only regular pebbles were examined. The fuel pebbles distribute randomly in the core to form a bed; the random packing limits the volume fraction of the core occupied by the pebbles to 60% as confirmed experimentally in the Pebble Recirculation Experiment (PREX) (Bardet, Franklin, et al. 2007).

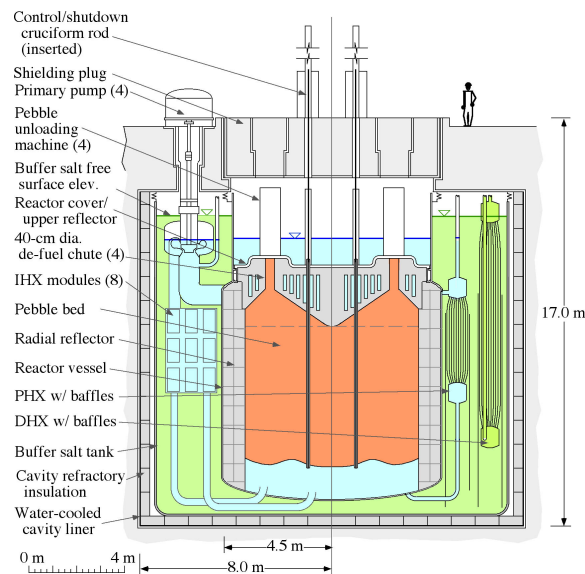


Figure 2.3 PB-AHTR integral design vertical view.

The power density was set at 10.2 MW/m^3 and the total core power at

2,400 MWth. The core is cylindrical and the dimensions—6.8 m diameter and 6.4 m active length—are dictated by the power assumptions and by imposing a height-to-diameter ratio of 0.94 to minimize neutrons leakage probability. The core contains about 1.25 million pebbles.

2.1.2 Modular design

The PB-AHTR modular design (Bardet, et al. 2008) is envisioned to make use of small annular pebbles—3 cm outer diameter, 0.5 cm thick shell, and an approximately 1.6 cm diameter central graphite kernel. The core is composed of hexagonal graphite blocks—125 cm side-to-side distance—pitched with 18 or 19 channels—19.8 cm diameter—through which pebbles flow. These structures are called Pebbles Channel Assemblies (PCAs) and are illustrated in Figure 2.4. The pebbles are inserted at the bottom of each PCA where they accumulate in a plenum before being directed into channels. At the exit of those channels, pebbles are collected in another plenum that closes towards a defueling chute. Each PCA is equipped with its own insertion and defueling chute. The channel section is 220 cm long, the lower plenum is 50 cm and the upper plenum 89 cm, for a total 359 cm active length. In this length each PCA contains about 0.5 million pebbles. The use of PCAs makes the design highly modular and multiple configurations can be envisioned by varying the number of PCAs. This project focused on a 900 MWth unit composed of seven modules (Figure 2.5).

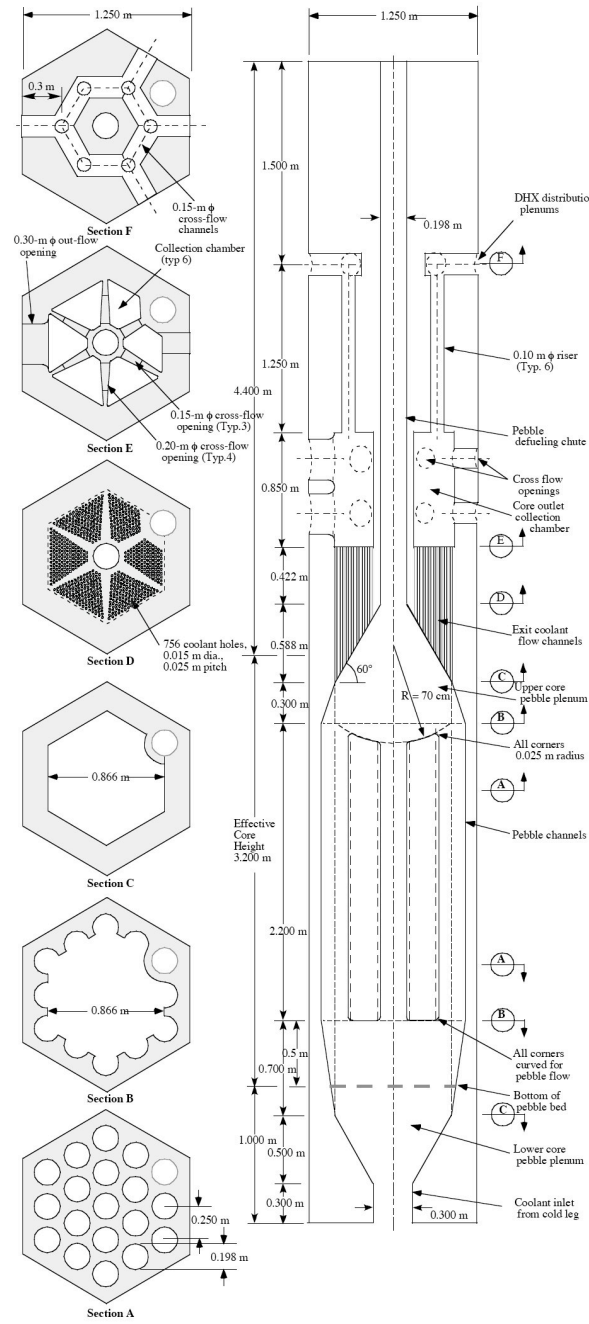


Figure 2.4 PCA vertical and horizontal views at multiple levels (Bardet, et al. 2008).

In all PCAs but the central PCA, one channel is filled with coolant only to allow insertion of the shutdown rods. An independent control/shutdown system utilizes 30 channels located in the outer reflector. Beyond the reflector, the core is contained in a 5 cm thick Alloy 800H vessel with Hastelloy N cladding for a total of 6 m outer diameter. The bed packing factor in the channels is 55% as measured experimentally (Bardet, et al. 2008). The average power density is set at 30 MW/m³.

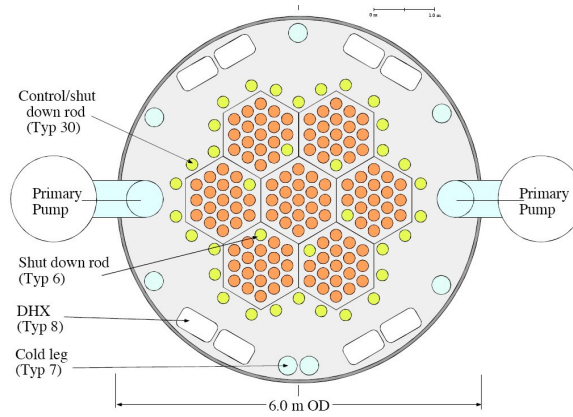


Figure 2.5 Horizontal view of the MPB-AHTR with seven PCA units (Bardet, et al. 2008).

2.2 MCNP models

The designs described above were simulated with the MCNP computer code. We used both unit cell and full core models, and we always modeled explicitly every pebble in the core and every kernel in the pebbles.

The unit cell model chosen for the integral design consists of a single pebble enclosed in a hexagonal prism of flibe and dimensioned so that the pebble volume

fraction corresponds to the correct bed packing factor (Figure 2.6).

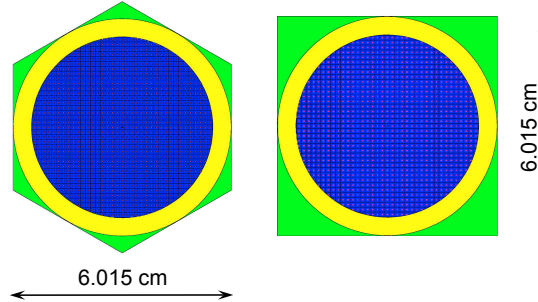


Figure 2.6 Horizontal and vertical view of the integral PB-AHTR unit cell model.

The full core model is described as a cylindrical core filled with pebbles arranged in a hexagonal lattice over parallel planes. Conic formations at the bottom of the core and exit cones are not explicitly modeled, but the cylinder active length was determined conserving the number of pebbles. The core is surrounded by a 100 cm thick graphite radial reflector, while axially the model is completed by: a 100 cm thick salt plenum at the bottom filled with flibe at inlet conditions followed by 30 cm graphite layer below the flibe; a 80 cm thick region above the pebbles modeled as a uniform mix of graphite (85 vol%) and coolant at the outlet conditions (15 vol%).

For the analysis of the modular design a full core model was exclusively applied. The MCNP replica is illustrated in Figure 2.7. Compared to the actual design (Figure 2.4) some nuances are eliminated (for example the channels are modeled all with same length instead of progressively shorter towards the center of the PCA). These geometry simplifications are not expected to affect the conclusions of this study. The shutdown/control systems channels are included in the model and filled with flibe.

Control and shutdown rods are assumed fully withdrawn unless differently specified. The region around the upper plenum embeds exit coolant flow channels and in MCNP was modeled as a uniform zone made of graphite (84 vol%) and salt (16 vol%) at the outlet conditions. Table 2.2 summarizes the MPB-AHTR design components dimensions.

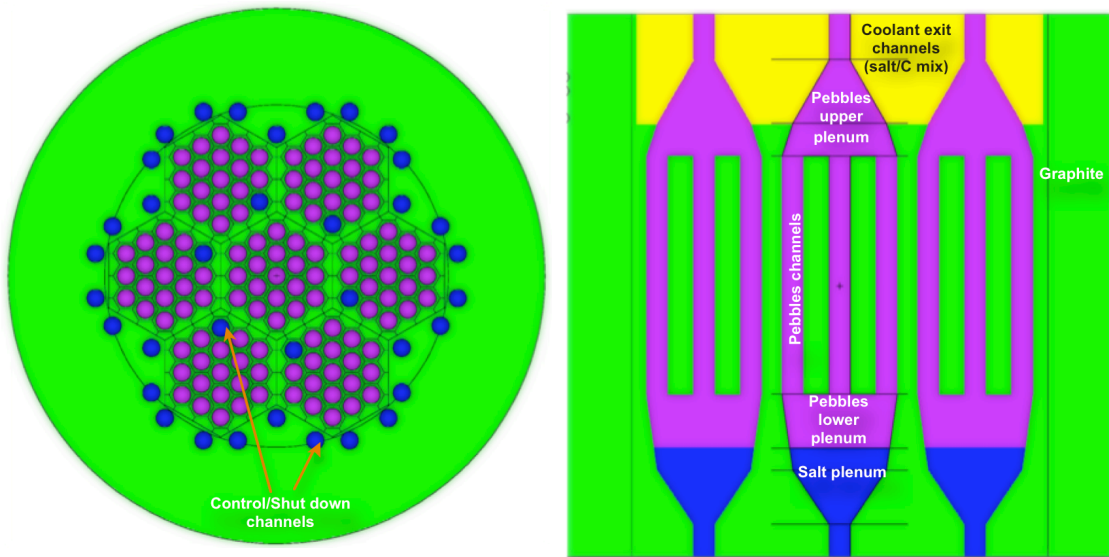


Figure 2.7 Horizontal and vertical views of the MPB-AHTR full core model—pebbles are not shown in this figure but are explicitly modeled in MCNP.

The defueling chutes extend ~ 4 m above the upper plenum. A preliminary simulation concluded that the power produced in the chutes is relatively small ($<0.4\%$) and it was neglected in the depletion model. The chutes model was further simplified using a homogeneous mix of graphite (55 vol%) and flibe (45 vol%) since no effect was noticed on core multiplication factor (Table 2.3). Their length was set at 40 cm

corresponding to the length of the coolant flow exit channels.

Table 2.2 Geometry parameters for the MPB-AHTR design.

Parameter	Value
Fuel kernel diameter (μm)	425
Carbon buffer thickness (μm)	100
Pyrolytic carbon inner layer thickness (μm)	35
SiC layer thickness (μm)	35
Pyrolytic carbon outer layer thickness (μm)	35
Graphite central core diameter (cm)	1.6
Pebble shell thickness (cm)	0.25
Pebble outer diameter (cm)	3.0
Bed packing factor	55%
Channels diameter (cm)	19.8
Channels pitch (cm)	25.0
Channels per PCA	19
PCAs pitch (cm)	125.0

Table 2.3 Core effective multiplication factor and fractional power produced in the chute as a function of defueling chute length and composition—clean fuel 10% enriched, 425 μm diameter kernel, 35% TRISO packing factor.

Composition	Length (cm)	k_{eff}	Power (%)
Pebbles and flibe heterogeneous	0	1.36859 ± 0.00028	-
	40	1.37180 ± 0.00028	0.11
	400	1.37250 ± 0.00018	0.39
Graphite and flibe homogeneous	40	1.37136 ± 0.00031	-

The following sections summarize data used in the MCNP models, in particular: materials and their properties (2.2.1); temperature and corresponding cross sections (2.2.2).

2.2.1 Materials

Table 2.4 summarizes all the materials used in the MCNP models together with density and temperature at operating conditions of hot full power.

Table 2.4 PB-AHTR core materials densities and operating temperatures.

Component	Materials	Density (kg/m ³)	Temperature (°C)
Kernel	UC _{0.5} O _{1.5}	10.50	800
Carbon buffer	Carbon	1.00	800
Inner pyrolytic carbon	Pyrolytic carbon	1.87	800
SiC	SiC	3.20	800
Outer pyrolytic carbon	Pyrolytic carbon	1.87	800
Matrix	Graphite	1.60	750
Shell	Graphite	1.74	700
Coolant	LiF-BeF ₂	1.936	600 (inlet)
		1.987	704 (outlet)
		1.960	655 (average)
Structure ^a	Graphite	1.74	650
Reflector	Graphite	1.74	600

^a MPB-AHTR only

The fuel adopted is uranium oxy-carbide (UO_{1.5}C_{0.5}) that is preferred over more traditional uranium dioxide in order to reduce TRISO particles failure probability (M. G. Izenson 1987). The fuel enrichment was assumed either 10% or 19.9%. TRISO particles coating materials and densities are the standard values commonly used in the literature.

Graphite can be fabricated at multiple densities, therefore either the matrix density

in regular pebbles or the central core density in annular pebbles is foreseen to be varied to control the average pebbles density. In the parametric analysis a constant density of 1.6 kg/m^3 was applied for the matrix in regular pebbles and of 1.0 kg/m^3 for the central graphite core in annular pebbles. As stated above, fuel kernel and number of TRISO particles per pebbles are design parameters and the results are searched as a function of C/HM, therefore the conclusions of this study still stand when the matrix density is changed. All the rest of the graphite in the core—pebbles shell, PCA structures for the MPB-AHTR, and reflectors—are nuclear grade graphite H-451 (1.74 kg/m^3).

2.2.1.1 Coolant properties and composition

The liquid salt LiF-BeF_2 (2:1 molar ratio) or flibe was chosen as the PB-AHTR coolant for its unique combination of high volumetric heat capacity and relatively low viscosity (Chapter 1). The flibe density is given by the following expression (de Zwaan 2005):

Equation 2.1 $\rho(\text{kg/m}^3) = 2.28 - 4.884 \cdot 10^{-4} T(K)$

The melting point is at 459°C , the boiling point at 1430°C .

Among flibe constituents, the isotope 6 of lithium is a strong neutron absorber and to reduce its reactivity penalty, we assumed that lithium would be enriched to

99.995% in ${}^7\text{Li}$. A further depletion of ${}^6\text{Li}$ is obtained in the core by means of (n,γ) reactions, but ${}^6\text{Li}$ is not completely eliminated because it is continuously produced by (n,α) reaction on ${}^9\text{Be}$ (de Zwaan 2005). The following balance equation describes ${}^6\text{Li}$ concentration in the core evolution as function of time:

$$\text{Equation 2.2} \quad \frac{dN_{Li-6}(t)}{dt} = \sigma_{Be-9}^{\alpha} N_{Be-9}(t)\phi - \sigma_{Li-6}^{abs} N_{Li-6}(t)\phi$$

where the σ_{Be-9}^{α} and σ_{Li-6}^{abs} are the one-group effective cross sections for (n,α) on ${}^9\text{Be}$ and for total absorption on ${}^6\text{Li}$, respectively, and ϕ the average flux level in the core. Since the (n,α) cross section for ${}^9\text{Be}$ in the PB-AHTR is ~ 2 mb, it can be assumed that the ${}^9\text{Be}$ concentration is about constant, then:

$$\text{Equation 2.3} \quad N_{Li-6}(t) = N_{Li-6}^0 e^{-\sigma_{Li-6}^{abs}\phi t} + \frac{\sigma_{Be-9}^{\alpha}}{\sigma_{Li-6}^{abs}} N_{Be-9} \left(1 - e^{-\sigma_{Li-6}^{abs}\phi t}\right)$$

that for $t \gg 0$ becomes:

$$\text{Equation 2.4} \quad N_{Li-6}(t) = \frac{\sigma_{Be-9}^{\alpha}}{\sigma_{Li-6}^{abs}} N_{Be-9}$$

This means ${}^6\text{Li}$ reaches an equilibrium concentration after an initial transient that is independent on the total neutron flux, but only depends on the neutron spectrum.

Since the absorption cross section of ${}^6\text{Li}$ is large (~ 200 b) the time required to reach this equilibrium is small enough to be insignificant in the lifetime of the PB-AHTR. The ${}^6\text{Li}$ equilibrium concentration was studied using MOCUP for depleting the salt¹ while the fuel composition was assumed to remain constant. Table 2.5 shows the results obtained. At equilibrium, ${}^6\text{Li}$ is reduced to about 1/10 of the initial amount, while the other constituents do not undergo any noticeable change in concentration. It requires about 2 effective full power years to reach equilibrium at the flux level corresponding to 10.2 MW/m^3 power density (Figure 2.8). The reduction of ${}^6\text{Li}$ concentration generates a reactivity gain of $\sim 5\%$ (Table 2.5) because of two effects: a reduction of neutrons absorption in the salt by $\sim 3\%$ (Table 2.6) and a larger number of thermal neutrons available for fissioning as showed by the change in the thermal spectrum (Figure 2.9) and by the increase of η (Table 2.6).

Table 2.5 Salt composition and infinite multiplication factor at different exposure times with constant fuel composition (clean fuel).

Parameter		0 EFPD	1000 EFPD
k_{∞}		1.3462	1.4165
Concentration (atoms/b-cm)	${}^6\text{Li}$	$1.1918 \cdot 10^{-6}$	$9.9260 \cdot 10^{-8}$
	${}^7\text{Li}$	$2.3836 \cdot 10^{-2}$	$2.3826 \cdot 10^{-2}$
	${}^9\text{Be}$	$1.1918 \cdot 10^{-2}$	$1.1918 \cdot 10^{-2}$
	${}^{19}\text{F}$	$4.7674 \cdot 10^{-2}$	$4.7674 \cdot 10^{-2}$

¹ MOCUP, as is, cannot be applied to salt depletion because ${}^6\text{Li}$ main reaction ${}^6\text{Li}_3({}^1_0\text{n}, {}^3_1\text{H})^4_2\text{He}$ in the ENDF library is denoted as MT 105 reaction that is (n,T), but this reaction is not among those tracked by MOCUP. Nevertheless, the (n,T) reaction in this case is equivalent to an (n, α) reaction and this is among those treated in MOCUP. A script was created to read the (n,T) cross section for ${}^6\text{Li}$ evaluated by MCNP and to input it in ORIGEN as the (n, α) cross section.

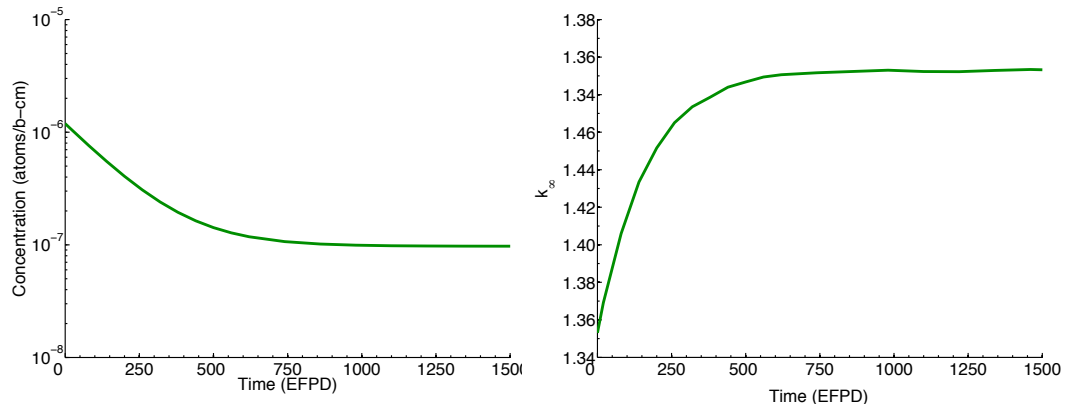


Figure 2.8 ${}^6\text{Li}$ concentration as function of time starting from initial (50 ppm ${}^6\text{Li}$) salt composition and corresponding single pebble infinite multiplication factor with clean fuel composition.

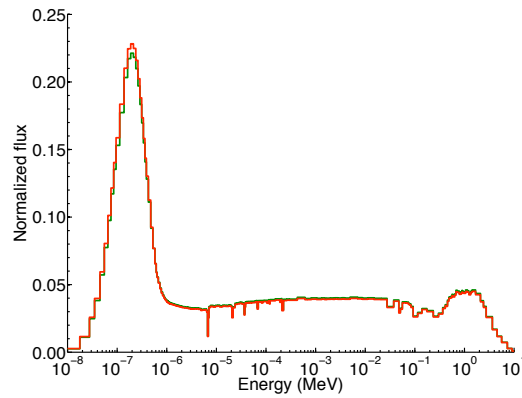


Figure 2.9 Comparison of the neutron spectrum in the fuel with initial and equilibrium salt composition.

Table 2.6 Pebble properties with initial and equilibrium salt composition.

Parameter	Flibe (0.005% ^6Li)	Flibe (0.0004% ^6Li)
$k_{\infty} (\sigma)$	1.34625 (0.00024)	1.41603 (0.00023)
η	1.55	1.57
f	0.86	0.90
CR	0.303	0.291
Fractional Absorption		
Fuel kernel	86.09%	89.59%
Coatings	0.57%	0.60%
Graphite matrix	0.85%	0.83%
Graphite structure	0.75%	0.79%
^6Li	4.32%	0.37%
^7Li	4.17%	4.39%
^9Be	0.77%	0.80%
^{19}F	2.47%	2.56%
Total coolant	11.74%	8.13%

2.2.2 Temperatures and cross sections

The MCNP models assume materials at their actual operating conditions, including temperature. Table 2.4 summarizes the temperatures assigned for each material and core component. Cross sections were chosen according to those temperatures for proper treating of Doppler effect. An average temperature was assumed for the TRISO particles. The cross sections used are from the ENDF/B-VI.7 library. Scattering kernels for the carbon thermal elastic scattering cross section were applied when carbon atoms are bond to form graphite, that is in the TRISO layers, in the matrix, in the pebbles shell, PCAs structure and reflectors. Each of these

components was assigned the scattering kernels corresponding to the operating temperature².

2.3 Modeling of fuel heterogeneities

The main challenge in modeling the PB-AHTR and in general any reactor that features TRISO fuel is to properly treat the double heterogeneity effect created by lumping the fuel into particles and those into pebbles. Most of the deterministic codes need to be modified (e.g. Dancoff factors correlations) to properly treat this effect. The SCALE package, for example, only in the latest version 5.1 introduced a subroutine for treating double heterogeneity. Nevertheless this can only be applied to criticality simulations and not to depletion analysis. MCNP instead is capable of treating double heterogeneity without requiring any modification, given its stochastic nature—no need for Dancoff factors—and a very flexible geometry capability. Yet, modeling each fuel kernel is computationally challenging. Next two sections investigate the double heterogeneity effect and present the approach applied to reduce computational time.

2.3.1 Double heterogeneity

The PB-AHTR integral design core contains ~1.25 million pebbles, each of which holds 20,000÷80,000 TRISOs for a total of more than 10^{10} particles in the entire core.

² For scattering kernels we used the SAB2002 library. Since this library provides data only for a limited set of temperatures (294 K, 400 K, 600 K, 800 K, 1,000 K and 1,200 K), scattering kernels at each needed temperature were generated interpolating the available data (Brown, 2006).

Modeling so many fuel regions in MCNP is feasible and relatively simple, but achieving accurate statistics is extremely time consuming even when taking advantage of parallel computing. In order to reduce computational time two approaches were tested using a single pebble model:

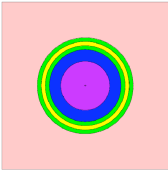
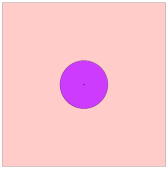
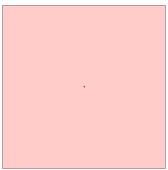
1. Uniform pebble in which TRISO particles and matrix are fully mixed conserving the total number of atoms of each constituent;
2. Homogenization of TRISO particle coatings with the carbon matrix while keeping each fuel kernel (Brown, et al. 2005).

Table 2.7 compares the infinite multiplication factor for these simplified models against a fully heterogeneous model. A fully homogenized pebble model is not accurate since k_{∞} is underestimated by $\sim 6\%$, meaning that the spatial self-shielding effect in the kernels is relevant. Indeed, if we decompose the multiplication factor in two factors: the fraction of neutrons absorbed in the fuel— f , and the neutrons generated per neutron absorbed in the fuel— η , it is found that while f increases moving from the heterogeneous (~ 0.86) to the homogeneous model (~ 0.88), η drops from ~ 1.55 to ~ 1.28 . A closer look at the components of η reveals that the homogeneous model overestimates ^{238}U effective capture cross section (5.68 b vs. 4.47 b in the heterogeneous model) since it does not catch the drop in the epithermal flux that occurs through the kernels due to spatial self-shielding.

The model with homogenized layers maintains k_{∞} similar to the fully heterogeneous model. This is not surprising since the TRISO coatings are mainly

made of carbon and they are mixed with the matrix that is also made of carbon; furthermore the fuel lumping effect is preserved since the geometry of the kernels is preserved. This simplification saves roughly 25% of computational time compared to the fully heterogeneous model.

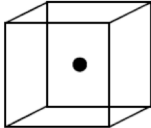
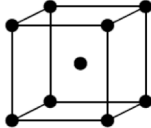
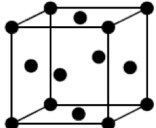
Table 2.7 Effect of TRISO particles homogenization—clean fuel 10% enriched, 425 μm diameter kernel, 10% TRISO packing factor, 50 ppm ^6Li .

Model		$k_{\infty} (\sigma)$	k_{∞} error (%)	Time saving
Heterogeneous		-	1.34652 (0.00026)	-
Fuel kernels with matrix and coatings homogenized		-0.02	1.34625 (0.00024)	25%
Fully homogenized		-5.59	1.27119 (0.00025)	80%

In the MCNP model fuel kernels are not randomly distributed inside the pebbles but are modeled as ordered structure having one of three possible patterns: simple cubic, body centered cubic, and face centered cubic. The results pertaining to these three patterns are compared in Table 2.8. It was found that the differences in reactivity are negligible. Version 5 of MCNP introduced the possibility of modeling a random

distribution, as well³. Since this distribution is stochastically determined, many realizations are required to obtain unbiased results therefore the computational time increases by hundredfold making this feature impractical to use for computationally intense studies. Table 2.8 shows that no difference in k_{∞} derives from using random distribution rather than ordered structures.

Table 2.8 Infinite multiplication factor as a function of fuel kernel lattice structure—clean fuel 10% enriched, 425 μm diameter kernel, 10% TRISO packing factor, 50 ppm ^6Li .

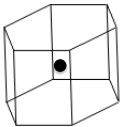
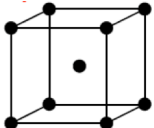
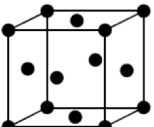
Structure		$k_{\infty} (\sigma)$
Simple Cubic		1.34625 (0.00024)
Body Centered Cubic		1.34632 (0.00023)
Face Centered Cubic		1.34637 (0.00030)
Random		1.34668 (0.00038)

A similar study was performed to select the arrangement of the array of pebbles. The simple cubic structure was not included because it can only provide packing factors up to $\sim 52.4\%$. The structures considered include a hexagonal prism cell

³ In reality the possible distributions are only partially random. A grid must be predefined and an object can be randomly placed in any of the grid mesh with the constraint that the object is fully contained in the mesh (Brown, 2005).

(side-to-side distance equals the prism height), a body-centered and a face-centered cubic. Table 2.9 shows that the infinite multiplication factor is not affected by the pebble lattice structure applied. The hexagonal prism structure was chosen for the rest of the study.

Table 2.9 Infinite multiplication factor as a function of pebble lattice structure—clean fuel 10% enriched, 425 μm diameter kernel, 10% TRISO packing factor, and 50 ppm ^6Li .⁴

Structure		$k_{\infty} (\sigma)$
Simple Hexagonal Prism		1.34625 (0.00024)
Body Centered Cubic		1.34623 (0.00024)
Face Centered Cubic		1.34653 (0.00025)

When using a regular repeated structure, the boundary surfaces cut the lattice creating unrealistic partial cells—partial pebbles and/or partial kernels. These effects were subject of sensitivity studies by Albornoz and Korochinsky and they concluded that even if these cut cells introduce an alteration to the theoretically predicted fuel loading ($< 1\%$, either positive or negative), it does not produce relevant effects on the system reactivity because it does not modify the moderator-to-fuel atom ratio

⁴ Considering the way random packing is implemented in MCNP and that pebbles are very tight, the random pebble packing is not relevant for the scope of this comparison.

(Albornoz and Korochinsky 2006). In this study the error in the estimation of the fuel loading due to cut cells was overcome by calculating exact volumes with MCNP.

High accuracy in MCNP is obtained despite the fact the system is composed of an enormous number of very small fuel particles. This is possible because all the quantities calculated by the code are averaged over all the particles in the model or in a macro region within it.

2.4 Depletion methodologies

The scope of the depletion analysis is to determine the fuel composition as a function of fuel residence time in the core. This task is particularly complex in a pebble bed reactor because the fuel elements are small, numerous, and continuously recirculated through the system. After an initial transient period, the core average composition reaches an equilibrium state that characterizes the core neutronic properties. This equilibrium composition cannot be determined without knowing the burnup history—at least on average—of the pebbles because the fuel elements are discharged selectively. The following subsections illustrate simplified methodologies that were developed with the purpose of determining pebble burnup histories while preserving the physics of the system.

2.4.1 Infinite uniform bed method

This methodology uses an infinite bed model in which all pebbles are assigned same composition. Two main assumptions are made: (1) since pebbles are circulated many times—axial mixing, and every time are reinserted in a random location—radial mixing, it was assumed that at equilibrium, the pebbles are well-mixed so that there is an equal probability to find in any region of the core a pebble at any burnup level at any given time; (2) the average flux each pebble is exposed to remains constant during the entire residence time of the pebble in the core and it is determined by the average equilibrium composition of all pebbles in the core. This model is simulated in MCNP and the fuel composition as a function of time is determined using MOCUP (Moore, et al. 1995). Depletion is performed under the constraint of a constant flux so that the implementation in MOCUP of this assumption required modifying the sequence. The flux value is an iteration variable and at first it is assigned a guessed value. When depletion is completed, MOCUP provides the multiplication factor $k_{\infty,pebble}(BU)$ and the power generated per pebble $P_{pebble}(BU)$ as a function of burnup. Then the reactivity of the core is calculated from the reactivity of every pebble considering that each pebble contributes to the core total reactivity according to its power level. Since it is assumed that the neutron flux is uniform throughout the core is uniform, then the power generated by each pebble depends only on its burnup level, and the core k_{∞} can be determined from the following:

Equation 2.5
$$\frac{P_{core}}{k_{\infty,core}} = \sum_{i=1}^N \frac{P_{pebble}(BU_i)}{k_{\infty,pebble}(BU_i)}$$

where N is the total number of pebbles in the core. Discretizing the burnup into a finite number of m levels, becomes:

Equation 2.6
$$\frac{P_{core}}{k_{\infty,core}} = \sum_{j=1}^m n_j \frac{P_{pebble}(BU_j)}{k_{\infty,pebble}(BU_j)}$$

where n_j is the number of pebbles within the burnup range $BU_j \leq BU < BU_{j+1}$ and

$N = \sum_{j=1}^m n_j$. Since the pebbles are assumed to be well-mixed in the core, each burnup

level BU_j corresponds to the residence time t_j such that:

Equation 2.7
$$BU_j = \frac{1}{t_j m_{HM}} \int_0^{t_j} P_{pebble}(t) dt$$

Equation 2.6 can be rewritten as a function of the residence time of the pebble in the core:

Equation 2.8
$$\frac{P_{core}}{k_{\infty,core}} = \sum_{j=1}^m n_j \frac{P_{pebble}(t_j)}{k_{\infty,pebble}(t_j)}$$

Since the core is well-mixed, if T is the total residence time, then:

$$\text{Equation 2.9} \quad n_j = N \frac{t_{j+1} - t_j}{T} = N \frac{\Delta t_j}{T}$$

where $t_{m+1} = T$. Substituting in Equation 2.8:

$$\text{Equation 2.10} \quad \frac{P_{core}}{k_{\infty,core}} = \frac{N}{T} \sum_{j=1}^m \Delta t_j \frac{P_{pebble}(t_j)}{k_{\infty,pebble}(t_j)}$$

and re-arranging:

$$\text{Equation 2.11} \quad \frac{T\bar{P}_{pebble}}{k_{\infty,core}} = \sum_{j=1}^m \frac{\Delta t_j P_{pebble}(t_j)}{k_{\infty,pebble}(t_j)}$$

where $\bar{P}_{pebble} = P_{core}/N$ is the average power generated per pebble in the core. With one more modification:

$$\text{Equation 2.12} \quad \frac{\bar{E}_{pebble}}{k_{\infty,core}} = \sum_{j=1}^m \frac{E_{pebble}(t_j)}{k_{\infty,pebble}(t_j)}$$

where $\bar{E}_{pebble} = T\bar{P}_{pebble} = \sum_{j=1}^m \Delta t_j P_{pebble}(t_j)$ is the total average energy that a pebble

generates during the entire residence time and $E_{pebble}(t_j)$ is the energy generated in the

pebble during the time interval Δt_j . Finally, defining f_j as the fraction of energy generated by a pebble, on average, when the residence time is between t_j and t_{j+1} , that is:

$$\text{Equation 2.13} \quad f_j = \frac{E_{pebble}(t_j)}{\bar{E}_{pebble}} = \frac{\Delta t_j P_{pebble}(t_j)}{T \bar{P}_{pebble}} = \frac{\Delta t_j P_{pebble}(t_j)}{\sum_{j=1}^m \Delta t_j P_{pebble}(t_j)}$$

Equation 2.12 becomes:

$$\text{Equation 2.14} \quad \frac{1}{k_{\infty,core}} = \sum_{j=1}^m \frac{f_j}{k_{\infty,pebble}(t_j)}$$

The core total power, the number of pebbles and the multiplication factor are not variables but pre-established properties of the core. The total residence time T is determined assuming that the core average multiplication factor obtained from Equation 2.10 is equal to $k_{limit} = 1/P_{NL}$ where P_{NL} is the neutron non-leakage probability from the finite core. The k_{limit} increases if the excess reactivity required to compensate xenon transient after a power drop needs to be considered. Once T is obtained, the average power generated per pebble is determined as:

$$\text{Equation 2.15} \quad \bar{P}_{pebble} = \frac{1}{T} \int_0^T P_{pebble}(t) dt$$

where $P_{pebble}(t)$ has been obtained from MOCUP. The value calculated from Equation 2.14 must match the initially assumed value of $\bar{P}_{pebble} = P_{core} / N$. If this is not the case, a new value must be guessed for the neutron flux amplitude realizing that $\bar{P}_{pebble} \propto \phi$ since it can be approximated as

$$\text{Equation 2.16 } \bar{P}_{pebble} = \frac{E_f \phi V^{pebble}}{T} \int_0^T \Sigma_{fission}^{pebble}(t) dt$$

where E_f is the energy released per fission (assumed constant), V^{fuel} the fuel volume and $\Sigma_{fission}^{fuel}(t)$ the macroscopic fission cross section as a function of the residence time. The process is iterated until the power matches the target value.

Equation 2.5 is only valid under the assumption that the flux is uniform through the core. More realistically, a spatially varying flux distribution should be considered. In this case the power generated by a pebble is not only a function of its composition (burnup level) but also of its position in the core, then:

$$\text{Equation 2.17 } \frac{P_{core}}{k_{\infty,core}} = \sum_{i=1}^N \frac{P_{pebble}(BU_i, \vec{r}_i)}{k_{\infty,pebble}(BU_i)}$$

where \vec{r}_i refers to the position of the pebble in the core. If ϕ is the average flux in the core, then:

$$\begin{aligned}
 P_{pebble}(BU_i, \vec{r}_i) &= E_f V^{pebble} \Sigma_{fission}^{pebble}(BU_i) \phi(\vec{r}_i) = \\
 \text{Equation 2.18} \quad &= V^{pebble} \Sigma_{fission}^{pebble}(BU_i) \phi \cdot \frac{\phi(\vec{r}_i)}{\phi} = P_{pebble}(BU_i) f_i^{flux}
 \end{aligned}$$

where f_i^{flux} is the ratio between the neutron flux in pebble i to the average flux in the core. Then, Equation 2.17 becomes:

$$\text{Equation 2.19} \quad \frac{P_{core}}{k_{\infty,core}} = \sum_{i=1}^N \frac{f_i^{flux} P_{pebble}(BU_i)}{k_{\infty,pebble}(BU_i)}$$

Now, let us divide the core into a number of S zones such that in each zone z the flux intensity can be considered constant, then:

$$\text{Equation 2.20} \quad \frac{P_{core}}{k_{\infty,core}} = \sum_{z=1}^S f_z^{flux} \sum_{q=1}^{N_z} \frac{P_{pebble}(BU_q)}{k_{\infty,pebble}(BU_q)}$$

where N_z is the number of pebbles in zone z . Under the assumption that the core is well-mixed and that each zone contains a large enough number of pebbles, the probability of finding a pebble at any burnup level in any point of each zone z can be assumed to be the same. This means that the ratio:

Equation 2.21
$$\frac{P_z}{\sum_{q=1}^{N_z} \frac{P_{pebble}(BU_q)}{k_{\infty,pebble}(BU_q)}} = k_{\infty,z}$$

is independent of the zone of the core and then of the flux level, but it only depends on the burnup distribution:

Equation 2.22
$$k_{\infty,core} = k_{\infty,z} \quad \forall z = 1, \dots, S$$

This means that Equation 2.14 maintains its validity even when the flux distribution is not uniform, as long as the bed is well-mixed. However, this approximation is not valid in cases where the neutron spectrum is zone-dependent. This is expected to be the case in the proximity of a reflector. In principle, this approximation will be also invalid if the residence time of the pebble in a given zone, i.e. in a given flux level, is long as compared with the radioactive decay time of fuel isotopes of non-negligible contribution to the neutron fission and capture probability. Furthermore, this methodology does not account for the spatial distribution of the neutron importance.

Figure 2.10 shows the flow chart of this methodology as implemented in MOCUP. A flux amplitude is guessed and the depletion analysis of the uniform bed is performed assuming constant flux. Infinite multiplication factor and fuel composition as a function of residence time are determined. Using Equation 2.20 the residence time

can be determined constraining k_{core} to be equal to $1/P_{NL}$. The average power produced by a pebble during the entire residence time must match the core average power per pebble. If not, a new flux amplitude is applied.

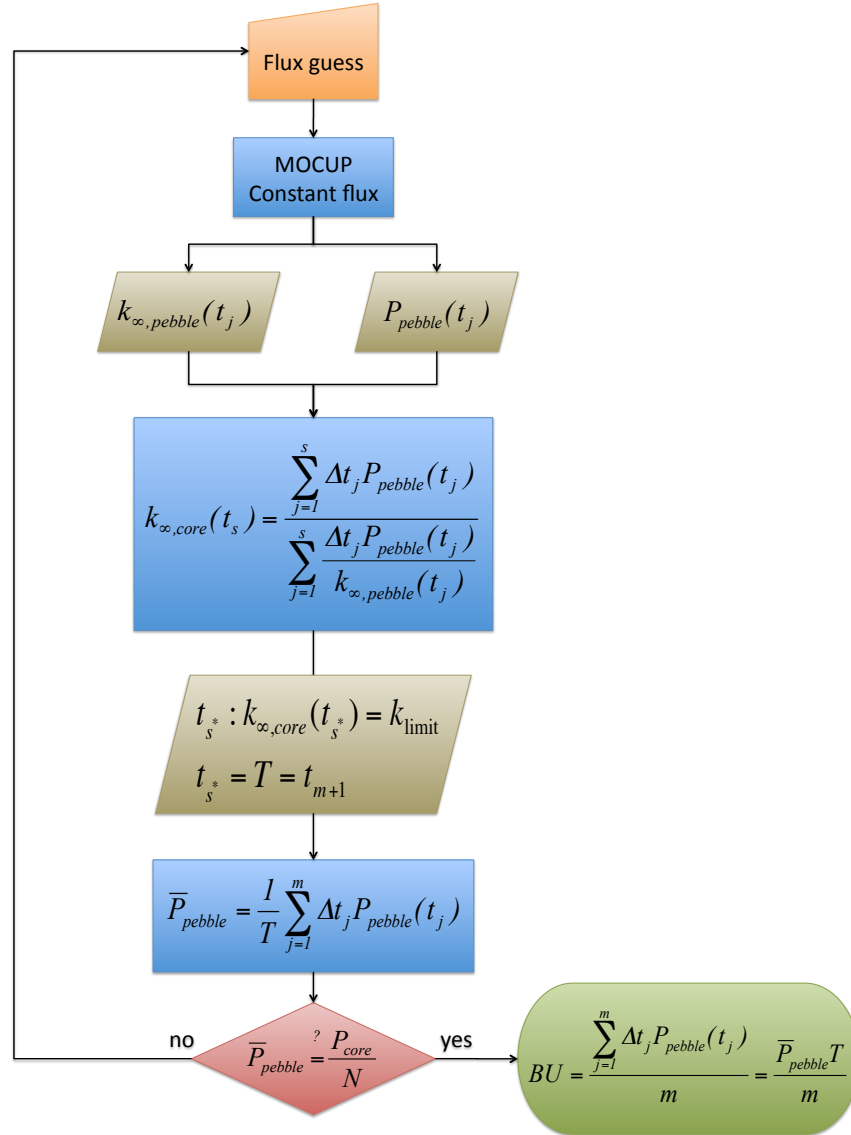


Figure 2.10 Uniform bed methodology flow chart.

The sensitivity of this methodology was evaluated estimating the change in the

predicted attainable burnup that follows a change in the pebble average power after a perturbation of the flux amplitude. Table 2.10 shows that the attainable burnup is not sensitive to the flux amplitude because the residence time balances each flux perturbations. The error on the prediction of average power per pebble (constrain value 1.9237 kW) that controls convergence is equivalent to the error on the flux amplitude. To reduce the uncertainty on the residence time below 1 Effective Full Power Days (EFPD), the acceptable error on the average power per pebble was set $< 0.1\%$.

Table 2.10 Sensitivity to the flux amplitude of the average pebble power and of the attainable burnup predicted by the uniform bed methodology—425 μm fuel kernel, 10% packing factor.

Flux (neutrons/cm ² -s)	Pebble power (kW)	Power error (%)	Burnup (GWd/tHM)	Residence time (EFPD)
$3.88 \cdot 10^{14}$	1.8789	-2.33	125.02	535
$3.96 \cdot 10^{14}$	1.9198	-0.21	125.11	524
$3.98 \cdot 10^{14}$	1.9272	+0.18	125.12	522
$4.00 \cdot 10^{14}$	1.9334	+0.50	125.28	521
$4.08 \cdot 10^{14}$	1.9766	+2.75	124.89	508

2.4.2 Single pebble in equilibrium bed method

The infinite uniform bed methodology is relatively fast and effective for scoping analysis, but it carries embedded approximations that limit its applicability. In particular that methodology is based on one pebble neglecting the effect of the neighboring pebbles that have a different composition. This effect is negligible, as it

will be shown later in this section, for 10% enriched uranium fuel pebbles because the neutron spectrum through the pebble does not change drastically during the depletion (Figure 2.11), but it can be important, for example when pebbles are loaded with TRU, because the spectrum changes dramatically from BOL to EOL. For this reason, an improved methodology was developed and it is referred to as “single pebble in equilibrium bed.” This is based on a subset of all pebbles in the core, whose average composition is representative of the core average composition, and in the case of a well-mixed core it is independent from where in the core this subset is extracted.

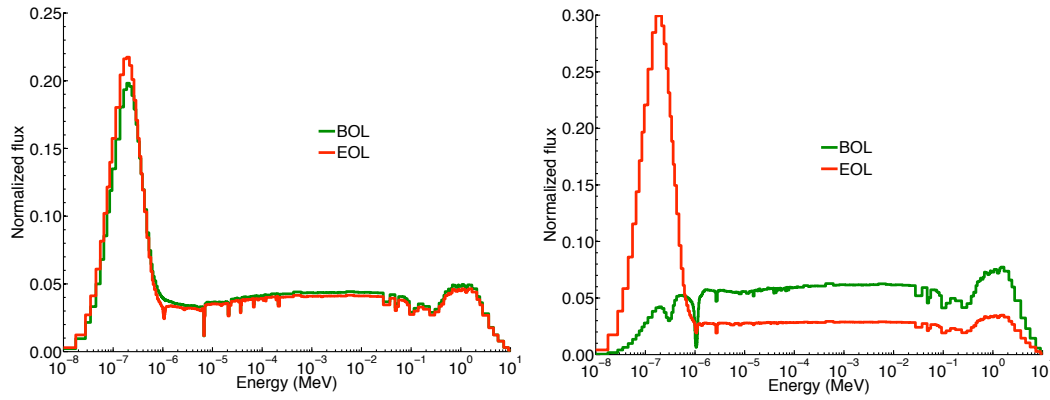


Figure 2.11 Neutron spectrum comparison at BOL and EOL as obtained from the infinite uniform bed methodology for 10% enriched uranium (left) and TRU (right) fuels.

All pebbles in the subset are assigned the same fuel composition, supposedly the core equilibrium composition, but one fresh pebble is placed in the middle of the subset. This pebble initially contains fresh fuel, and then is depleted while all the other pebbles maintain their set composition. This way, the condition that the neutron spectrum depends mainly on the neighboring pebbles is realized.

This methodology was implemented using MOCUP, after ad hoc modifications, as illustrated in Figure 2.12. Initially, the bed is assigned an arbitrary composition; the sample pebble is depleted assuming that the flux amplitude remains constant during the entire residence time while the power produced in it changes and is determined at each depletion step. The power produced in each of the fixed pebbles in the bed equals the average power per pebble in the core—the core total power divided by total the number of pebbles in the core—1.92 kW. Then:

$$\text{Equation 2.23} \quad P_{pebble}(t) = \frac{R_{pebble}^{fis}}{R_{bed}^{fis}} \bar{P}_{pebble}$$

where R^{fis} is the fission reaction rate per pebble either in the sample pebble or in the bed. The fission reaction rates are obtained from extra tallies added in MCNP. Once the depletion is completed the residence time is calculated by imposing the requirement that the average power produced in the pebble during its life matches the average power per pebble:

$$\text{Equation 2.24} \quad T = \frac{\sum_{j=1}^m \Delta t_j P_{pebble}(t_j)}{\bar{P}_{pebble}}$$

where m is the number of time steps applied to the depletion analysis and Δt_j their

length. Equation 2.24 holds under the assumption of a well-mixed core. When the residence time is known, the bed composition can be determined from the following:

$$\text{Equation 2.25} \quad \underline{N}^{bed} = \frac{1}{T} \sum_{j=1}^m \Delta t_j \underline{N}^{pebble}(t_j)$$

At this point the process goes back to a new depletion calculation and it is iterated until the bed composition remains constant in few successive iterations. The infinite multiplication factor of this subset of pebbles must be the same, in the well-mixed conditions, as the core k_∞ —since the sample pebble does not practically affects it. If $k_\infty = 1/P_{NL}$, where P_{NL} is the probability of non-leakage established a priori with a full core simulation, then the target is achieved. Otherwise the flux assumption is modified accordingly and a new equilibrium composition is searched.

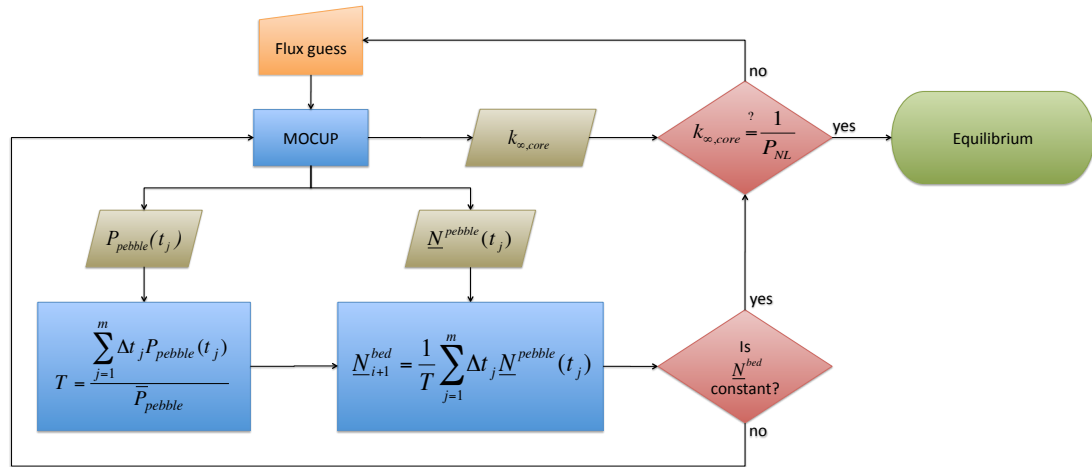


Figure 2.12 Single pebble in equilibrium bed methodology flow chart.

The sensitivity of this methodology was evaluated by estimating the change in the predicted attainable burnup that follows a change in the equilibrium bed k_∞ after a perturbation of the flux amplitude. Table 2.11 shows that in this methodology the attainable burnup is very sensitive to the spectrum level. The convergence is controlled by the error on the estimated k_∞ that was constrained to be $<0.1\%$ in order to determine the attainable burnup within a confidence of ± 1 GWd/tHM.

Table 2.11 Sensitivity to the flux amplitude the equilibrium infinite multiplication factor and of the attainable burnup predicted by the single pebble in equilibrium bed methodology—425 μm fuel kernel, 12.5% TRISO packing factor.

Flux (neutrons/cm ² -s)	k_∞	k_∞ error (%)	Burnup (GWd/tHM)	Residence time (EFPD)
$3.23 \cdot 10^{14}$	1.0531	+2.18	113.2	584
$3.31 \cdot 10^{14}$	1.0358	+0.50	122.7	641
$3.33 \cdot 10^{14}$	1.0306	0.06	125.4	655
$3.35 \cdot 10^{14}$	1.0251	-0.48	128.9	672
$3.43 \cdot 10^{14}$	1.0110	-1.90	139.7	722

The assumption of constant flux amplitude is not necessary to this methodology. The flux, indeed, could be determined at each time step using MCNP tallies. In this case the iteration variable would be the bed composition and controlling the convergence would become very difficult if not impossible. Figure 2.13 shows the flux as a function of burnup when constraints on it are released. The variation with respect to an average value is below 3%, therefore, the constant flux assumption was considered reasonable.

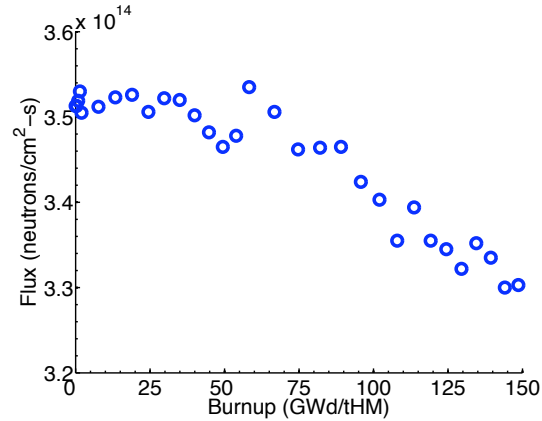


Figure 2.13 Neutron flux amplitude in the sample pebble as a function of burnup when not constrained to be constant—425 μm fuel kernel diameter, 12.5% TRISOs packing factor, 10% enriched uranium.

The size of the pebbles subset was chosen to comply with the assumption that the flux through a pebble and the subset k_{∞} are independent from the specific pebble composition, and dictated by the core average composition. Different sizes were compared: 10^2 , 10^3 and 10^4 . It was found that a subset of 10^3 pebbles is sufficient to realize the required conditions (Table 2.12).

Table 2.12 Infinite multiplication factor as a function the equilibrium bed size—425 μm fuel kernel diameter, 12.5% TRISOs packing factor, 10% enriched uranium.

Bed size	$k_{\infty} (\sigma)$
10^0 (uniform bed)	1.39467 (0.00022)
10^1	1.05212 (0.00025)
10^2	1.04524 (0.00015)
10^3	1.03936 (0.00016)
10^4	1.03922 (0.00008)

Figure 2.14 shows that the equilibrium bed imposes a more thermal flux to a fresh

pebble and the difference between the neutrons spectrum that this fresh pebble sees when in a uniform bed and the one when in an equilibrium bed (1:1,000) is negative in the thermal region and positive in the epithermal and fast region.

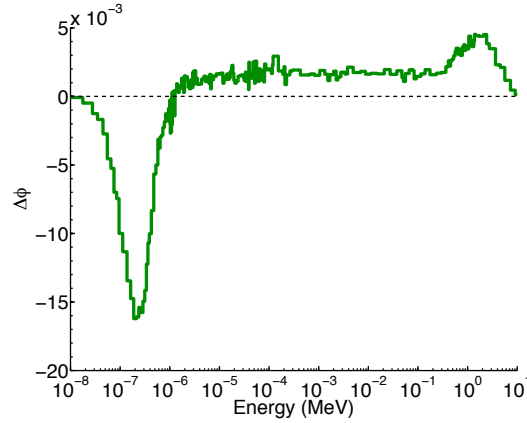


Figure 2.14 Normalized neutron spectrum difference between a fresh pebble when in a uniform bed and when in an equilibrium bed—425 μm fuel kernel diameter, 12.5% TRISOs packing factor, 10% enriched uranium.

2.4.2.1 Single pebble in equilibrium bed vs. uniform bed

To estimate the limitation of the uniform bed methodology, we compared it with the equilibrium bed methodology. Two sample cases were considered: (1) 10% enriched uranium fuel kernel, 425 μm diameter, 12.5% packing factor; (2) TRU fuel kernel, 200 μm diameter, 11% packing factor. As anticipated, the two methodologies show reasonable agreement for enriched uranium fuel (Table 2.13) since the neutron spectrum does not change drastically from BOL to EOL (Figure 2.11). The uniform bed methodology instead generates an over-estimation of the burnup for TRU fuel

(Table 2.14) because it predicts a very soft spectrum towards EOL (Figure 2.11) that in reality the pebble mixing prevents (Figure 2.15).

Table 2.13 Uniform bed and single pebble in uniform bed methodologies prediction comparison for enriched uranium—425 μm kernel diameter, 12.5% TRISOs packing factor.

Features	Uniform pebble	Single pebble
Burnup (GWd/tHM)	127.0	125.4
Residence time (EFPD)	664	655
Flux (neutrons/cm ² -s)	$3.34 \cdot 10^{14}$	$3.33 \cdot 10^{14}$

Table 2.14 Uniform bed and single pebble in uniform bed methodologies prediction comparison for TRU—200 μm kernel diameter, 11% TRISOs packing factor.

Features	Uniform pebble	Single pebble
Burnup (GWd/tHM)	685	644
Residence time (EFPD)	663	625
Flux (neutrons/cm ² -s)	$3.28 \cdot 10^{14}$	$3.20 \cdot 10^{14}$

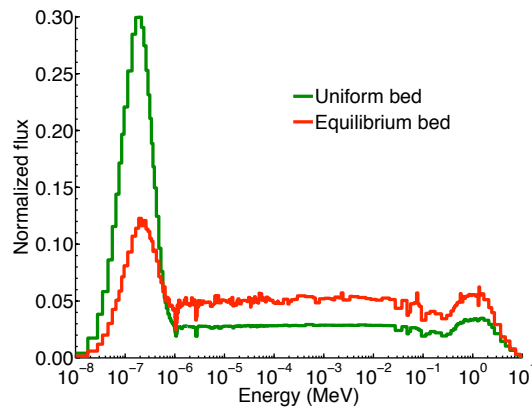


Table 2.15 Neutrons spectrum in the fuel of a pebble near EOL (640 GWd/tHM) when calculated using the uniform bed and the equilibrium bed methodologies; 200 μm kernel diameter, 11% TRISOs packing factor.

2.4.3 Full core method

The methodologies presented so far are all based on the assumption that pebbles are well-mixed and they all see the same neutron flux. In reality, pebbles can face multiple conditions and more phenomena need to be considered: the wall effect of the boundary surfaces on the local C/HM; the axial burnup distribution; the radial burnup distribution when pebbles are not randomly placed in the core like in the MPB-AHTR. To better capture these effects, a full core methodology was developed. This methodology is not meant to replace the simplified methodologies, but to provide a tool for refining the parametric analysis for which the faster methods described above are more suitable. The full core approach is based on the observation that the neutron spectrum in a pebble is determined by the other pebbles that occupy the same core region rather than by the pebble composition itself (Massimo 1976). Then, if the individual pebble composition does not perturb significantly the local average neutron spectrum, the effective one-group (1-g) microscopic cross sections depend only on the pebble position in the core and not on its own composition. Following this consideration, we developed a methodology to obtain a pebble fuel composition as a function of the residence time in the core and to use it to determine the core equilibrium composition. For this purpose, let us describe the trajectory of a pebble in the core by the vector $\tilde{r}(t)$ that represents the pebble position at any time t . The fuel composition vector $\underline{N}_{pebble}(t)$ of a pebble changes, in general, as follows:

Equation 2.26
$$\frac{d\underline{N}_{pebble}(t)}{dt} = -A[\underline{\tilde{r}}(t), \underline{N}_{pebble}(t)]\underline{N}_{pebble}(t)$$

where $A[\underline{\tilde{r}}(t), \underline{N}_{pebble}(t)]$ is the depletion matrix that contains physical parameters that affect the depletion process—decay constants, 1-g effective cross sections, and flux. Under the assumption that the neutron spectrum and, therefore, the effective cross sections do not depend on the pebble composition but rather on its position in the core, the depletion matrix is independent of the fuel vector, i.e. $A[\underline{\tilde{r}}(t), \underline{N}_{pebble}(t)] \equiv A[\underline{\tilde{r}}(t)]$ and Equation 2.26 can be rewritten as:

Equation 2.27
$$\underline{N}_{pebble}(t) = \underline{N}_{pebble}(t_0) \cdot e^{-\int_{t_0}^t A[\underline{\tilde{r}}(t')] dt'}$$

To better link the pebble motion in the core and its depletion history, let us split the trajectory into two components: the radial component $\underline{\tilde{v}}(t)$ that defines the position in the xy plane at time t and the vertical component $\tilde{z}(t)\hat{k}$. Then:

Equation 2.28
$$\underline{\tilde{r}}(t) = \underline{\tilde{v}}(t) + \tilde{z}(t)\hat{k}$$

The pebble motion defines the properties of these two functions, in particular the vertical trajectory is a piecewise monotonously increasing function in the range $[0, H]$ where H is the active length of the core. This is because the pebbles can only move from bottom to top and cannot move backward, except when they move outside of the

core from the exit plane at level H from where they are transferred to the entrance plane at level 0.

Let us consider a zone X subspace of the core space V ; if cross sections can be considered radially independent within X then the depletion matrix depends only on the vertical component of the trajectory, i.e. $A[\tilde{r}(t)] = A[\tilde{z}(t)]$, and Equation 2.27 becomes:

$$\text{Equation 2.29} \quad \underline{N}_{pebble}(t) = \underline{N}_{pebble}(t_0) \cdot e^{-\int_{t_0}^t dt' A[\tilde{z}(t')]} \quad \forall \tilde{r} \in X \subseteq V$$

Assuming that all pebbles move at the same velocity, the depletion history is the same for any pebble crossing this zone.

If instead cross sections in X also depend on the radial position then a pebble can have different depletion histories. However, observing that pebbles move in slug flow and the mixing is limited, it is reasonable to assume that once a pebble enters the zone X in the radial position \tilde{v} this position does not change until it transits to a new zone. Then the trajectory can be described as $\tilde{r}(t) = \tilde{v} + \tilde{z}(t)\hat{k}$ and the depletion matrix as $A[\tilde{r}(t)] = A[\tilde{v}, \tilde{z}(t)]$, for which Equation 2.27 becomes:

$$\text{Equation 2.30} \quad \underline{N}_{pebble}(\tilde{v}, t) = \underline{N}_{pebble}(\tilde{v}^*, t^*) \cdot e^{-\int_{t^*}^t dt' A[\tilde{v}, \tilde{z}(t')]} \quad \forall \tilde{r}(t) \in X \subseteq V, t \in [t^*, t^* + \Delta t)$$

where t^* is the time when the pebble enters zone X and $\tilde{\underline{r}}^* = \tilde{\underline{v}}^* + \tilde{\underline{z}}^* \hat{k}$ is the entry position; $t^* + \Delta t$ is the exit time and $\tilde{\underline{r}}^* + \Delta \tilde{\underline{r}} = \tilde{\underline{v}}^* + (\tilde{\underline{z}}^* + \Delta \tilde{\underline{z}}) \hat{k}$ the exit position.

$\underline{N}_{pebble}(\tilde{\underline{v}}^*, t^*)$ is defined by the boundary condition on the entry plane of zone X .

Equation 2.29 does not apply at $\tilde{\underline{r}}^* + \Delta \tilde{\underline{r}}$ where pebbles exit zone X to enter zone Y . Depletion histories through X , as well as characteristics of the Y zone, determine the fuel vector at this discontinuity region. Different scenarios can be imagined. Here we limit our consideration to the case where pebbles coming from different parallel zones converge into a radially uniform zone, like it would be the case when pebbles are collected at the entrance of the defueling chutes in the integral design or when pebbles exit the channels region in the modular design. In this case the fuel vector changes as in Equation 2.29 while the boundary condition at the entry plane $\tilde{\underline{r}}^* + \Delta \tilde{\underline{r}} = \tilde{\underline{v}}^* + (\tilde{\underline{z}}^* + \Delta \tilde{\underline{z}}) \hat{k}$ is:

$$\text{Equation 2.31} \quad \underline{N}_{pebble}(t^* + \Delta t) = \frac{\int d\tilde{\underline{v}} \left[\lim_{t \rightarrow t^* + \Delta t} \underline{N}_{pebble}(\tilde{\underline{v}}, t) \right]}{\int_{\partial X / \partial Y} d\tilde{\underline{v}}}$$

where $\partial X / \partial Y$ is the boundary surface between zone X and zone Y .

In conclusion if the trajectory of the pebble and the depletion matrix for any point in core are known, the pebble fuel composition can be calculated as a function of the residence time. The core composition can then be obtained considering that at any

point of the core the fuel vector will be equal to the average of the fuel vectors carried by all pebbles that cross that point some time during their history. In formula:

$$\text{Equation 2.32} \quad \underline{N}_{core}(\underline{r}) = \frac{\int_0^T dt \underline{N}_{pebble}(t) \delta[\underline{r} - \tilde{r}(t)]}{\int_0^T dt \delta[\underline{r} - \tilde{r}(t)]}$$

where T is the pebble total residence time. Simplified:

$$\text{Equation 2.33} \quad \underline{N}_{core}(\underline{r}) = \frac{\sum_{i=1}^{n(\underline{r})} \underline{N}_{pebble}(t_i)}{n(\underline{r})}$$

where $n(\underline{r})$ is the number of times a pebble is found in position \underline{r} and t_i the corresponding time in the pebble life.

This methodology can be further simplified if it can be assumed that within each zone cross sections are uniform in the axial direction. Then Equation 2.29 for a radially uniform zone becomes:

$$\text{Equation 2.34} \quad \underline{N}_{pebble}(t_{i+1}) = \underline{N}_{pebble}(t_i) \cdot e^{-A_i(t_{i+1}-t_i)}$$

where t_i and t_{i+1} are the time pebbles enter and exit zone i , respectively, and A_i is the depletion matrix for the same zone. For a radially non-uniform zone, instead, Equation

2.31 becomes:

$$\text{Equation 2.35 } \underline{N}_{pebble}(t_{i+1}) = \frac{\sum_{j=1}^{p_i} \underline{N}_{pebble,j}(t_i) \cdot e^{-A_{i,j}(t_{i+1}-t_i)}}{p_i}$$

We developed a depletion analysis algorithm to implement the methodology, derived above, using MCNP and ORIGEN2 along with the MOCUP code utilities. This algorithm determines a pebble burnup history from which it derives the core equilibrium composition. This new algorithm is illustrated for the Modular PB-AHTR the MCNP model for which is shown in Figure 2.7.

Figure 2.15 gives the methodology flow chart. At first the fuel is assigned an arbitrary composition and the residence time is assigned a guessed value. The pebble trajectory in the core is assumed to be known. The depletion scheme proceeds as follows:

1. The core is divided into zones grouping together regions where the spectrum can be considered similar.
2. For each zone MCNP determines relevant reactions rates for those nuclides, whose concentration in the fuel needs to be tracked. The MCNP input structure is similar to that used for MOCUP but extra tallies are added to obtain total fission rates in each zone. MCNP provides core k_{eff} , as well.
3. The mcnpPRO module of MOCUP reads zone-by-zone flux and nuclides'

reactions rates, and calculates zone-wise effective 1-g cross sections. The utility fluxPRO reads zone total fission rates from which the zone-wise power level is determined so as to conserve the total core power. Once the power of each zone is known, fluxPRO determines the corresponding zone flux amplitude using the origenPRO module of MOCUP.

4. The depletionPRO module performs the actual fuel depletion, starting from fresh fuel and following the trajectory of the pebble in the core. At each depletion step initial composition, flux, cross sections and step length are provided to ORIGEN2 according to the corresponding position of the pebble in the core. As the flux is assumed constant within a zone, consequently the power generated per pebble is dictated by its composition. ORIGEN2 outputs the fuel composition at the end of each time step thus providing $\underline{N}_{pebble}(t)$ at discrete points in time. For depletion of zones with distinct possible paths, an extra module, called parallelPRO, is launched. This creates a branch depletion calculation for each possible path starting from the entry plane, and collapses them into a single average composition at the exit plane (Equation 2.35).
5. The time dependent pebble composition obtained from deplePRO is used as input to the utility corePRO. This reconstructs the core composition using Equation 2.33.
6. The new zone-by-zone core composition is input to the MOCUP utility compPRO that creates a new input for MCNP.

The loop is repeated until k_{eff} gets constant and the entire process is re-iterated varying the residence time guessed value, to find the critical equilibrium core.

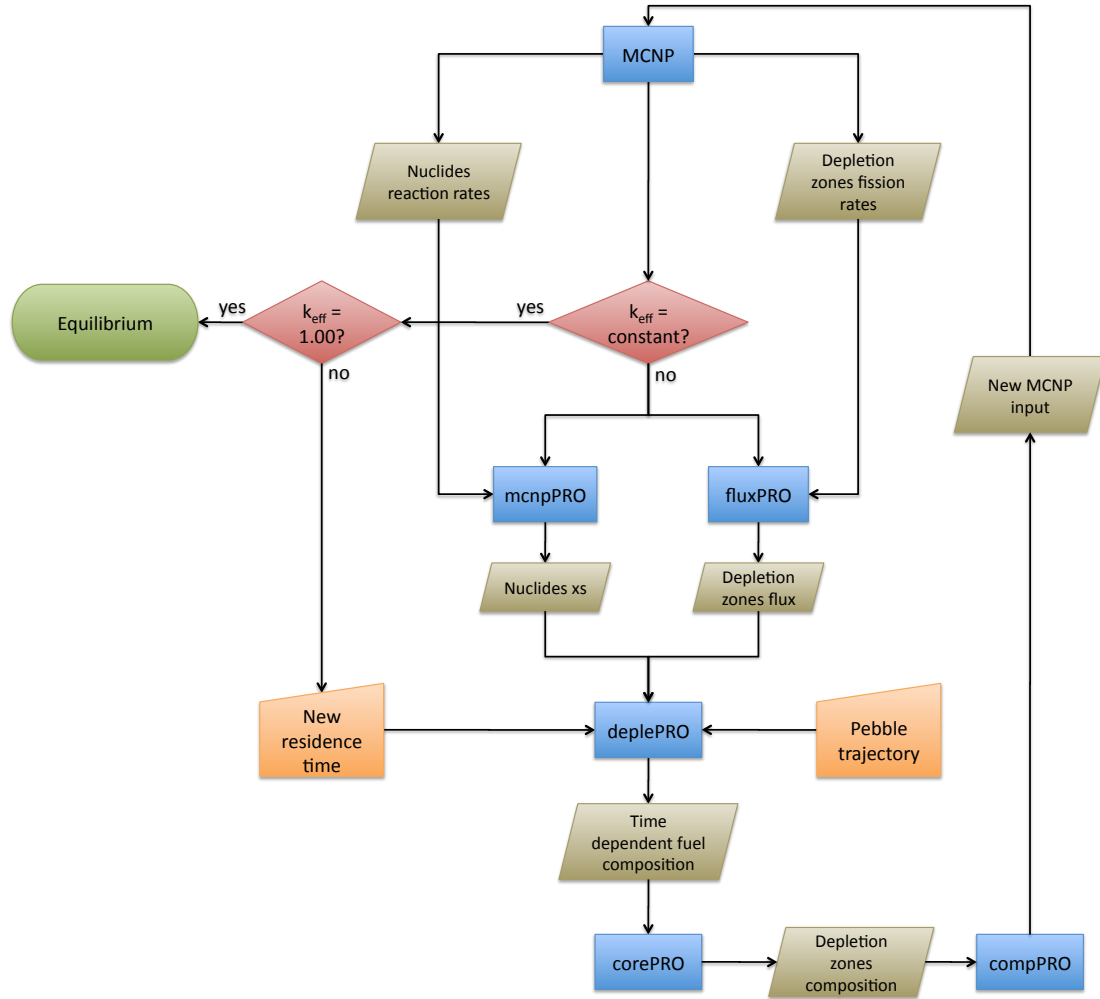


Figure 2.15 Flow chart of the full core depletion methodology.

This methodology can be applied both to the integral and to the modular design, but the following sample results refer to the modular design. Different zone subdivisions were considered. All of them divide the core into two macro zones—the

outer PCAs in the outer core ring that can be grouped together because of symmetry, and the central PCA. Each of the two macro zones is further subdivided into sub-zones as follow:

1. Three radially uniform axial zones—the lower plenum, the upper plenum and the channels section for both the outer PCAs and the central PCA;
2. Seven radially uniform axial zones that besides the plena include five equal length axial zones per channels section for both outer PCAs and central PCA;
3. Three axial zones, two of which—the plena—radially uniform, and one radially non-uniform zone; the outer PCAs channels section was subdivided into 13 radial zones and the central PCA channels section was subdivided into three radial zones (Figure 2.16).

Later on we will refer to these subdivision as “3 axial”, “7 axial”, and “3 axial + radial”.

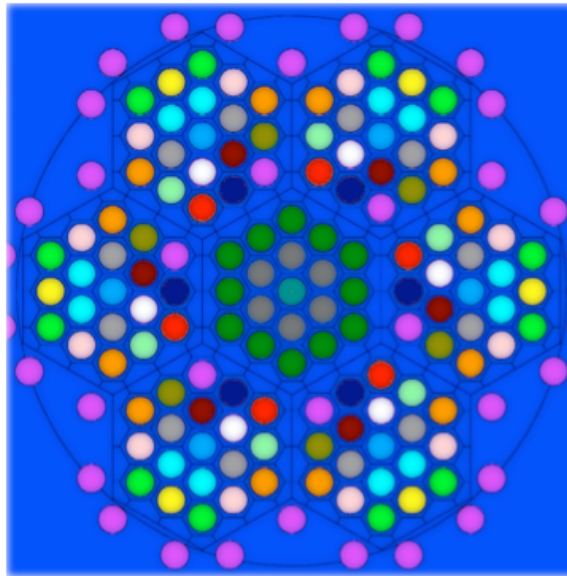


Figure 2.16 Radial depletion zones distribution in the “3 axial + radial” scheme.

In order to test the methodology and find the sensitivity of the results to the core subdivision scheme, a test case was chosen: the fuel kernel diameter was set at 325 μm and TRISO particles packing factor at 40%; fuel is 19.9% enriched uranium. The recirculation scheme assumes that pebbles circulate six times through the outer PCAs and at the seventh loop move to the inner PCA. It is also assumed that the average pebble velocity is the same in each section of the core, and the time required to recirculate the pebble from the top of the core back to the core bottom is negligible.

Figure 2.17 shows how the core k_{eff} evolves towards an equilibrium value iteration by iteration when starting from clean fuel and a uniform core composition for the three axial zones case. Reaching equilibrium required about 15 iterations, but a better initial guess for the core composition can speed up the convergence considerably.

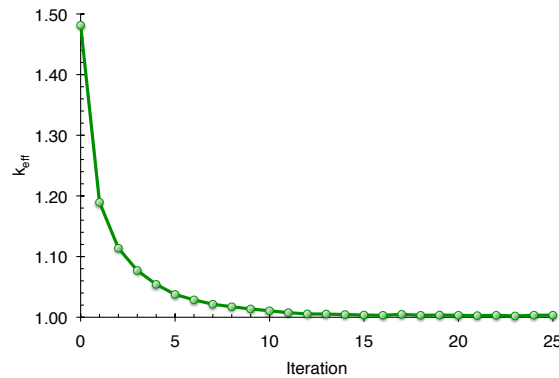


Figure 2.17 Effective multiplication factor evolution with iterations from a uniform clean fuel composition to the core equilibrium composition—three axial zones case.

Table 2.16 compares equilibrium core properties when using different zoning

approaches and same residence time. It was found that a more accurate axial burnup distribution affects the core reactivity causing a ~ 300 pcm drop, but a larger effect is obtained considering radial zones for which the reactivity drop is $\sim 1,000$ pcm. The simplest core subdivision with 3 axial zones allows a considerable run time saving but it overestimates burnup.

Table 2.16 also shows how a less detailed core zoning fails in estimating the peak power per TRISO particle. The value reported is the peak value during the entire pebble life and accounts for the following peaking factors: fuel composition peaking factor, intra-channels peaking factor, and core axial peaking factor; they do not account for channel peak factoring and inner pebble peaking factor.

Table 2.16 Comparison of selected characteristics obtained using the three core subdivision schemes.

Property	3 axial zones	7 axial zones	3 axial + radial zones
k_{eff}^a	1.00365 ± 0.00025	1.00093 ± 0.00025	0.99354 ± 0.00032
Residence time (EFPD)	256	256	256
Burnup (GWd/tHM)	215	215	215
Peak kernel power (mW)	418	477	556
Extra MCNP run time factor ^b	1.0	~ 1.2	~ 1.7

^a Average of 10 iterations after equilibrium; ^b Run time-to-3 axial zones case run time ratio.

Table 2.17 shows the sensitivity of the core multiplication factor to the pebble

residence time. A change of one day in the residence time is equivalent to ~ 400 pcm change in reactivity, and to 1 GWd/tHM in burnup. From this observation we established that the depletion scheme for burnup estimation should converge to k_{eff} values between 1.000 and 1.004.

Table 2.17. Burnup results as a function of total residence time—3 axial zones case.

Residence time (EFPD)	k_{eff}^a	Burnup (GWd/tHM)
254	1.00787 ± 0.00030	213
256	1.00365 ± 0.00025	215
258	0.99747 ± 0.00039	217

^a Average of 10 iterations after equilibrium.

The depletion methodology developed allows to reconstruct in detail the power history of the pebbles and TRISO particles. Figure 2.18 and Figure 2.19 show the pebble-average power a fuel kernel is subjected to at each pass through the PCAs once the equilibrium core composition has been established, for 3 axial zones and 7 axial zones, respectively. Figure 2.20 shows the pebble-average kernel power at each pass and for each channel.

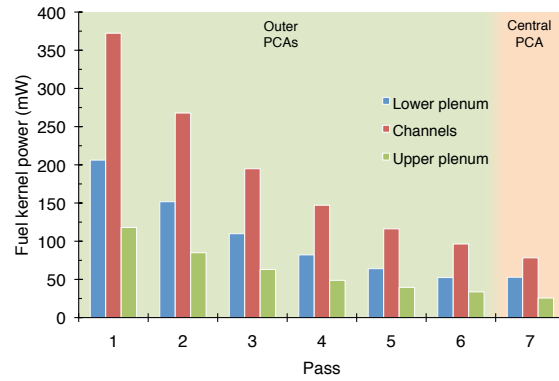


Figure 2.18 Power per fuel kernel at each pass and in each zone at equilibrium—3 axial zones case.

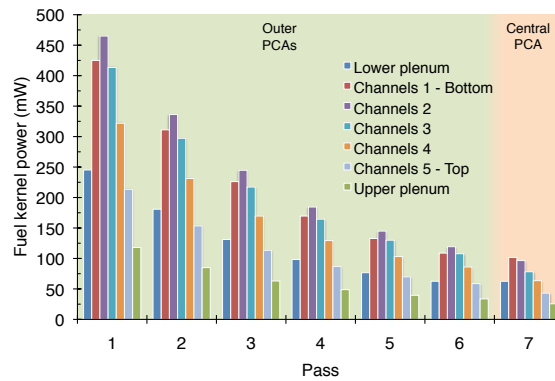


Figure 2.19 Power per fuel kernel at each pass and in each zone at equilibrium—7 axial zones case.

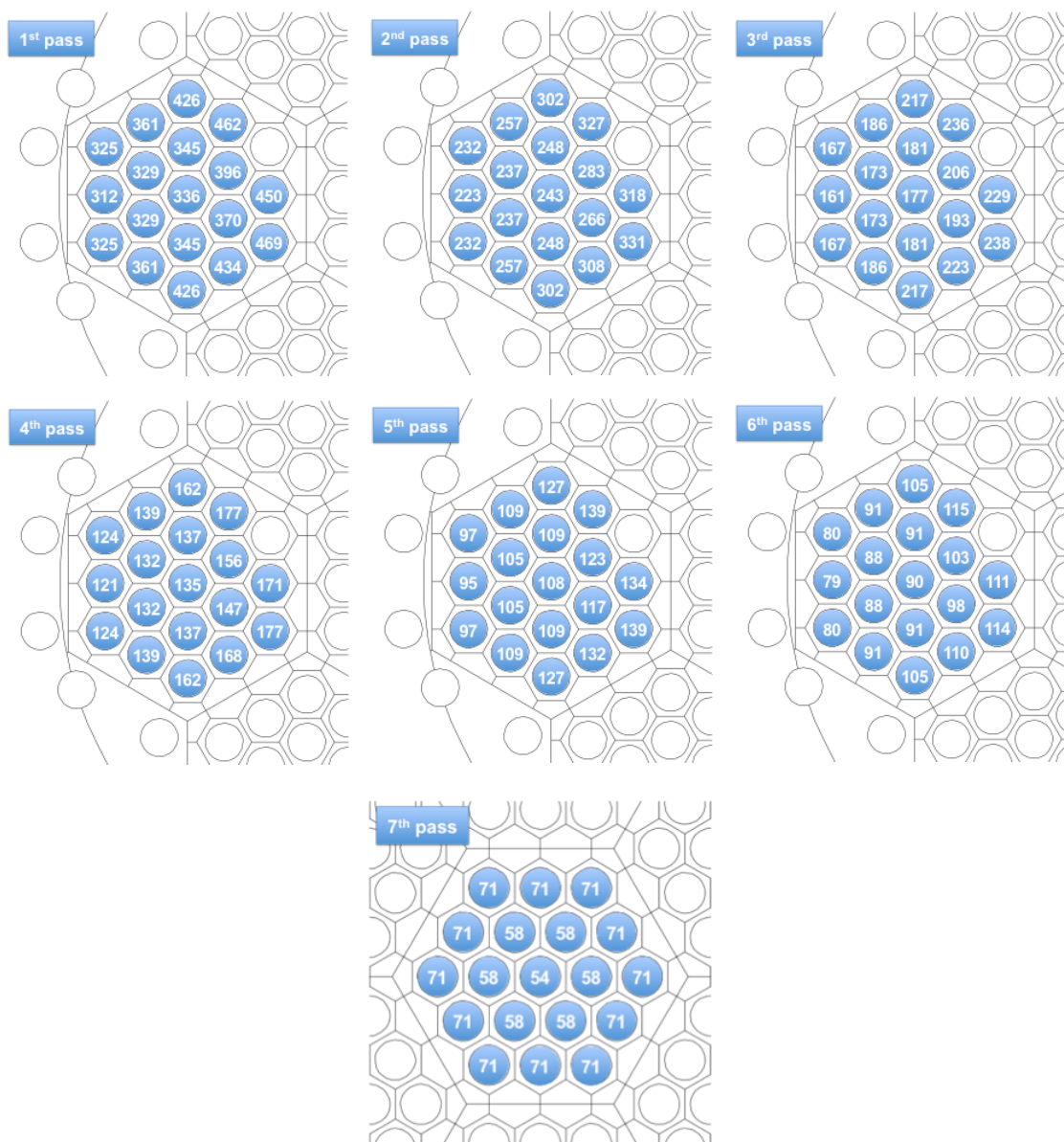


Figure 2.20 Power per fuel kernel in each channel of the outer PCAs from the first to the sixth pass and in each channel of the central PCA at the seventh pass.

3. Results

This Chapter presents the results obtained when applying the methodologies described in Chapter 2 to the integral design of the PB-AHTR fueled with 10% enriched uranium. In particular, attainable burnup and temperature and void reactivity coefficients are presented as a function of the main design variables.

3.1 Neutronics features of the PB-AHTR

The PB-AHTR is characterized by a large coolant volume fraction—40%, in the core. Furthermore the coolant is not transparent to neutrons like helium in gas-cooled pebble bed reactors. The flibe constituents feature relatively large absorption cross sections and, having a low mass numbers they function as a good moderator—the mass number of Li and Be isotopes is even smaller than that of the solid moderator, i.e. graphite. Figure 3.1 shows the neutron spectrum in the fuel kernels for the reference

design⁵ at beginning of life (BOL). This spectrum is compared to that of the same system if we assume that all the coolant is removed. This comparison reveals the double effect of the salt. The peak in the thermal energy range becomes larger when the salt moderation is accounted for, but at the same time deeps appear around the 0.1 MeV energy range in correspondence of the inelastic scattering resonances of the flibe constituents, in particular F (Figure 3.2) and ${}^6\text{Li}$ (Figure 3.3). The deeps in the spectrum between 1 eV and 1 keV, instead, appear in both cases because they are due to the ${}^{238}\text{U}$ absorption resonances (Figure 3.4).

Despite the fact that ${}^6\text{Li}$ concentration in flibe is reduced to 4 ppm at equilibrium (Section 2.2.1), the neutron absorption in the coolant is not negligible. There is ~8% of neutron loss for the reference design, mainly due to ${}^7\text{Li}$. Although it has a cross section five orders of magnitude smaller than ${}^6\text{Li}$, its concentration is six order of magnitude larger (Table 3.1).

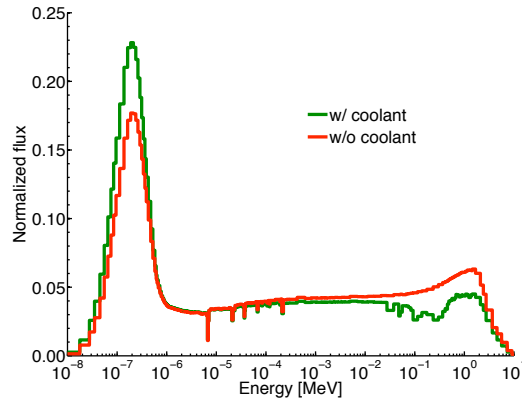


Figure 3.1 Neutron spectrum in the fuel kernels at BOL for the reference design, with and without coolant.

⁵ In this paragraph we refer to reference design as the pebble loaded with 425 μm fuel kernels and 12.5% TRISOs packing factor, that corresponds to ~360 C/HM containing 10% enriched uranium in the form of oxy-carbide ($\text{UO}_{1.5}\text{C}_{0.5}$).

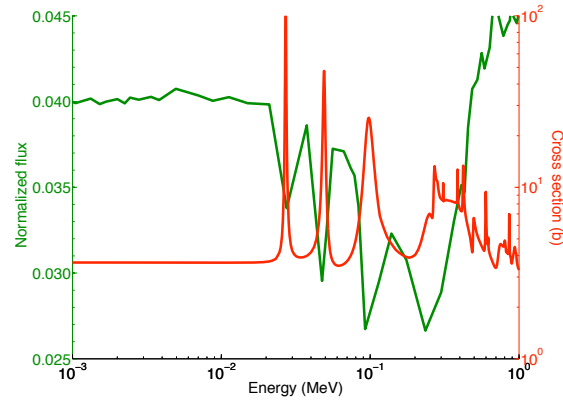


Figure 3.2 Comparison of neutron flux and F total cross section.

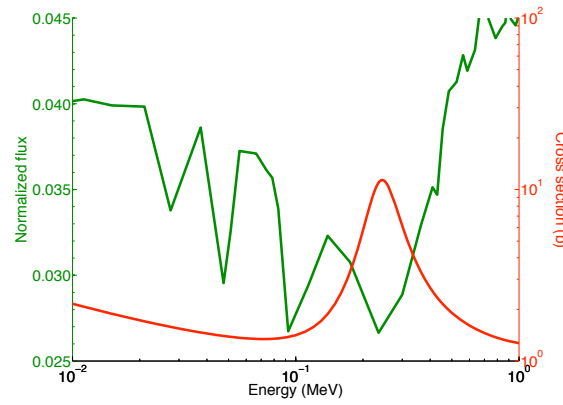
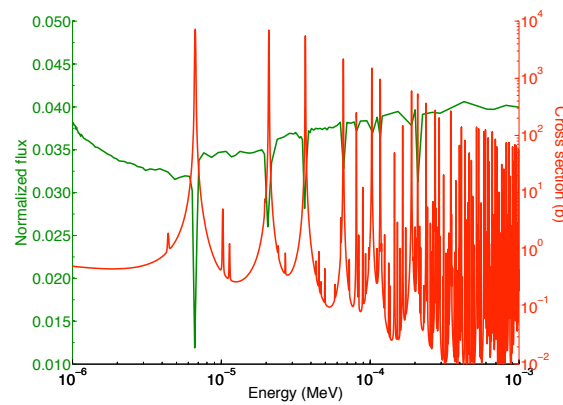
Figure 3.3 Comparison of neutron flux and total ${}^6\text{Li}$ cross section.Figure 3.4 Comparison of neutron flux and ${}^{238}\text{U}$ capture cross section.

Table 3.1 Fractional neutron absorption in the unit cell components at BOL for the reference design.

Component	Fractional absorption
Fuel kernels	89.59%
Coatings	0.60%
Graphite matrix	0.83%
Graphite structure	0.79%
^6Li	0.37%
^7Li	4.39%
^9Be	0.80%
^{19}F	2.56%
Total coolant	8.13%

3.2 Attainable burnup

The attainable burnup was determined as a function of multiple design variables, but in particular: fuel kernel diameter and graphite-to-heavy metal atom ratio (or TRISO packing factor). For this analysis the initial fuel enrichment is set at 10%, the total core power at 2,400 MW_{th}, and the core power density at 10.2 MW/m³. The core neutron leakage probability to be specified as an input to the depletion methodology, as described in Chapter 2, was determined using a full core loaded with a uniform fuel composition corresponding to the average of all pebbles in the equilibrium core; its value was found to be about 3%.

The burnup values presented in this section and in the following does not account

for the excess of reactivity at which the core operates to overcome xenon transient. It was estimated that when the power drops abruptly from 100% to 40% the core reactivity drops by about 2% because of xenon build up, therefore an equivalent reactivity excess must be maintained at any time. This requirement causes a penalty on the theoretical attainable burnup of about 10 GWd/tHM.

3.2.1 Fuel kernel diameter and C/HM

Figure 3.5 shows the attainable burnup for a wide range of combinations of fuel kernel diameter (from 225 μm to 1025 μm) and graphite-to-moderator atom ratio (from 200 to 600), and Figure 3.6 shows the corresponding residence time of the pebbles in the core. It was found that the maximum burnup is achieved with C/HM in the 300-400 range for any of the fuel kernels sizes considered, and that larger kernels reach larger burnup.

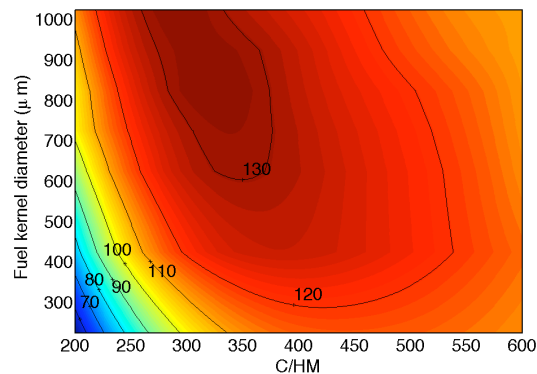


Figure 3.5 Attainable burnup (GWd/tHM) as a function of fuel kernel diameter and graphite-to-heavy metal atom ratio.

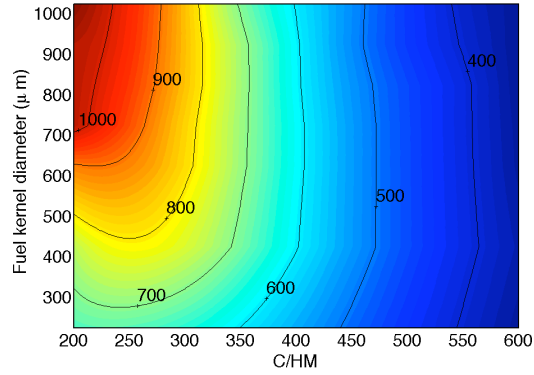


Figure 3.6 Residence time (EFPD) as a function of fuel kernel diameter and graphite-to-heavy metal atom ratio.

To understand the dependence of the attainable burnup on the kernel diameter and C/HM let us consider the two variables separately. We first fix the fuel kernel diameter at 425 μm and vary the C/HM. Figure 3.7 gives the BOL infinite multiplication factor as a function of C/HM along with two factors: f —the fraction of neutrons absorbed in the fuel kernels out of the total absorption in the pebble unit cell; and η —the number of neutrons generated per neutron absorbed in the fuel. The product of f and η is k_∞ . As C/HM increases the neutron spectrum gets softer (Figure 3.8), consequently the loss of neutrons in the salt increases and f decreases, whereas η increases (Figure 3.7). These two opposite trends define an optimal moderation point to which the maximum attainable burnup corresponds.

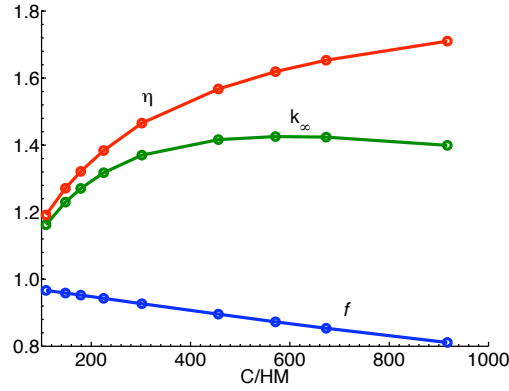


Figure 3.7 Infinite multiplication factor, fractional absorption in the fuel— f , and neutron generated per neutron absorbed in the fuel— η , as a function of graphite-to-heavy metal atom ratio for 425 μm fuel kernels.

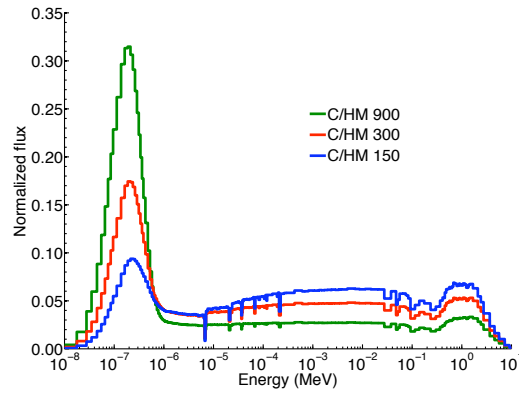


Figure 3.8 Neutron spectrum at different graphite-to-heavy metal atom ratio for 425 μm fuel kernels.

If, instead, we fix C/HM and vary the fuel kernel diameter, the neutron spectrum does not change. Therefore, the reason for the increasing burnup with kernel size must arise from the spatial self-shielding effect at the kernel level. This effect is due to a strong absorption in the resonance energy range that causes the flux in that energy range to decrease when progressively moving towards the center of the kernel. Figure 3.9 shows that when increasing the kernel diameter while maintaining C/HM constant,

the BOL f remains about constant while η increases and so does k_{∞} . This trend is due to the drop of the effective ^{238}U capture cross section from the kernel periphery towards the kernel center that is due to the spatial self-shielding; the larger the kernel the more enhanced is this cross section drop (Figure 3.10). Thus, the 825 μm kernel average ^{238}U cross section is $\sim 15\%$ smaller than that of the 425 μm kernel, while the ^{235}U cross section is not sensitive to the kernel dimensions (Table 3.2).

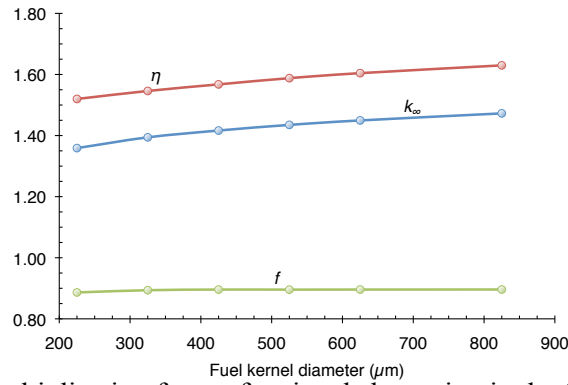


Figure 3.9 BOL multiplication factor, fractional absorption in the fuel— f , and neutron generated per neutron absorbed in the fuel— η , as a function of kernel diameter at a constant graphite-to-heavy metal atom ratio (~ 360).

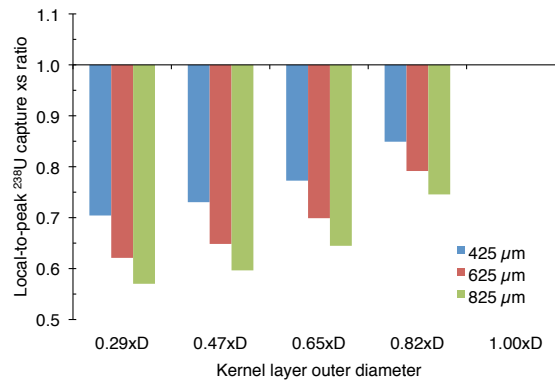


Figure 3.10 Local-to-peak ^{238}U effective 1-g capture cross section as a function of radial position in the kernel and kernel diameter at a constant graphite-to-heavy metal atom ratio (~ 360)—BOL, 10% enriched uranium.

Table 3.2 BOL kernel average effective 1-g cross sections for selected kernels diameter—360 C/HM graphite-to-heavy metal atom ratio, 10% enriched uranium.

Kernel diameter (μm)	Cross section (b)		
	^{235}U fission	^{235}U capture	^{238}U capture
425	99.32	20.92	4.42
625	100.41	21.06	4.05
825	100.02	20.98	3.76

3.2.2 Power density and total core power

The core power density was initially fixed to be 10.2 MW/m^3 but the thermal-hydraulic analysis found possible for the PB-AHTR to reach much higher power density with acceptable temperatures and transient response. The achievable burnup was therefore determined for power densities of 20 MW/m^3 and 40 MW/m^3 while keeping the total core power constant and adjusting the core dimensions and the neutron leakage probability. Table 3.3 compares selected characteristics of three PB-AHTR core designs having different power density. The attainable burnup of the highest power density core drops by 13-14 GWd/tHM relative to the low power density core due to the enhanced neutron leakage probability caused by the smaller core size.

If the total core power is reduced, the design would suffer the same consequences: reduced core dimensions, enhanced leakage, and lower attainable burnup (Table 3.4).

Table 3.3 Attainable burnup as function of core power density—reference pebble design.

Property	Power density (MW/m ³)		
	10.2	20	40
Core diameter (cm)	684	547	434
Core active length (cm)	640	514	408
Leakage (%)	3	4	6
Flux (n/cm ² -s)	$3.36 \cdot 10^{14}$	$6.45 \cdot 10^{14}$	$1.26 \cdot 10^{15}$
Burnup (GWd/tHM)	129	114	113
Residence time (EFPD)	672	303	149

Table 3.4 Attainable burnup as function of total core power—reference pebble design, 10.2 MW/m³.

Property	Core power (MW _{th})	
	2,400	600
Core diameter (cm)	684	431
Core active length (cm)	640	405
Leakage (%)	3	6
Flux (n/cm ² -s)	$3.36 \cdot 10^{14}$	$3.20 \cdot 10^{14}$
Burnup (GWd/tHM)	129	113
Residence time (EFPD)	672	589

3.2.3 Spatial self-shielding effect on attainable burnup

In Section 3.2.1 we showed that the spatial self-shielding facilitates larger kernels to reach higher burnup levels. In this Section we further investigate the phenomenon by performing a radial dependent depletion instead of assuming a uniform depletion across the kernel. The double heterogeneity of the fuel is also reflected in a double

spatial self-shielding effect, one at the kernel level and one the pebble level. The two effects are treated separately. The analysis is performed for the reference pebble design.

3.2.3.1 *Self-shielding at the kernel level*

To evaluate the self-shielding effect in the kernels, they were divided into five spherical layers the outer diameters of which are 125 μm , 200 μm , 275 μm , 350 μm and 425 μm . The burnup calculations were carried out depleting separately each of these zones. The average flux amplitude in the kernels was assumed to be constant through the pebble and its value was obtained from the equilibrium core found in previous burnup calculations. The flux amplitude in each layer, instead, was determined using the local-to-average flux ratio as determined using flux tallies in MCNP.

Table 3.5 summarizes results obtained at beginning of life. It shows that the flux and power distributions are quite uniform through the kernels. The conversion ratio⁶ (CR) behaves differently, and decreases moving toward the kernel center. The reason for this trend is the radial change of ^{238}U effective capture cross section, that is larger in the outer part of the kernels—as we would expect from spatial self-shielding.

⁶ Conversion ratio is defined as fissile generated-to-fissile consumed ratio, and the fissile vector is limited to ^{235}U , ^{239}Pu and ^{241}Pu .

Table 3.5 BOL pebble properties as a function of kernel layer.

Property	Kernel layer outer diameter (μm)				
	125	200	275	350	425
Local specific power-to-kernel average specific power ratio	0.996	0.996	0.998	0.999	1.002
Conversion ratio	0.26	0.27	0.29	0.32	0.37
^{235}U fission xs (b)	98.91	98.96	99.08	99.26	99.54
^{235}U capture xs (b)	20.82	20.83	20.86	20.90	20.97
^{238}U capture xs (b)	3.50	3.63	3.84	4.22	4.97

During depletion the power peaking factor increases as shown in Figure 3.10, reaching a maximum at end of life (EOL) of ~ 1.08 . The CR, as well, remains larger in the outer region, but differences become smaller towards EOL (Figure 3.12). As expected from the power distribution, the outer region of the kernel reaches a larger burnup (Figure 3.13).

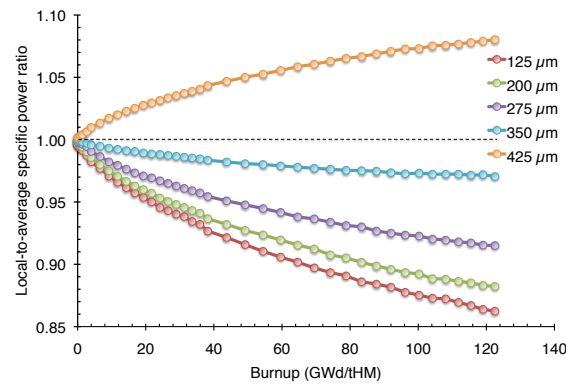


Figure 3.11 Local specific power-to-kernel average specific power as a function of average burnup in selected kernel zones.

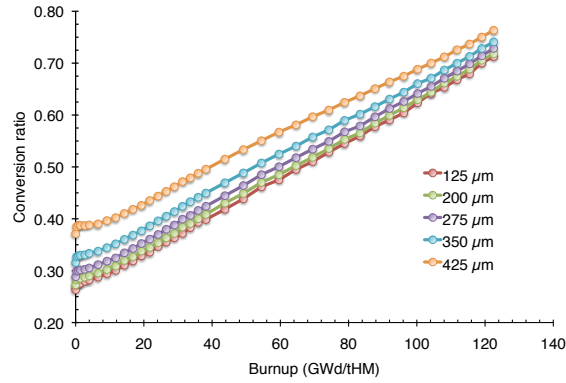


Figure 3.12 Conversion ratio as a function of kernel average burnup in selected kernel zones.

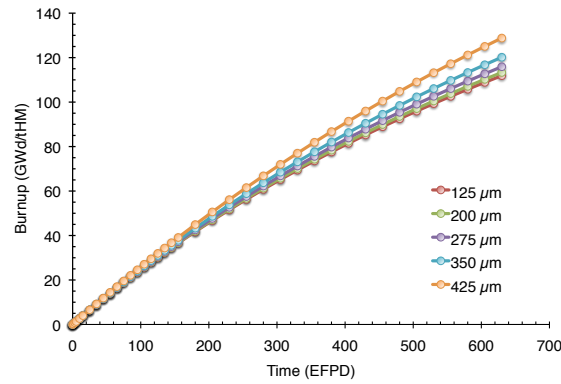


Figure 3.13 Zone-dependent burnup as a function of depletion time.

Table 3.6 compares the concentration of selected actinides and total fission products across the kernel at EOL. The total concentration of HM and fission products are, respectively, inversely proportional and proportional to the power level. Uranium, both 235 by fission and 238 by capture, is consumed faster in the outer layer of the kernels, where plutonium is preferentially accumulated.

Table 3.6 EOL fuel isotopic composition in each kernel layer (atoms/b-cm).

Nuclide	Kernel layer outer diameter (μm)				
	125	200	275	350	425
^{235}U	$2.537 \cdot 10^{-4}$	$2.532 \cdot 10^{-4}$	$2.527 \cdot 10^{-4}$	$2.523 \cdot 10^{-4}$	$2.512 \cdot 10^{-4}$
^{238}U	$1.982 \cdot 10^{-2}$	$1.977 \cdot 10^{-2}$	$1.969 \cdot 10^{-2}$	$1.955 \cdot 10^{-2}$	$1.926 \cdot 10^{-2}$
^{239}Pu	$1.215 \cdot 10^{-4}$	$1.252 \cdot 10^{-4}$	$1.316 \cdot 10^{-4}$	$1.424 \cdot 10^{-4}$	$1.635 \cdot 10^{-4}$
^{240}Pu	$9.172 \cdot 10^{-5}$	$9.429 \cdot 10^{-5}$	$9.894 \cdot 10^{-5}$	$1.0692 \cdot 10^{-4}$	$1.221 \cdot 10^{-4}$
^{241}Pu	$6.153 \cdot 10^{-5}$	$6.348 \cdot 10^{-5}$	$6.702 \cdot 10^{-5}$	$7.290 \cdot 10^{-5}$	$8.459 \cdot 10^{-5}$
^{242}Pu	$6.854 \cdot 10^{-5}$	$7.087 \cdot 10^{-5}$	$7.507 \cdot 10^{-5}$	$8.210 \cdot 10^{-5}$	$9.625 \cdot 10^{-5}$
Total HM	$2.081 \cdot 10^{-2}$	$2.078 \cdot 10^{-2}$	$2.071 \cdot 10^{-2}$	$2.060 \cdot 10^{-2}$	$2.039 \cdot 10^{-2}$
Total FP	$4.063 \cdot 10^{-3}$	$4.114 \cdot 10^{-3}$	$4.206 \cdot 10^{-3}$	$4.359 \cdot 10^{-3}$	$4.666 \cdot 10^{-3}$

Results obtained for the model above, where the kernels are divided into five layers, were compared with a model where the kernel is uniformly depleted for the same test case. It was found that the infinite multiplication factor and burnup predictions are not sensitive to refinement of the depletion analysis to sub-kernel spatial resolution (Figure 3.14 and Figure 3.15).

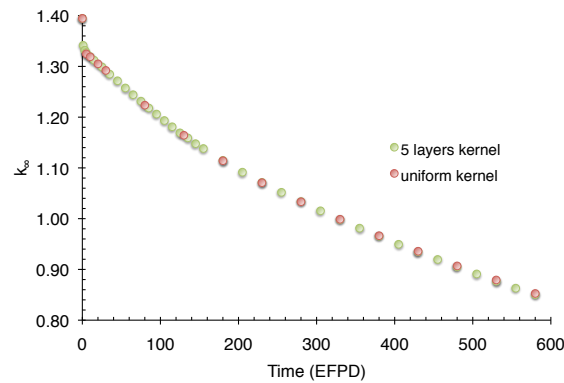


Figure 3.14 Comparison of k_{∞} as a function of depletion time for five layers and uniform kernel models.

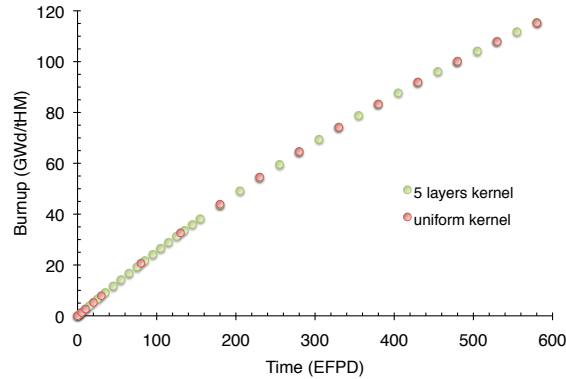


Figure 3.15 Comparison of burnup as a function of depletion time for five layers and uniform kernel models.

3.2.3.2 Self-shielding at the pebble level

The spatial self-shielding effect at the pebble level was analyzed by dividing the part of the pebble containing fuel into five regions that are separated by spherical shells of 1 cm, 2 cm, 3 cm, 4 cm and 5 cm in diameter, and depleting each of these regions separately. As done for the kernels, the pebble average flux amplitude was assumed constant while the region flux was determined at every depletion step by the ratio of the zone-to-pebble flux deduced from flux tallies taken by MCNP.

The results obtained are very similar to those found for the kernels. The power distribution at BOL is quite flat, whereas the CR is significantly larger in the outer region of the pebble. As burnup increases, the power tends to increase in the outer region (Figure 3.16) and the CR tends to become more uniform across the pebble (Figure 3.18). The power peaking at EOL is ~ 1.03 , smaller compared to the ~ 1.08 caused by the spatial self-shielding in the kernels.

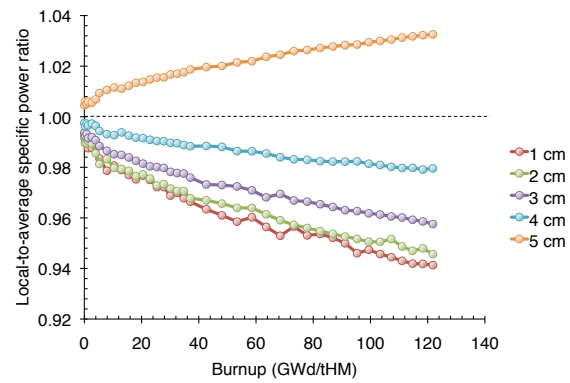


Figure 3.16 Local specific power-to-pebble average specific power as a function of average burnup in selected pebble regions.

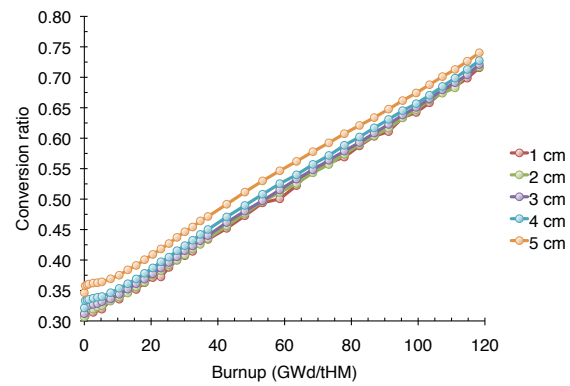


Figure 3.17 Conversion ratio as a function of kernel average burnup in selected pebble regions.

Table 3.7 EOL fuel isotopic composition in each kernel layer (atoms/b-cm).

Nuclide	Kernels layer outer diameter (μm)				
	125	200	275	350	425
²³⁵ U	2.608·10 ⁻⁴	2.611·10 ⁻⁴	2.600·10 ⁻⁴	2.581·10 ⁻⁴	2.548·10 ⁻⁴
²³⁸ U	1.963·10 ⁻²	1.962·10 ⁻²	1.959·10 ⁻²	1.954·10 ⁻²	1.940·10 ⁻²
²³⁹ Pu	1.370·10 ⁻⁴	1.381·10 ⁻⁴	1.405·10 ⁻⁴	1.447·10 ⁻⁴	1.549·10 ⁻⁴
²⁴⁰ Pu	1.032·10 ⁻⁴	1.044·10 ⁻⁴	1.058·10 ⁻⁴	1.084·10 ⁻⁴	1.150·10 ⁻⁴
²⁴¹ Pu	7.003·10 ⁻⁵	7.060·10 ⁻⁵	7.188·10 ⁻⁵	7.406·10 ⁻⁵	7.964·10 ⁻⁵
²⁴² Pu	7.746·10 ⁻⁵	7.802·10 ⁻⁵	7.952·10 ⁻⁵	8.241·10 ⁻⁵	8.944·10 ⁻⁵
Total HM	2.068·10 ⁻²	2.067·10 ⁻²	2.065·10 ⁻²	2.060·10 ⁻²	2.049·10 ⁻²
Total FP	4.249·10 ⁻³	4.262·10 ⁻³	4.296·10 ⁻³	4.360·10 ⁻³	4.513·10 ⁻³

3.3 Reactivity coefficients

This section examines the reactivity feedback mechanisms of the PB-AHTR. The analysis is based on a unit cell model and the coefficients were determined first for a pebble as a function of the burnup level and then they were projected to the core level. A core average reactivity coefficient was estimated from the change in the core multiplication factor as follows:

$$\text{Equation 3.1 } \Delta\rho = \rho_{\text{perturbed}} - \rho_{\text{nominal}} = \frac{k_{\text{perturbed}} - k_{\text{nominal}}}{k_{\text{perturbed}} k_{\text{nominal}}}$$

where k and ρ are, respectively, the multiplication factor and reactivity of the core either at nominal conditions or in a perturbed condition as indicated by the subscript. The core multiplication factor was determined by averaging the k obtained for a single

pebble at different burnup levels. Under the assumption of a well-mixed core it is (as in Chapter 2, Equation 2.10):

$$\text{Equation 3.2 } \frac{1}{k^{core}} = \sum_{j=1}^m \frac{f_j}{k^{pebble}(BU_j)}$$

where f_j is the fraction of power out of the total core power generated in a pebble at burnup level BU_j and m is the number of burnup steps considered. Equation 3.2 was applied to the core both at nominal and at perturbed operating conditions. In the later case it was assumed that the power distribution does not vary significantly with the perturbation.

3.3.1 SCALE model

The reactivity feedback mechanisms were analyzed using the CSAS sequence (Goluoglu, et al. 2006) of the SCALE 5.1 code system. Even though this sequence does not have depletion capability, it can calculate the multiplication factor properly accounting for double heterogeneity as it exists in pebble bed systems. A deterministic code is preferred over a stochastic code for the calculation of the reactivity effect of perturbations as it can drastically reduce the required computational time.

Cross sections are processed in the CSAS sequence using the Bondarenko method (BONAMI) before being collapsed using a problem dependent point-wise

continuous flux (WORKER, CENTRM and PMC). The transport module XSDRNPM calculates k_{∞} . The process is repeated at the kernel and at the pebble level to account for double heterogeneity. The sequence can be terminated with the 1-D k_{∞} estimation by XSDRNPM (CSAS1) or can be coupled with KENO-V.a for a 3-D evaluation (CSAS25). In the case of a single pebble model with reflective boundary conditions, perfect agreement was found between XSDRNPM and KENO-V.a k_{∞} values. Satisfactory agreement was found between MCNP and the CSAS sequence.

The burnup dependent fuel composition obtained from the depletion analysis performed using MOCUP is used as an input to CSAS.

All reactivity feedbacks analyzed in the following Sections were determined for unit cell models with reflective boundary conditions, therefore they do not account for changes in the neutron leakage when the operating conditions are perturbed. The perturbations considered, in particular an increase in coolant temperature and consequent density drop and an increase in moderator temperature and consequent expansion, result in an increase of neutron leakage probability and negative reactivity feedback. For this reason the results reported below are considered conservative.

3.3.2 Results

Four main reactivity feedback mechanisms in the PB-AHTR were examined: (1) change of the fuel temperature; (2) change of the coolant temperature; (3) formation of

voids in the coolant; (4) change of the moderator temperature. Each of these mechanisms was analyzed for multiple combinations of fuel kernel diameters and C/HM ratios.

3.3.2.1 Fuel temperature

The fuel temperature reactivity coefficient (FTRC) was obtained by increasing the fuel kernel temperature by 100 K and maintaining all other components, including the TRISO coatings, at the nominal operating temperature so as to encompass the Doppler effect only. It was found that: the FTRC is always negative for any combination of fuel kernel diameter and C/HM (Figure 3.18); the smaller the kernel and the lower the C/HM, the more negative the fuel temperature feedback is. As the spatial self-shielding effect is more pronounced in larger kernels, the Doppler broadening of those resonances is less effective as the kernel size increases (Figure 3.19). Larger C/HM softens the spectrum, reducing the fraction of neutrons in the epithermal energy range and, consequently, the Doppler effect (Figure 3.20).

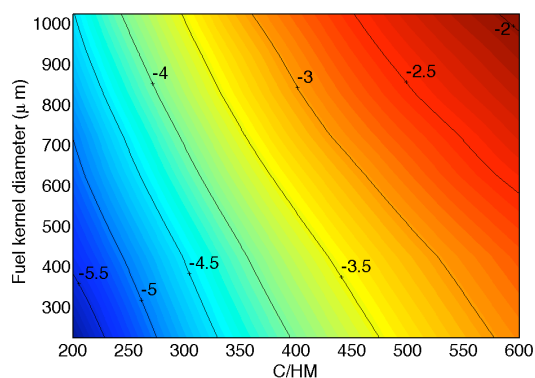


Figure 3.18 Fuel temperature reactivity coefficient (pcm/K) as a function of fuel kernel diameter and graphite-to-heavy metal atom ratio.

Figure 3.19 and Figure 3.20 show the burnup dependence of the fuel temperature feedback for selected designs. The FTRC always decreases during depletion—for enriched uranium fuel—as TRU builds up.

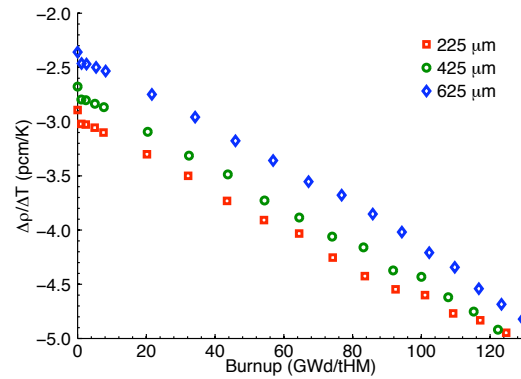


Figure 3.19 Fuel temperature reactivity coefficient as a function of pebble burnup level for selected fuel kernel diameters and ~ 360 graphite-to-heavy metal atom ratio.

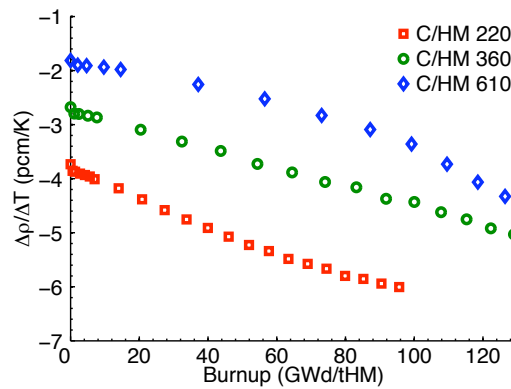


Figure 3.20 Fuel temperature reactivity coefficient as a function of pebble burnup level for selected graphite-to-heavy metal atom ratio and 425 μm fuel kernel diameter.

3.3.2.2 Coolant temperature

The coolant temperature reactivity coefficient (CTRC) was obtained increasing the coolant temperature by 100 K to 755 °C and decreasing its density to 1.91 g/cm³ (2.49% reduction compared to the nominal conditions). Figure 3.21 shows the core average coolant temperature reactivity feedback as a function of fuel kernels diameter and C/HM. To achieve a negative CTRC, C/HM must be below 300 to 400, depending on the kernel diameter. This zero CTRC line separates the over-moderated design domain—larger C/HM, from the under-moderated design domain—smaller C/HM. It corresponds to the maximum attainable burnup designs (Figure 3.5) that feature optimal moderation. The CTRC increases with increasing C/HM and fuel kernels diameter (Figure 3.21).

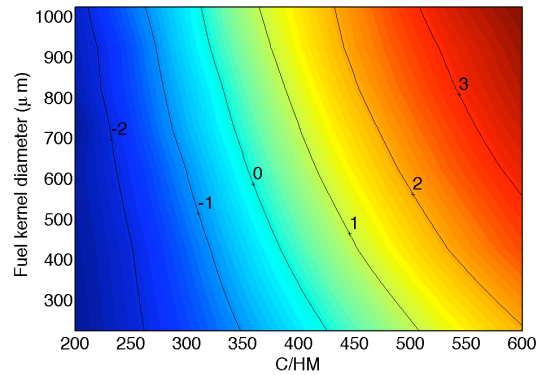


Figure 3.21 Coolant temperature reactivity coefficient (pcm/K) as a function of fuel kernel diameter and graphite-to-heavy metal atom ratio.

Figure 3.22 shows how the CTRC varies with the pebble burnup level for the reference design. After an initial jump that is due to fission products buildup, the

CTRC decreases to reach a minimum at about half way and then increases and becomes positive toward EOL. This trend is a consequence of two phenomena that are affected by the increase of the coolant temperature: (1) an absorption effect—a drop in the neutron absorption by the expanding coolant; (2) a spectral effect—spectrum hardening due to coolant temperature increase and reduced density. The absorption effect results in an increase of f causing a positive reactivity insertion. This positive effect increases with burnup because the fuel absorption cross section decreases with fuel depletion making the fuel less competitive with the flibe in absorbing neutrons.

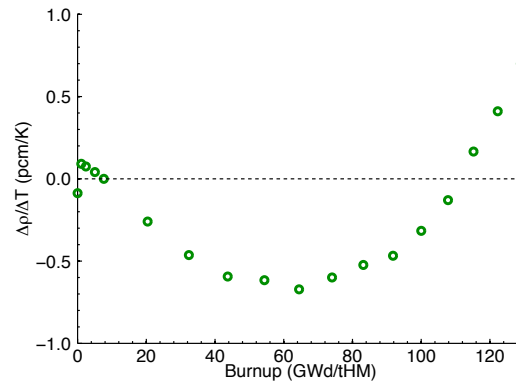


Figure 3.22 Coolant temperature reactivity coefficient as a function of burnup for the reference design.

Figure 3.23 shows the contribution of the coolant temperature increase and of the coolant density drop to the spectral effect at BOL. Shown in the figure is the effect of three different perturbations: decrease of the coolant density by 2.49%; increase of the coolant temperature by 100 K; the combined effect of the above. When the salt density is reduced (due to thermal expansion) there is a depletion in the neutron flux dipping

around 0.1 eV. As a result the η value of the fissile isotopes that have a pronounced resonance below 0.1 eV, in particular ^{239}Pu and ^{241}Pu (Figure 3.24), drops. The resulting reactivity effect is either negative or positive (Figure 3.25) depending on the concentration of the fissile plutonium isotopes. Figure 3.28 shows how the decreasing/increasing trend of $\Delta\eta$ due to only coolant temperature increase is correlated with the concentration of ^{239}Pu . This thermal spectrum shift affects f as well because it decreases the effective microscopic thermal neutron absorption of the fuel (Figure 3.26). The effect is largest towards EOL when the coolant fractional absorption is the largest. The net reactivity effect of increasing the coolant temperature without changing its density (not a physical scenario) is positive at almost any burnup for the reference design (Figure 3.27).

The spectrum hardening affects both f and η according to the moderator-to-fuel volume ratio, where moderator includes the coolant, as well. If the system is under-moderated the spectrum hardening decreases η but increases f , and vice versa if the system is over-moderated. The reference design is sufficiently under-moderated that the drop of η (Figure 3.25) compensates for the increase of f (Figure 3.26) that is also boosted by the density drop of the salt, and the net reactivity effect of changing the salt density without modifying its temperature is negative for almost any burnup level (Figure 3.27).

When the density and temperature effect are combined in the CTRC, the former prevails at lower burnup, and the latter at larger burnup (Figure 3.27). The core

average coolant temperature reactivity coefficient is negative.

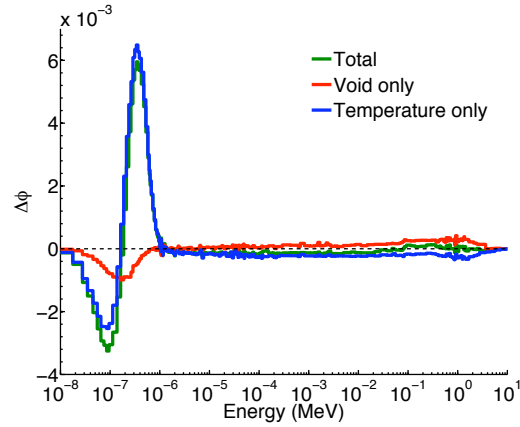


Figure 3.23 Comparison of BOL neutrons spectrum variation when the coolant temperature is increased by 100 K and its density is reduced by 2.49%, when only the coolant void fraction is reduced and when only the temperature is increased—reference design.

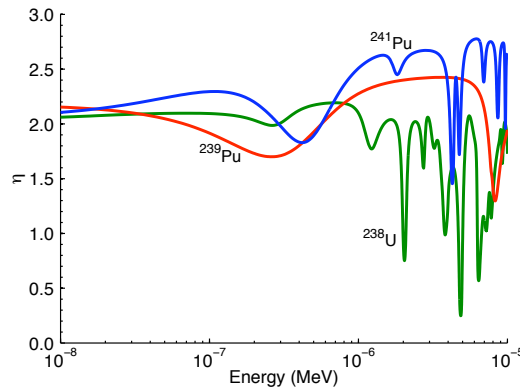


Figure 3.24 Fissile nuclides η as a function of neutron energy in the thermal range.

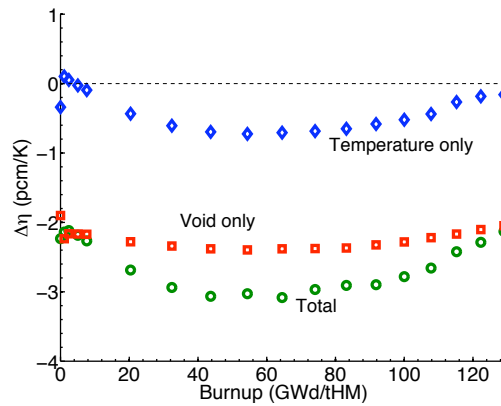


Figure 3.25 Burnup dependent variation of the neutrons produced per neutron absorbed in the fuel kernels when the coolant temperature is increased by 100 K and its density is reduced by 2.49%, when only the coolant void fraction is reduced and when only the temperature is increased—reference design.

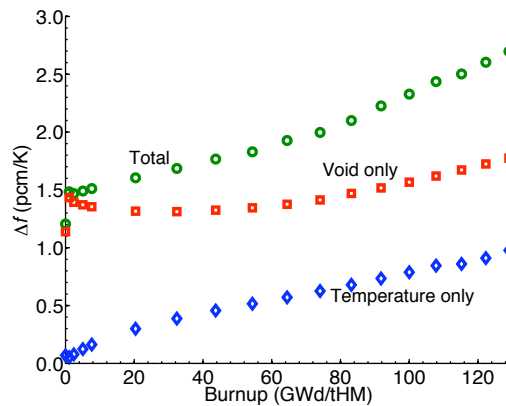


Figure 3.26 Burnup dependent variation of neutron fraction absorbed in the fuel when the coolant temperature is increased by 100 K and its density is reduced by 2.49%, when only the coolant void fraction is reduced and when only the temperature is increased—reference design.

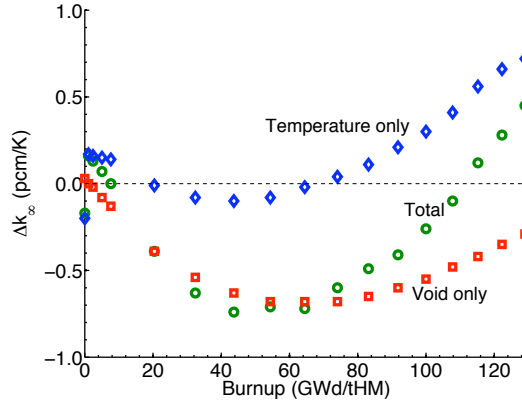


Figure 3.27 Burnup dependent variation of the infinite multiplication when the coolant temperature is increased by 100 K and its density is reduced by 2.49%, when only the coolant void fraction is reduced and when only the temperature is increased—reference design.

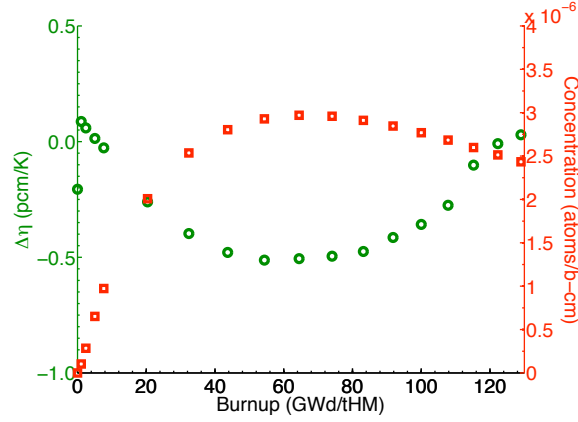


Figure 3.28 ^{239}Pu concentration and η variation due to coolant temperature increase as function of pebble burnup for 425 μm fuel kernel diameter and ~ 360 graphite-to-heavy metal ratio.

Figure 3.29 shows the burnup dependent CTTC for selected fuel kernel diameters when C/HM is fixed (~ 360). The trend is similar for all kernel sizes but the feedback is less negative or more positive for larger kernels. Since these designs feature similar spectra, the differences are due to the spatial self-shielding effect on f and η . Figure 3.30 and Figure 3.31 show how these two factors vary as a function of burnup for

selected kernel diameters. In particular, the change in η increases—becomes less negative or more positive—as the kernels get larger because the self-shielding limits the build up of fissile plutonium isotopes— ^{239}Pu in particular (Figure 3.32).

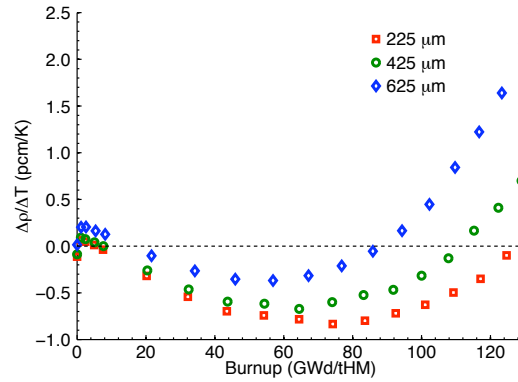


Figure 3.29 Coolant temperature reactivity effect as function of the pebble burnup level for selected fuel kernel diameters and ~ 360 graphite-to-heavy metal atom ratio.

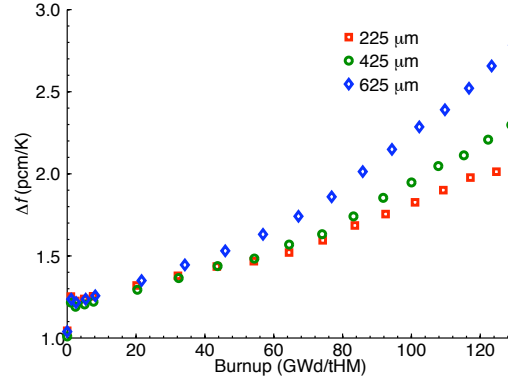


Figure 3.30 Variation of f as a function of burnup due to coolant temperature increase for selected fuel kernel diameters and constant graphite-to-heavy metal atom ratio (~ 360).

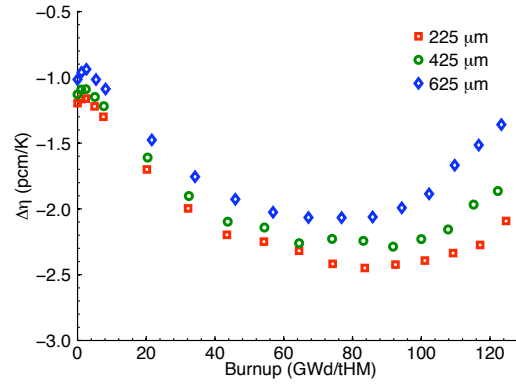


Figure 3.31 Variation of $\Delta\eta$ as a function of burnup due to coolant temperature increase for selected fuel kernel diameters and constant graphite-to-heavy metal atom ratio (~ 360).

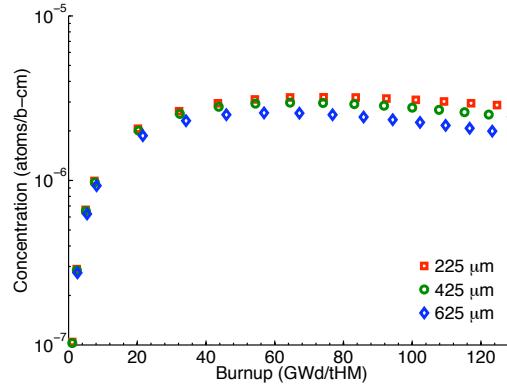


Figure 3.32 Concentration of ^{239}Pu in the kernels as a function of burnup for selected fuel kernels diameters and constant graphite-to-heavy metal atom ratio (~ 360).

Figure 3.33 shows how the CTTC varies when changing C/HM while maintaining the fuel kernel diameter constant (425 μm). It was found that the feedback is always negative for small C/HM whereas it increases and turns positive as C/HM increase and the spectrum becomes softer. In under-moderated designs absorption in the salt is strongly reduced and f is not very sensitive to small variation of the coolant density (Figure 3.34) whereas in well-moderated and over-moderated designs a significant

fraction of the neutrons is lost in the coolant and even a small changes in its density causes a significant variation in f . At the same time the small C/HM system features a more negative spectral effect revealed in a larger drop of η : the thermal spectrum shifting is less effective because the thermal spectrum component is smaller and the spectrum hardening effect becomes significant.

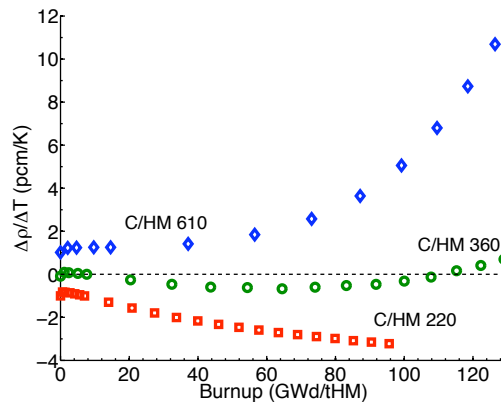


Figure 3.33 Coolant temperature reactivity coefficient as a function of the pebble burnup level for selected graphite-to-heavy metal atom ratio and constant fuel kernel diameter (425 μm).

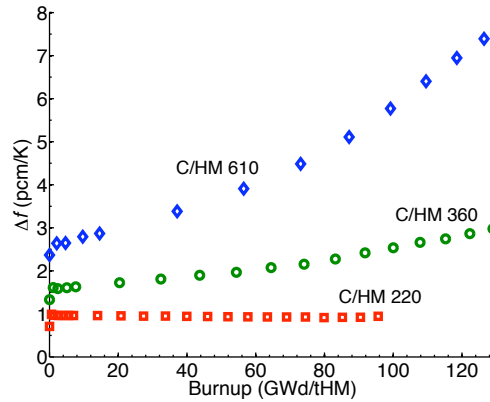


Figure 3.34 Variation of f as a function of burnup due to coolant temperature increase for selected graphite-to-heavy metal atom ratio and constant fuel kernel diameter (425 μm).

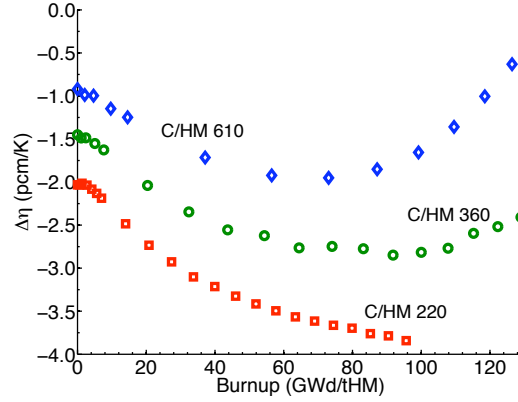


Figure 3.35 Variation of η as a function of burnup due to coolant temperature increase for selected graphite-to-heavy metal atom ratio and constant fuel kernel diameter (425 μm).

3.3.2.3 Coolant voiding

The temporary formation of voids in the coolant in the PB-AHTR could involve the ingestion of non-condensable gas such as the cover gas into the coolant. Otherwise, boiling phenomena are considered unrealistic since flibe operating and transient conditions leave large margins to the coolant boiling point, and the pool-type reactor vessel precludes any loss of coolant that would drain the core. The coolant void reactivity coefficient (CVRC) was obtained by decreasing the coolant density to 1.91 g/cm³ (-2.49% compared to the nominal conditions density), while keeping its nominal operating temperature. Figure 3.36 shows the CVRC as a function of the fuel kernels diameter and C/HM. The trend is very similar to that of the CTRC, as coolant density drop is the main contributor to the CTRC as it was observed in the previous section.

The analysis of the CVRC was basically already presented in the previous

paragraph. The reduced flibe density causes a drop in f and a spectrum hardening (Figure 3.37) with a consequent increase or decrease of η depending if the system is over-moderated or under-moderated, respectively.

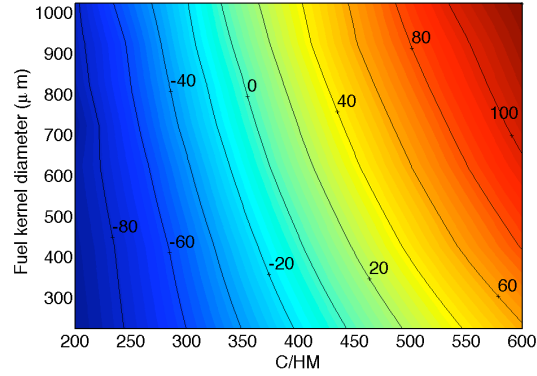


Figure 3.36 Coolant void reactivity coefficient (pcm/void%) as a function of fuel kernel diameter and graphite-to-heavy metal atom ratio.

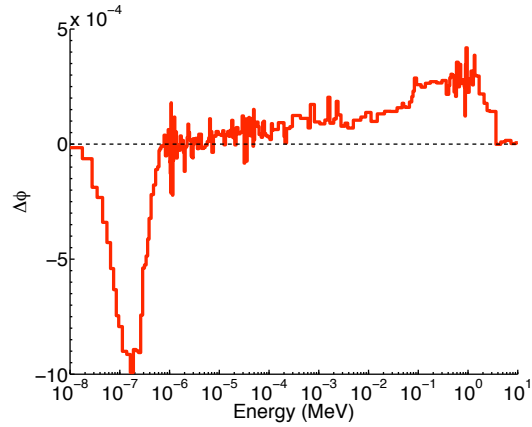


Figure 3.37 Variation of the BOL neutron spectrum when the coolant density is reduced by 2.49%—reference design.

The dependence of the CVRC on the fuel kernel size at constant C/HM is illustrated in Figure 3.38) for $C/HM \sim 360$; the smaller the kernels the more negative

CVRC is. Coolant voiding causes a more positive variation of f (Figure 3.39) and a more negative variation of η (Figure 3.40) as the kernels get smaller. The larger the kernel size the more the spatial self-shielding effect mitigates the spectrum hardening, leaving more neutrons to be absorbed in the coolant.

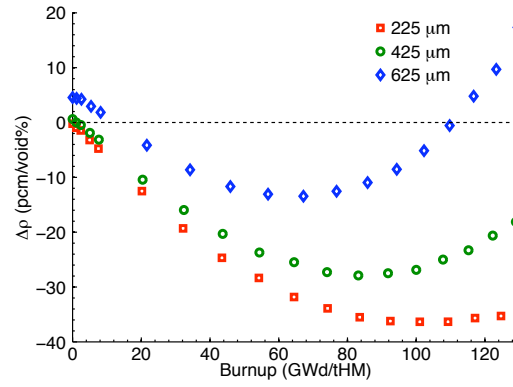


Figure 3.38 Coolant void reactivity coefficient as a function of the pebble burnup level for selected fuel kernels diameters and ~ 360 graphite-to-heavy metal atom ratio.

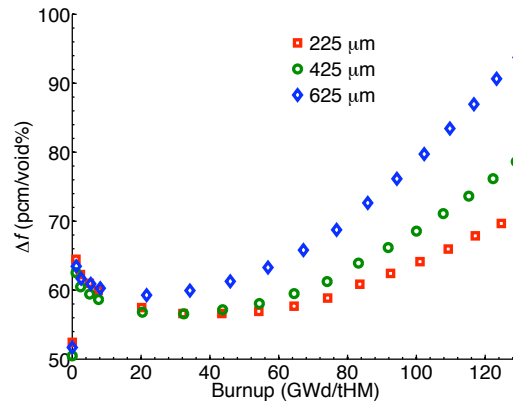


Figure 3.39 Variation of the fuel neutrons absorption fraction as function of the pebble burnup level due to coolant density drop for selected fuel kernels diameters and ~ 360 graphite-to-heavy metal atom ratio.

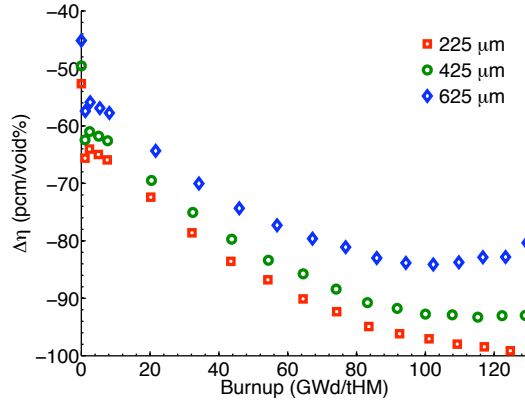


Figure 3.40 Variation of the number of neutrons produced per neutron absorbed in the fuel as a function of the pebble burnup level due to coolant density drop for selected fuel kernels diameters and ~ 360 graphite-to-heavy metal atom ratio.

If we keep the fuel kernel diameter constant ($425 \mu\text{m}$) and increase C/HM , the CVRC increases with it (Figure 3.41) and becomes positive for C/HM above 400. The softer spectra enhance coolant absorption and the voiding causes a large increase of f (Figure 3.42) that increases toward EOL because C/HM gets larger. Under-moderated systems experience a smaller drop of f and this drop slightly decreases with burnup. The variation of η is always negative (Figure 3.43) as expected from the spectrum hardening, but this variation is more negative in the under-moderated domain where η ramps up quickly with an increase of moderation as compared to the over-moderated domain where η is almost insensitive to an increase in moderation.

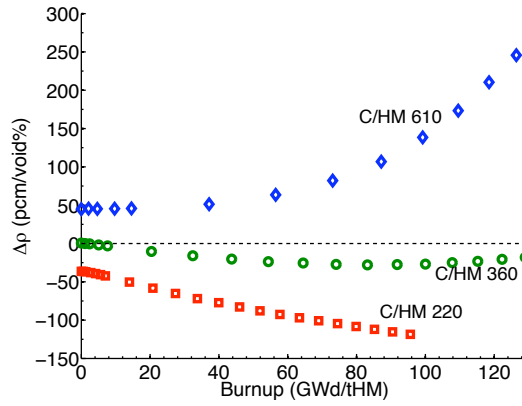


Figure 3.41 Coolant void reactivity coefficient as function of the pebble burnup level due to coolant density drop for selected graphite-to-heavy metal atom ratio and 425 μm fuel kernel diameter.

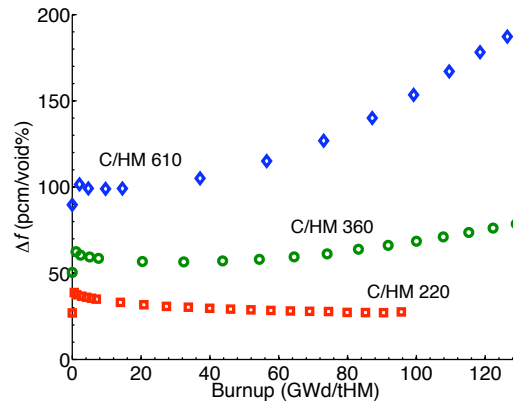


Figure 3.42 Variation of the fuel neutrons absorption fraction as function of the pebble burnup level due to coolant density drop for selected graphite-to-heavy metal atom ratio and 425 μm fuel kernel diameter.

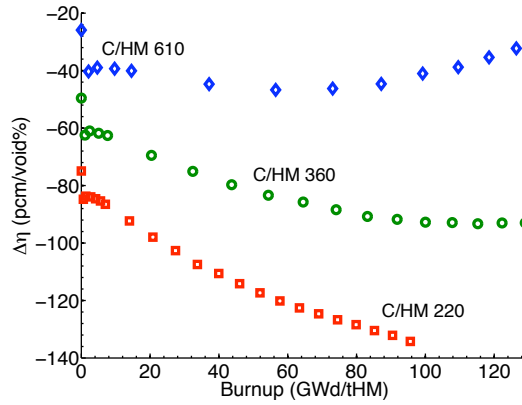


Figure 3.43 Variation of the number of neutrons produced per neutron absorbed in the fuel as function of the pebble burnup level due to coolant density drop for selected graphite-to-heavy metal atom ratio and 425 μm fuel kernel diameter.

The reactivity effect of a loss of coolant accident in which the core is completely emptied of the coolant was studied as well. Figure 3.44 shows the “full coolant void reactivity coefficient” (FVRC) as a function of the fuel kernel diameter and C/HM ratio. The full voiding of the coolant causes a strong hardening of the spectrum (Figure 3.45) and an increase in reactivity due to the elimination of neutron absorption in the liquid salt (Figure 3.46). As for small void perturbations, the overall effect is negative for smaller C/HM with the neutral line located in the 400-500 C/HM range.

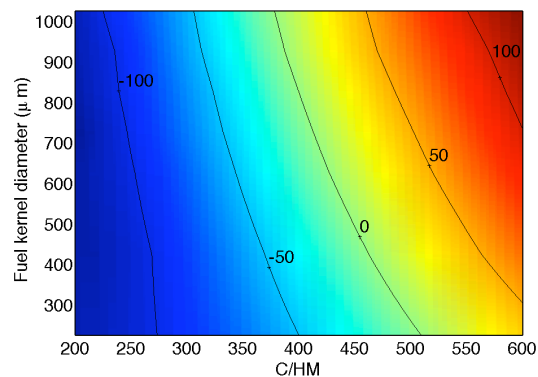


Figure 3.44 Coolant full void reactivity coefficient (pcm/void%) as a function of fuel kernel diameter and graphite-to-heavy metal atom ratio.

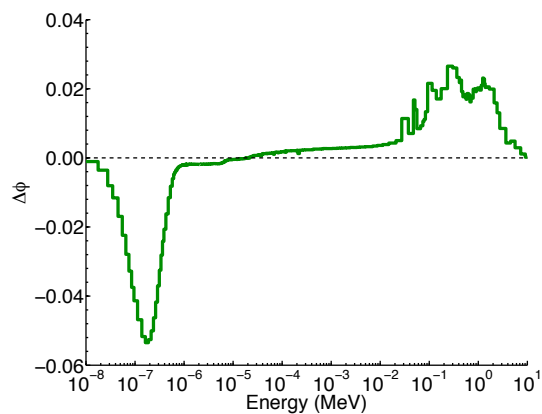


Figure 3.45 Variation of the BOL neutrons spectrum when the coolant is fully voided—reference design.

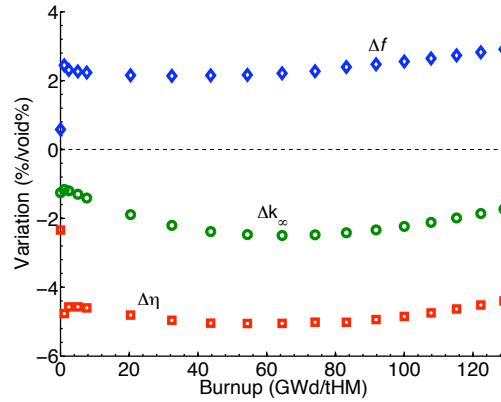


Figure 3.46 Burnup dependent variation of the multiplication factor, fractional fuel absorption and number of neutrons generated per neutron absorbed in the fuel after the coolant is fully voided—reference design.

The dependence of the FVRC on the kernel diameter and C/HM ratio resembles that already described for a small coolant density change: larger kernels feature less negative or more positive FVRC (Figure 3.47) depending on C/HM, at any burnup level. Under-moderated systems feature more negative/less positive FVRC, likewise at any burnup level (Figure 3.48).

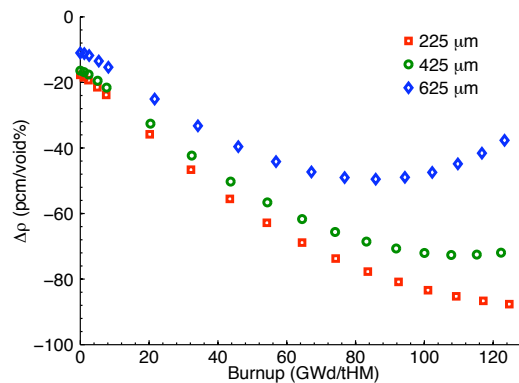


Figure 3.47 Coolant full void reactivity coefficient as function of the pebble burnup level after coolant full voiding for selected fuel kernel diameters and ~360 graphite-to-heavy metal atom ratio.

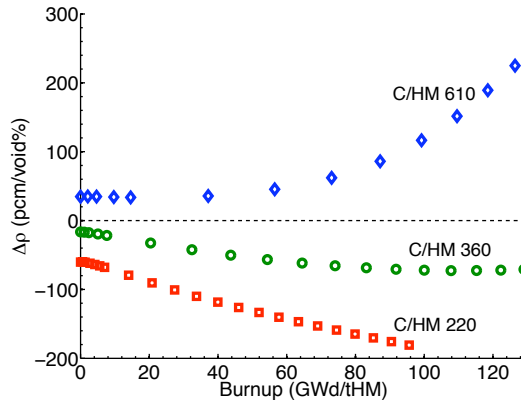


Figure 3.48 Coolant full void reactivity coefficient as function of the pebble burnup level after coolant full voiding for selected graphite-to-heavy metal atom ratio and 425 μm fuel kernel diameter.

3.3.2.4 Moderator temperature

The graphite moderator temperature can increase either by an increase in the coolant temperature or by an increase in the fuel temperature or both. Therefore this reactivity feedback is presented in combination with the coolant temperature feedback (moderator and coolant temperature reactivity coefficient—MCTRC) and with the fuel temperature feedback (moderator and fuel temperature reactivity coefficient—MFTRC). Nevertheless, with the purpose of better understanding the physical phenomena, the moderator temperature reactivity coefficient (MTRC) only was also studied separately by increasing the moderator temperature by 100 K while maintaining all the other system components at their nominal operating temperature.

For this analysis, we refer to moderator as all of the graphite in the unit cell model: TRISO coatings, matrix and pebble shell. Also, the model does not account for

the expansion of graphite that follows a temperature increase, but since the model is based on an infinite system, this effect would be irrelevant. A more accurate simulation should consider a full core model with thermal expansion, but the estimations proposed here are conservative since they neglect the enhanced leakage caused by the graphite expansion.

The MTRC dependence on the fuel kernel diameter and C/HM ratio is illustrated in Figure 3.49. Since there is no change in the actual C/HM ratio, the only consequence of raising the moderator temperature is a shift of the neutron spectrum thermal energy peak (Figure 3.50). This shift is about double in magnitude of that caused by the increase of coolant temperature (Figure 3.23). As found for the CTRC, the reactivity change is the result of a drop of η that depends on the amount of fissile plutonium in the fuel and an increase of f that is due to an increase in the ratio of effective absorption cross section of the fuel to the effective absorption cross section of the flibe (Figure 3.51). The latter effect increases with burnup.

When C/HM is fixed at ~ 360 and the fuel kernel diameter is increased, the MTRC is almost constant and becomes slightly less negative/more positive only towards EOL (Figure 3.52), when both Δf and $\Delta \eta$ increase (Figure 3.53 and Figure 3.54). As shown for the coolant temperature, the variation of η is controlled by the concentration of fissile plutonium in the fuel (Figure 3.32).

When the fuel kernel diameter is fixed at $425 \mu\text{m}$ and C/HM is increased, the MTRC increases (Figure 3.55), because in softer spectra systems f is more sensitive to

the spectral shift (Figure 3.56). Whereas $\Delta\eta$ is very similar until a burnup above 70 GWd/tHM is achieved (Figure 3.57); at this point $\Delta\eta$ starts to become more negative for systems with higher conversion ratio—faster spectrum.

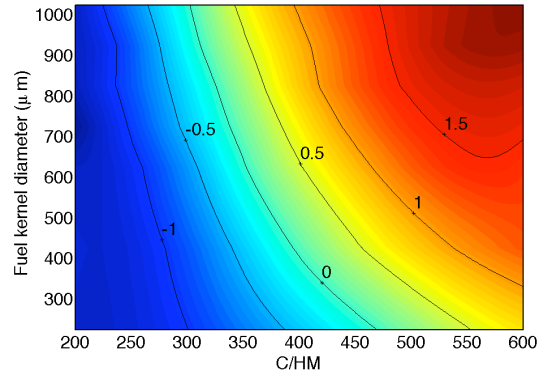


Figure 3.49 Moderator temperature reactivity coefficient (pcm/K) as a function of fuel kernel diameter and graphite-to-heavy metal atom ratio.

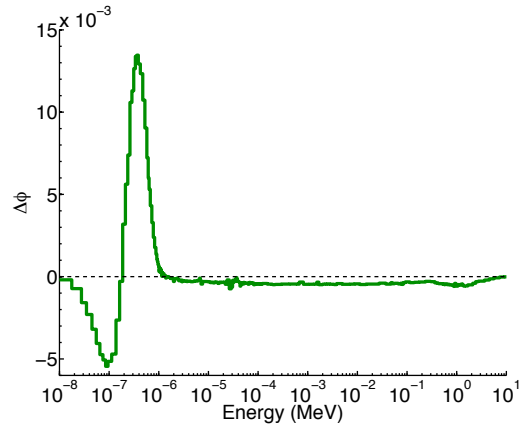


Figure 3.50 Variation of the BOL neutron spectrum when the moderator temperature is increased by 100 K—reference design.

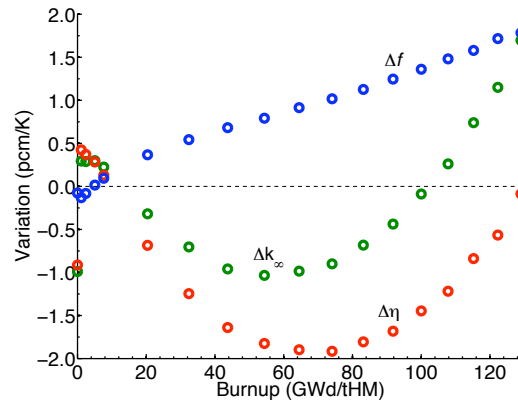


Figure 3.51 Burnup dependent variation of the multiplication factor, fractional fuel absorption and number of neutrons generated per neutron absorbed in the fuel due to moderator temperature increase—reference design.

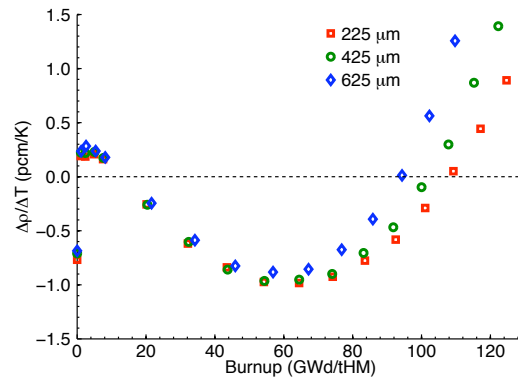


Figure 3.52 Moderator temperature reactivity coefficient as a function of the pebble burnup level due to moderator temperature increase for selected fuel kernel diameters and ~360 graphite-to-heavy metal atom ratio.

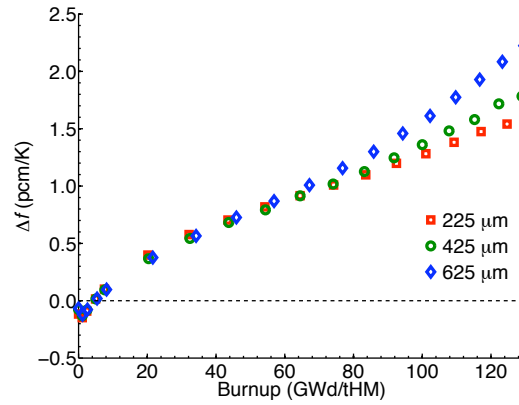


Figure 3.53 Variation of the fuel neutrons absorption fraction as a function of the pebble burnup level due to moderator temperature increase for selected fuel kernel diameters and ~ 360 graphite-to-heavy metal atom ratio.

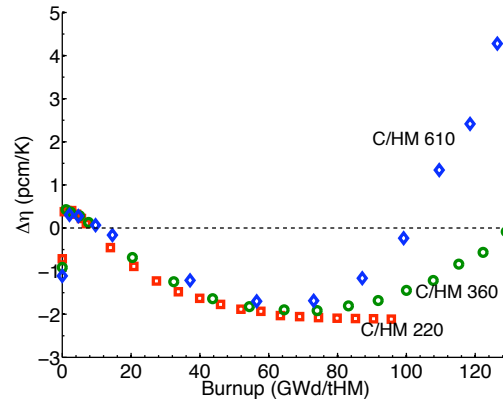


Figure 3.54 Variation of the number of neutrons produced per neutron absorbed in the fuel as function of the pebble burnup level due to moderator temperature increase for selected fuel kernel diameters and ~ 360 graphite-to-heavy metal atom ratio.

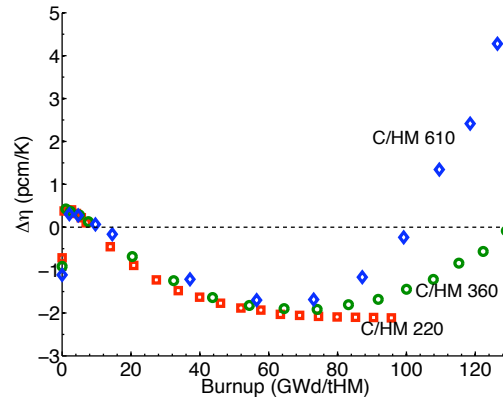


Figure 3.55 Variation of the number of neutrons produced per neutron absorbed in the fuel as function of the pebble burnup level due to moderator temperature increase for selected graphite-to-heavy metal atom ratio and 425 μm fuel kernel diameters.

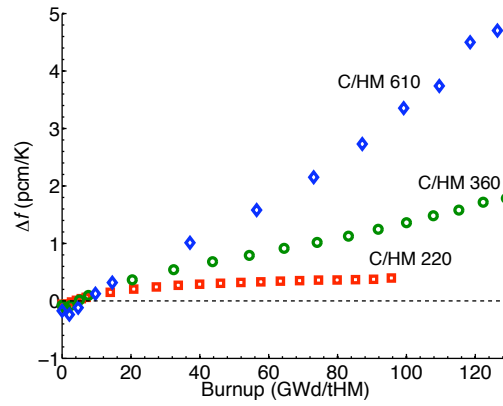


Figure 3.56 Variation of the fuel neutrons absorption fraction as function of the pebble burnup level due to moderator temperature increase for selected graphite-to-heavy metal atom ratio and 425 μm fuel kernel diameters.

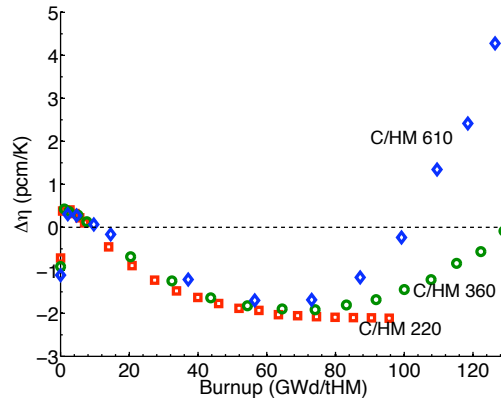


Figure 3.57 Variation of the number of neutrons produced per neutron absorbed in the fuel as function of the pebble burnup level due to moderator temperature increase for selected graphite-to-heavy metal atom ratio and 425 μm fuel kernel diameters.

The moderator effect is smaller as compared to the temperature effect per unit of temperature. Then, assuming that their temperatures raise by the same amount, the reactivity feedback is dominated by the Doppler feedback and is always negative (Figure 3.58).

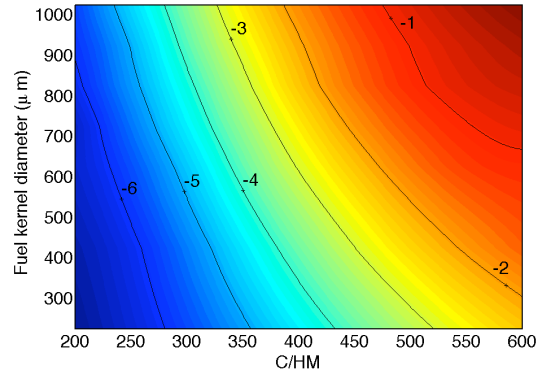


Figure 3.58 Moderator and fuel temperature reactivity coefficient (pcm/K) as a function of fuel kernel diameter and graphite-to-heavy metal atom ratio.

Since the line of neutrality for the coolant and moderator temperature feedbacks

overlap, the latter will just reinforce the former making it more negative in the under-moderated C/HM range and more positive in the over-moderated C/HM range.

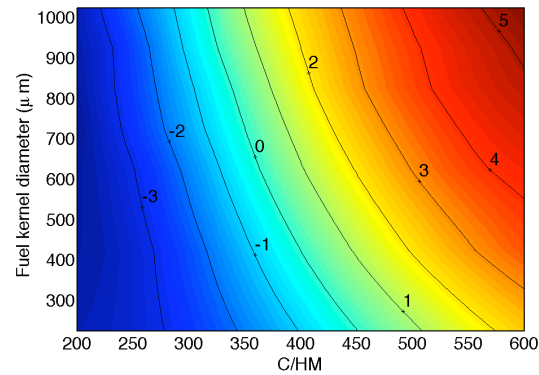


Figure 3.59 Moderator and coolant temperature reactivity coefficient (pcm/K) as a function of fuel kernel diameter and graphite-to-heavy metal atom ratio.

3.4 Summary

Table 3.8 summarizes neutronics properties of selected designs that for each kernel size feature maximum attainable burnup and all negative reactivity coefficients.

Table 3.8 Properties of selected design that for a given fuel kernel diameter, maximize the burnup while maintaining all the reactivity coefficients negative.

Property	Fuel kernel diameter (μm)		
	225	425	825
C/HM	380	363	296
Initial HM loading (gHM/pebble)	9.5	10.1	12.4
Burnup (GWd/tHM)	115	127	131
Residence time (EFPD)	567	664	847
Fuel temperature feedback (pcm/K)	-4.11	-3.95	-3.82
Coolant temperature feedback (pcm/K)	-0.59	-0.33	-0.68
Coolant void feedback (pcm/void%)	-27.6	-20.5	-33.0
Full coolant void feedback (pcm/void%)	-57.1	-53.5	-67.5
Fuel and moderator temperature feedback (pcm/K)	-4.69	-4.29	-4.22
Coolant and moderator temperature feedback (pcm/K)	-1.34	-0.87	-1.27

4. HTRs comparison

In Chapter 3 we determined what burnup can be attained in the PB-AHTR when fueled with 10% enriched uranium. In this Chapter we contrast the performance of the PB-AHTR with alternative design options proposed for High Temperature Reactors (HTRs). Besides the gas-cooled pebble bed reactor (Pebble Bed Modular Reactor—PBMR), prismatic fuel reactors were considered, both gas-cooled (Very High Temperature Reactor—VHTR) and liquid salt cooled (Liquid Salt-cooled High Temperature Reactor—LS-VHTR). For each design the maximum attainable burnup was searched as a function of C/HM for a constant kernel diameter, arbitrarily set at 425 μm . All the designs feature the same TRISO particles as described in Chapter 2, loaded with 10% enriched uranium oxy-carbide.

The following sections describe the model and assumptions used for each core design concept and summarize the results obtained.

4.1 Helium-cooled Pebble Bed Modular Reactor

The PBMR core was assumed to be cylindrical and like in the PB-AHTR, pebbles occupy 60% of the core volume and the coolant fills the remaining 40%. The thermo-physical properties of helium limit the achievable power density (Chapter 2) as compared to the liquid salt. In this analysis, the power density was assumed to be 6.6 MW/m^3 with total core power at 600 MWth (Kadak and Petti 2000). The resulting core dimensions are 498 cm diameter and 466 cm active length. Pebbles are 6 cm in diameter (5 cm diameter active section) as in the PB-AHTR, but the graphite matrix density was set at $1,740 \text{ kg/m}^3$ (Kadak, Petti et al., 2000) because it is not constrained by buoyancy requirements.

The attainable burnup was determined using the same simplified methodology as described in Chapter 2 for the PB-AHTR. Table 4.1 summarizes the results obtained for selected TRISO packing factors. The leakage probability was determined using a full core model and was found to be very sensitive to the heavy metal loading in the core. When reducing the packing factor in the PB-AHTR the advantage obtained from a more thermal spectrum (larger η) is limited and eventually overshadowed by the disadvantage of a larger absorption in the coolant (smaller f). In the PBMR this does not happen, because the coolant is transparent to neutrons and what limits the burnup is the leakage probability that gets as high as 12% when the packing factor is reduced to 5%. The maximum burnup attained is about 126 GWd/tHM with a packing factor of 5%, corresponding to C/HM of ~ 960 (Table 4.1).

Most recent PBMR designs feature an annular core to allow passive decay heat removal. In this case, the neutron leakage is expected to be larger, but the extra central graphite reflector increases the effective C/HM that potentially allows loading more HM per pebble.

Table 4.1 PBMR attainable burnup as a function of the TRISO particles packing factor.

Property	TRISO particles packing factor		
	5%	10%	15%
C/HM	960	476	315
Initial HM load (g/pebble)	4.02	8.05	12.07
Leakage (%)	11.9	9.0	8.6
Flux (n/cm ² -s)	$5.60 \cdot 10^{14}$	$2.84 \cdot 10^{14}$	$2.20 \cdot 10^{14}$
Burnup (GWd/tHM)	126	120	62
Residence time (EFPD)	407	776	601

4.2 Prismatic fuel

Classical HTRs designs from the U.S. utilize prismatic fuel elements. These are hexagonal graphite blocks penetrated by 324 holes arranged in a hexagonal lattice, 216 of which are filled with fuel and 108 are used for the coolant flow. The fuel is made of TRISO particles dispersed in a graphite matrix that forms cylindrical compacts 4.928 cm long and 1.245 cm diameter. These compacts are inserted into the fuel channels. The prismatic blocks, 79.3 cm tall and 36 cm wide flat-to-flat, are configured in a hexagonal array on multiple levels to form the active region of the core,

that can be either pseudo-annular—as in the gas-cooled model, or pseudo-cylindrical—as in the case of the liquid salt-cooled model. The number of rings of prismatic fuel blocks varies with the design (Figure 4.1). The core is surrounded with graphite reflector blocks. In case of a pseudo-annular core, graphite blocks also fill the inner volume making an inner reflector. Table 2.4 summarizes the main features the VHTR and LS-VHTR core designs (Kim, Taiwo and Yang 2005).

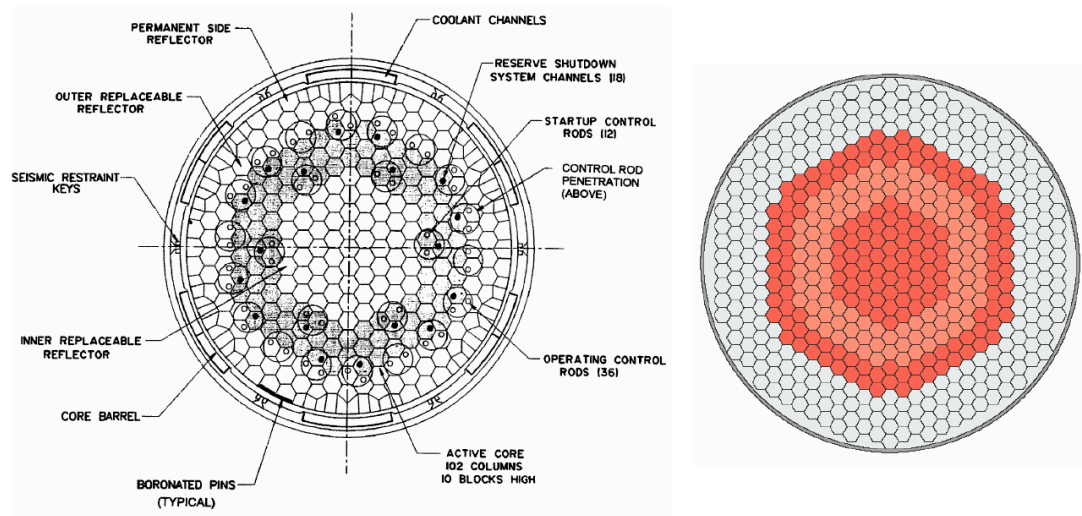


Figure 4.1 Horizontal view of the VHTR (left) and LS-VHTR (right) core.

A simplified model was used in this study to analyze the prismatic fuel reactors. It consists of a single fuel block with reflective boundary conditions on all sides (Figure 4.2). Out of the 216 fuel channels in a block, 6 are modeled as empty because in reality these channels are reserved for burnable poisons, but in this model these poisons are not taken into account.

The depletion analysis was performed assuming a uniform power across the core. A multi-batch fuel management scheme was assumed and the core average multiplication factor at any time t was determined as:

$$\text{Equation 4.1} \quad \frac{n}{k_{\infty,core}(t)} = \sum_{j=1}^n \frac{1}{k_{\infty,element}(t + T)}$$

where $k_{\infty,core}$ is the core average infinite multiplication factor, $k_{\infty,element}$ is the fuel element k_{∞} , T is the cycle length, and n is the number of batches. The cycle length was obtained by searching for $k_{\infty,core}(T)$ that would be equal to the limit value $1/P_{NL}$, where P_{NL} is the neutron non-leakage probability. For both systems the number of batches was assumed to be three (Kim, Taiwo and Yang 2005).

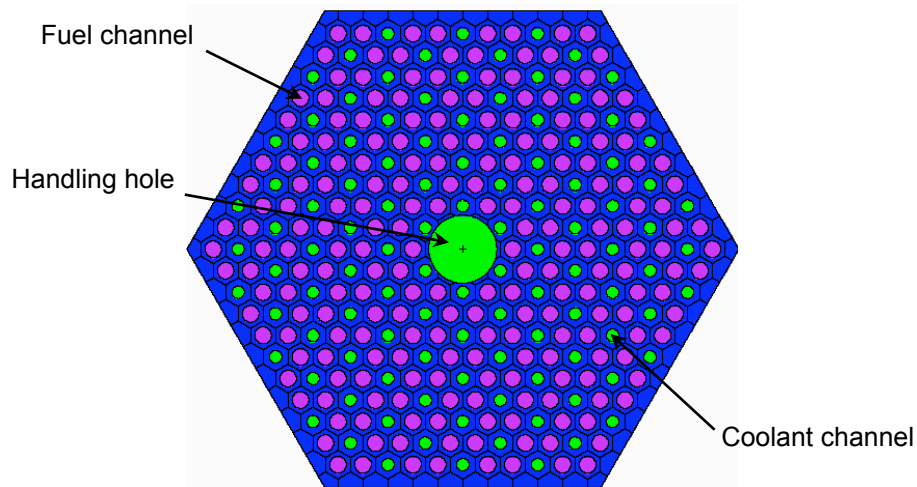


Figure 4.2 Prismatic fuel block model.

Table 4.2 LS-VHTR and VHTR models.

Property	Liquid Salt Cooled	Gas Cooled
Total Core Power (MW _{th})	2,400	600
Power density (W/cm ³)	10.2	6.6
Fuel columns	265	102
Leakage probability (%)	3	7
Fuel compact	Graphite matrix (1.74 g/cm ³)	
Fuel Element		
Flat-to-flat width (cm)		36
Height (cm)		79.3
Fuel hole diameter (cm)		1.27
Coolant hole diameter (cm)	0.953	1.5875
Holes pitch (cm)		1.8796
Fuel holes		210
Coolant holes		108
Burnable poison holes		6
Coolant		
Material	LiF-BeF ₂ (4 ppm ⁶ Li)	He
Density (g/cm ³)	1.827	0.004 (at 7 MPa)
Inlet temperature (°C)		900
Outlet temperature (°C)		1000
Average temperature (°C)		927
Fuel average temperature (°C)		1027
Graphite block (°C)		977

4.2.1 Liquid salt cooled prismatic fuel (LS-VHTR)

The fuel blocks of the LS-VHTR feature smaller diameter coolant channels (Table 2.4) because of the better heat removal capability of liquid salt compared to helium. The coolant is flibe as in the PB-AHTR and was assumed to be at its

equilibrium composition (4 ppm of ^6Li). The prismatic fuel AHTR may have a feasibility issue due to the fact that the fuel element density is lower than the salt density, so the fuel elements float which greatly complicates refueling (for pebbles the floating of the fuel is an advantage). This aspect is here neglected since the only purpose of the present study is to compare the theoretical attainable burnup with the alternative pebble bed design concept.

The core is pseudo-cylindrical (Figure 4.1) with 10 active rings of prismatic fuel blocks making a total of 265 columns of ten levels each (2650 fuel elements). The total core power was set at 2,400 MWth, therefore the power per element at ~ 906 kW. The power density is 10.2 MW/m^3 as in the PB-AHTR. The leakage probability was found from a full core model to be around 3%.

Table 4.3 summarizes the burnup results obtained for selected TRISO packing factors. The maximum attainable burnup—129 GWd/tHM, is obtained for the 15% packing factor design corresponding to a C/HM of 846.

Table 4.3 LS-VHTR attainable burnup for selected TRISO particles packing factors for a three-batch refueling scheme.

Property	TRISO particles packing factor			
	10%	15%	20%	25%
C/HM	1,293	846	623	488
Specific power (W/gHM)	369	246	184	147
Burnup (GWd/tHM)	123	129	126	120
Residence time (EFPD)	333	524	685	816

4.2.2 Gas cooled prismatic fuel (VHTR)

The reference core for the gas cooled prismatic fuel is pseudo-annular (Figure 4.1) with the fuel columns located in rings 6, 7, and 8 for a total of 102 columns, each made of 10 levels for a total of 1,020 fuel blocks. The total core power was assumed to be 600 MW_{th}, consequently the average power generated per fuel element is ~588 kW. The power density is 6.6 MW/m³. The leakage probability was found from a full core model to be 7%.

Table 4.4 summarizes the results obtained for selected TRISO packing factors. The maximum burnup attained is 123 GWd/tHM and requires a packing factor of 11%, corresponding to a C/HM of 1,033.

Table 4.4 VHTR attainable burnup for selected TRISO particles packing factors for three-batch refueling scheme.

Property	TRISO particles packing factor			
	10%	11%	15%	20%
C/HM	1,141	1,033	745	547
Specific power (W/gHM)	239	218	160	120
Burnup (GWd/tHM)	122	123	119	99
Residence time (EFPD)	510	564	744	1,212

4.3 Comparison

Table 4.5 compares the BOL neutronic properties of the four HTRs designs examined, while Figure 4.3 compares the neutrons spectra corresponding to these same designs. The TRISO particles packing factor was adjusted to make C/HM equal 455 in all reactors. The value chosen for C/HM is arbitrary and the comparison is limited to characteristics that are independent from the selected C/HM value. It is noticed that the PB-AHTR features the lowest k_{∞} , the largest η , and the smallest f . The PB-AHTR thermal peak is the largest because the coolant provides extra moderation that increases η . However, the salt absorbs neutrons causing f to drop. The LS-VHTR spectrum shows similar trends, but its coolant volume fraction is below 7% so the neutrons loss in it is smaller—less than 1%.

Table 4.6 summarizes the neutronics properties of the HTR designs that were found to maximize the attainable burnup under this study assumptions. It is found that all HTR designs examined offer a similar burnup. The LS-VHTR burnup is slightly superior since it combines the small leakage probability of the liquid salt systems and the small coolant volume fraction of the prismatic fuel systems. This burnup is only theoretical because to prevent floating of the fuel elements on the salt during refueling it is required to add ballasts to the blocks with a consequent burnup penalty.

The optimal C/HM is lower in the PB-AHTR than in the PBMR due to the flibe contribution to the neutron moderation. This allows an increase of the heavy metal load per pebble by ~ 2.5 times and the energy produced per pebble rises by the same

factor with a direct positive effect on the fuel fabrication cost and spent fuel volume.

Table 4.5 Comparison of HTRs designs BOL properties for C/HM 455.

Property	PB-AHTR	PBMR	LS-VHTR	VHTR
$k_{\infty} (\sigma)$	1.41603 (0.00023)	1.43803 (0.00028)	1.44752 (0.00032)	1.43449 (0.00031)
η	1.57	1.47	1.49	1.47
F	0.90	0.98	0.95	0.96
CR	0.291	0.363	0.338	0.359
Packing factor (%)	10	10.5	26.7	23.6
C/HM	455	455	455	455
Leakage (%)	3	9	3	7
Volume fraction				
TRISO (%)	3.47	3.63	5.98	5.31
Graphite matrix (%)	31.25	31.09	16.47	17.14
Graphite structure (%)	25.28	25.28	69.11	56.93
Coolant (%)	40.00	40.00	6.86	19.05
Fractional absorption				
Fuel kernel (%)	89.59	97.62	95.06	95.85
Coatings (%)	0.60	0.63	0.64	0.64
Graphite matrix (%)	0.83	0.97	0.32	0.37
Graphite structure (%)	0.70	0.79	3.02	3.14
Coolant (%)	8.13	0.00	0.96	0.00

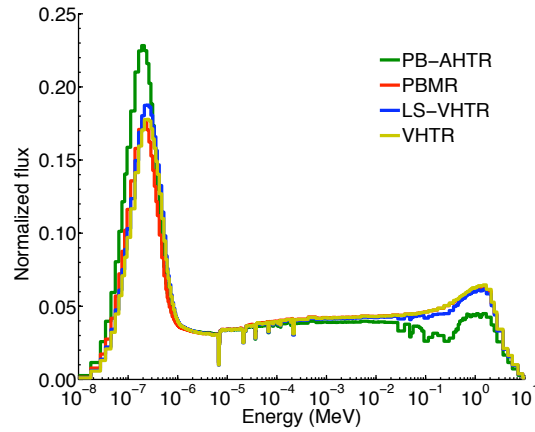


Figure 4.3 Comparison of HTR designs BOL neutron spectra for C/HM 455.

Table 4.6 Comparison of the maximum burnup offered by the HTR design concept examined.

Property	PB-AHTR	PBMR	LS-VHTR	VHTR
Coolant	Flibe	He	Flibe	He
Total power (MW _{th})	2,400	600	2,400	600
Power density (W/cm ³)	10.2	6.6	10.2	6.6
Leakage (%)	3	12	3	7
Packing factor (%)	12.5	5	15	11
C/HM	363	960	846	1,033
HM inventory (kg/MW _{th})	5.23	3.23	4.07	4.59
Burnup (GWd/tHM)	127	126	129	123
Residence time (EFPD)	664	407	524	564

Figure 4.4 compares the spectra of the maximum burnup designs. They are all similar as it should be expected when close to the optimal moderation, except for the PB-AHTR again because of the strong effect of the salt.

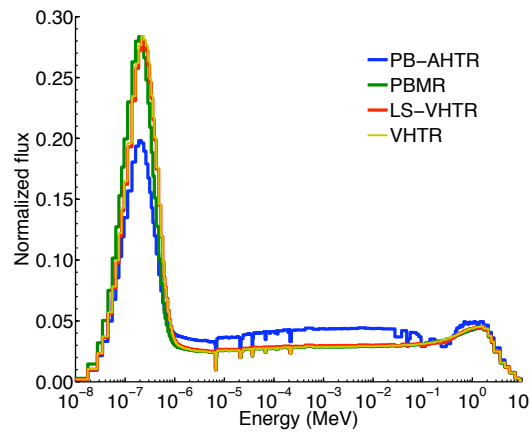


Figure 4.4 Neutrons spectra of the maximum burnup HTR designs.

Current PBMR designs operate with a typical HM load of 9 g per pebble (Matzner and Wallace 2005) corresponding to a TRISO packing factor of $\sim 11.2\%$ (C/HM 425), significantly larger than the packing factor found to allow maximum burnup (5%). This optimized design suffers a large burnup penalty, but reduces the fuel fabrication cost and limits the spent fuel volume (Table 4.7). Compared to the PB-AHTR the optimized PBMR design achieves ~ 20 GWd/tHM lower burnup; the energy generated per pebble is about double that in the PBMR maximum burnup design, but about 30% smaller than for the PB-AHTR pebbles.

Table 4.7 Comparison of PB-AHTR performance with the PBMR maximum burnup and optimized designs.

Property	PB-AHTR	PBMR Maximum burnup	PBMR Optimized
Coolant	Flibe	He	He
Total power (MW _{th})	2,400	600	600
Power density (W/cm ³)	10.2	6.6	6.6
Leakage (%)	3	12	9
Packing factor (%)	12.5	5	11.2
C/HM	363	960	425
HM inventory (kg/MW _{th})	5.23	3.23	7.24
Burnup (GWd/tHM)	127	126	106
Residence time (EFPD)	664	407	734
Initial HM mass (g/pebble)	10.06	4.02	9.01
Energy generated (MWd/pebble)	1.28	0.51	0.96
Relative energy generated per pebble	1.33	0.53	1.00

5. Deep-burn option

HTRs and in particular the Modular Helium-cooled Reactor (MHR) have been proposed to incinerate transuranic elements (TRU) including plutonium, americium, neptunium and possibly curium, deriving from LWRs spent fuel (Rodriguez, et al. 2003). This concept is referred to as deep-burn because fissioning of TRU elements above 60% of the initial load is attained in a single pass of the fuel through the reactor. In this Chapter we investigated the possibility of designing the PB-AHTR for deep-burn purposes and compared its performance to that of the DB-MHR.

The analysis was limited to a predefined set of design parameters. The fuel kernel diameter was fixed at 200 μm for both designs as this is the preferred size to be utilized in the DB-MHR (Venneri 2007). The coatings thicknesses are slightly different from the enriched uranium case, and in particular the buffer layer is thicker in order to accommodate larger kernel deformation and larger gaseous fission products volume resulting from the very high burnup—the carbon buffer thickness is 120 μm ,

inner pyrolytic carbon 35 μm , SiC 35 μm , outer pyrolytic carbon 40 μm . The fuel is $\text{TRUO}_{1.7}$ and the TRU composition, given in Table 5.1, is that obtained from the spent fuel of LWRs after 50 GWd/tHM burnup, 5 years cooling and complete removal of uranium, curium and fission products (Venneri 2007).

The reactor-specific assumptions are defined in the following sections.

Table 5.1 Initial TRU composition from LWR spent fuel after 50 GWd/tHM burnup, 5 years cooling and complete removal of U, Cm and fission products (Venneri 2007).

Nuclide	Weight Fraction (%)
^{237}Np	6.8
^{238}Pu	2.9
^{239}Pu	49.5
^{240}Pu	23.0
^{241}Pu	8.8
^{242}Pu	4.9
^{241}Am	2.8
$^{242\text{m}}\text{Am}$	0.02
^{243}Am	1.4

5.1 Deep-burn PB-AHTR

The depletion analysis for the deep-burn PB-AHTR was performed applying the single pebble in equilibrium bed methodology described in Chapter 2. Total core power (2,400 MWth) and power density (10.2 MW/m³), as well as core components temperatures were assumed the same as for the design fueled with enriched uranium.

The leakage probability was accurately determined using a full core model because the attainable burnup is very sensitive to it. A preliminary value was obtained using an all fresh fuel core, and corrected after an equilibrium core composition was established. It was found that leakage probability has a minimum value for a TRISO particles packing factor of about 10%. For larger packing factors it increases due to spectrum hardening and for lower packing factors it increases due to decrease in the core macroscopic absorption cross section. For the range of packing factors of interest in this study the neutron leakage probability is ~3%.

The attainable burnup and TRU incineration fraction were searched for by varying the graphite-to-heavy metal atom ratio while keeping the fuel kernel diameter constant (Table 5.2). It was found that the maximum burnup (653.5 GWd/tHM) and therefore the maximum HM consumption (66.4%) is achieved with C/HM of ~2,500 but in general burnup and HM incineration are only slightly sensitive to the C/HM ratio. Plutonium inventory is reduced by ~74% and its fissile content becomes smaller as the neutron spectrum gets softer. Long-lived ^{237}Np and its precursors (^{241}Pu , ^{241}Np , ^{245}Cm , ^{249}Bk) are reduced by ~58% and their transmutation is particularly sensitive to C/HM because softer spectra can better fission ^{241}Pu .

Table 5.2 Transmutation properties of the PB-AHTR as a function of TRISO particles packing factor for 200 μm diameter fuel kernels and initial HM load TRU from LWRs spent fuel.

Property	C/HM			
	1684	1993	2439	2746
Packing factor	13%	11%	9%	7%
Initial HM mass (t)	2.75	2.33	1.90	1.69
Neutron flux ($\text{n}/\text{cm}^2\text{-s}$)	$2.97 \cdot 10^{14}$	$3.20 \cdot 10^{14}$	$3.48 \cdot 10^{14}$	$3.99 \cdot 10^{14}$
Burnup (GWd/tHM)	642.3	650.3	653.5	651.7
Residence time (EFPD)	736	631	518	402
HM consumption (%)	65.2	66.1	66.4	66.2
Pu consumption (%)	73.4	74.2	74.2	72.9
Fissile Pu consumption (%)	88.4	90.2	91.2	92.1
^{237}Np and precursors consumption (%)	41.8	51.5	57.6	62.3

Besides the transmutation performance, all the reactivity coefficients of a deep-burn PB-AHTR must be negative for the design to be feasible. The reactivity feedbacks were calculated, using the methodology described in Chapter 3, for the core equilibrium composition that was preliminary obtained from the depletion analysis. Table 5.3 summarizes the results for selected designs. As found for the enriched uranium model cores, all reactivity coefficients are negative for under-moderated designs while over-moderated designs have positive coolant temperature and small void reactivity coefficients.

The maximum burnup design (C/HM $\sim 2,500$) features all negative reactivity coefficients.

Table 5.3 Core average reactivity coefficients in the deep-burn PB-AHTR for selected graphite-to-heavy metal atom ratio.

Reactivity coefficient	C/HM			
	1,684	1,993	2,439	2,746
Fuel temperature (pcm/K)	-1.81	-1.71	-1.51	-1.28
Coolant temperature (pcm/K)	-2.01	-1.56	-0.94	+0.13
Coolant void (pcm/void%)	-55.77	-43.83	-25.83	+3.90
Full coolant void (pcm/void%)	-85.05	-74.09	-54.29	-21.00
Moderator temperature (pcm/K)	-3.94	-4.39	-3.88	-2.93
Moderator and fuel temperature (pcm/K)	-6.11	-5.85	-5.46	-4.31
Moderator and coolant temperature (pcm/K)	-6.18	-6.29	-5.23	-3.33

5.2 TRU transmutation in the DB-MHR

The DB-MHR core is composed of hexagonal prismatic fuel blocks that form a pseudo-annular core as illustrated in Chapter 4. Multiple core configurations have been proposed over the years characterized by different number of rings and different shuffling scheme. For this comparison we selected a five-ring configuration (Figure 5.1) and four-batch fuel management scheme. The methodology applied for determining the attainable burnup is the same as the one described in Chapter 4 for prismatic fuel reactors. The leakage probability was estimated using a full core model; its average value between BOL and EOL was found to be ~5%.

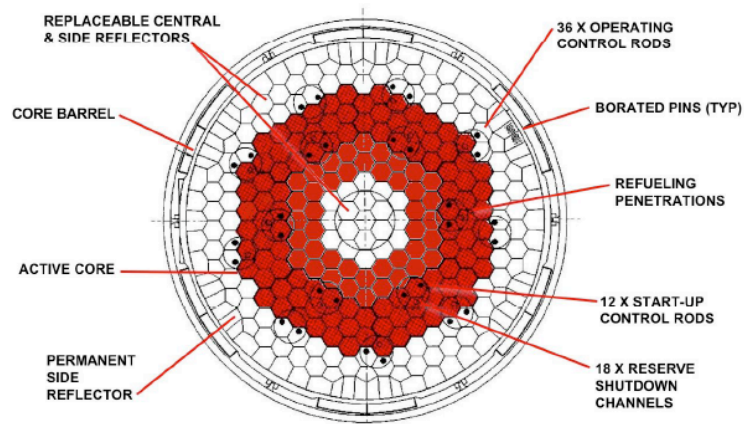


Figure 5.1 DB-MHR core horizontal view with five fuel element rings (Venneri 2007).

The maximum attainable burnup was searched for as a function of C/HM (Table 5.4) and it was found to be achieved with a TRISO particles packing factor of 14% (C/HM ~2,500). As observed for the PB-AHTR, plutonium and HM fractional consumption are not very sensitive to C/HM; fissile plutonium consumption increases with softer spectra; ^{237}Np and precursors consumption is more sensitive to the spectrum and increases for larger C/HM since ^{241}Pu and ^{241}Am fission cross sections increase in soft spectra.

Table 5.4 Transmutation properties of the DB-MHR as a function of TRISO particles packing factor for 200 μm diameter fuel kernels and initial HM load TRU from LWR spent fuel.

Property	C/HM			
	1,970	2,216	2,533	2,955
Packing factor	18%	16%	14%	12%
Initial HM mass (t)	1.31	1.16	1.02	0.87
Burnup (GWd/tHM)	613.7	618.1	621.3	617.4
Residence time (EFPD)	1336	1196	1052	896
HM consumption (%)	62.45	63.01	63.24	62.84
Pu consumption (%)	69.24	69.35	69.49	68.58
Fissile Pu consumption (%)	89.06	90.18	91.16	91.68
²³⁷ Np and precursors consumption (%)	47.74	54.11	58.44	61.28

5.3 Comparison

The PB-AHTR and DB-MHR maximum burnup designs were compared in terms of overall transmutation performance and final waste properties. Table 5.5 shows that burnups are similar for the two systems, only ~ 30 GWd/tHM larger for the PB-AHTR that translates in a $\sim 3\%$ larger heavy metal consumption.

Figure 5.2 shows the spectrum in the sample pebble at BOL and EOL in the PB-AHTR. As argued in Chapter 2, the spectrum in a pebble strongly depends on the average composition of the neighbor pebbles, and the spectral changes between BOL and EOL are limited—for example at BOL the spectrum shows a deep depression around 0.3 eV, corresponding to the lowest energy resonance of ²³⁹Pu that is highly concentrated in fresh pebbles. In the DB-MHR, on the other hand, the spectrum

swings from epithermal at BOL to strongly thermal at EOL (Figure 5.3).

Table 5.5 PB-AHTR and DB-MHR transmutation properties.

Property	PB-AHTR	DB-MHR
Total core power (MW _{th})	2,400	600
Power density (MW/m ³)	10.2	4.68
Initial HM mass (t)	1.90	1.02
C/HM	2,439	2,533
Leakage probability (%)	3	5
Burnup (GWd/tHM)	653.5	621.3
Residence time (EFPD)	518	1052
HM consumption (%)	66.4	63.2
Pu consumption (%)	74.2	69.5
Fissile Pu consumption (%)	91.2	91.2
²³⁷ Np and precursors consumption (%)	57.6	58.4

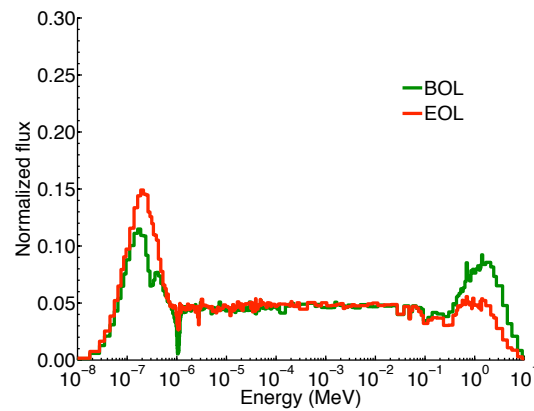


Figure 5.2 PB-AHTR neutrons spectrum at BOL and EOL.

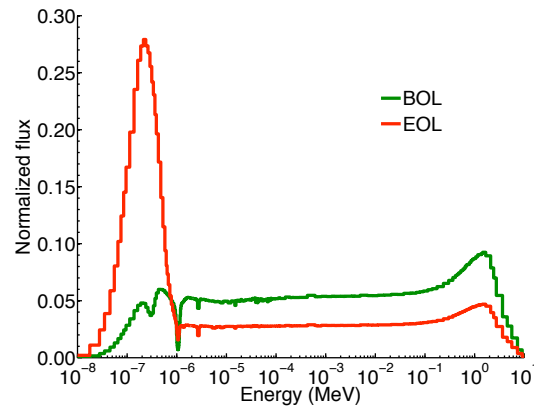


Figure 5.3 DB-MHR neutrons spectrum at BOL and EOL.

The flux changes effect the conversion ratio variations with burnup (Figure 5.4): the DB-MHR fuel cycle starts with a hard spectrum and a larger CR (0.37) that increases moderately as fissile isotopes are consumed and the spectrum softens. The PB-AHTR, instead, starts with a softer spectrum and a smaller CR (0.21) that rapidly increases with burnup because the spectrum only changes slightly.

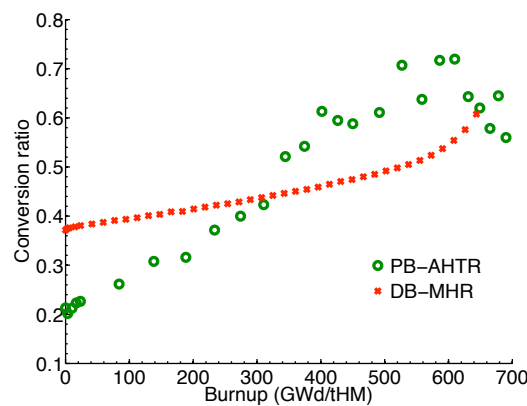


Figure 5.4 Comparison of the conversion ratio as a function of burnup for the PB-AHTR and the DB-MHR.

Table 5.7 compares the consumption of the actinides initially loaded in the reactors and Table 5.6 gives the HM composition at EOL. It is noticed that the PB-AHTR consumption of the short-lived ^{241}Pu is slightly smaller although it operates at more than double the power density of the DB-MHR. The reason for this result must be understood based on the spectrum variations illustrated above. Figure 5.5 shows that the effective fission cross section of ^{241}Pu is almost constant in the PB-AHTR whereas it rapidly increases with burnup in the DB-MHR and towards EOL is about double than in the pebble bed system. The DB-MHR fuel kernels first build up ^{241}Pu because of its high CR and relatively small ^{241}Pu cross sections, but as the spectrum softens ^{241}Pu burns quickly and its concentration at EOL is smaller than in the PB-AHTR fuel.

The reduced ^{241}Pu incineration affects the ^{237}Np inventory consumption.

Table 5.6 Comparison of feed actinides consumption (%) in the PB-AHTR and in the DB-MHR.

Nuclide	PB-AHTR	DB-MHR
^{237}Np	-65.77	-62.85
^{238}Pu	75.63	104.28
^{239}Pu	-98.54	-98.39
^{240}Pu	-90.76	-80.36
^{241}Pu	-49.56	-50.50
^{242}Pu	116.20	136.52
^{241}Am	-94.13	-91.07
$^{242\text{m}}\text{Am}$	-85.47	-75.75
^{243}Am	127.08	88.11

Table 5.7 Comparison of the heavy metal composition at the EOL in the PB-AHTR and in the DB-MHR fuel.

Nuclide	PB-AHTR	DB-MHR
²³⁴ U	0.111%	0.230%
²³⁵ U	0.026%	0.045%
²³⁶ U	0.008%	0.017%
²³⁷ Np	6.917%	6.863%
²³⁸ Np	0.045%	0.053%
²³⁸ Pu	15.137%	16.095%
²³⁹ Pu	2.148%	2.165%
²⁴⁰ Pu	6.319%	12.271%
²⁴¹ Pu	13.191%	11.834%
²⁴² Pu	31.485%	31.486%
²⁴³ Pu	0.014%	0.008%
²⁴⁴ Pu	0.006%	0.003%
²⁴¹ Am	0.488%	0.679%
^{242m} Am	0.009%	0.013%
²⁴² Am	0.004%	0.007%
²⁴³ Am	9.448%	7.155%
²⁴⁴ Am	0.016%	0.009%
²⁴² Cm	1.715%	1.770%
²⁴³ Cm	0.079%	0.055%
²⁴⁴ Cm	11.687%	8.526%
²⁴⁵ Cm	0.957%	0.586%
²⁴⁶ Cm	0.187%	0.130%
²⁴⁷ Cm	0.003%	0.002%

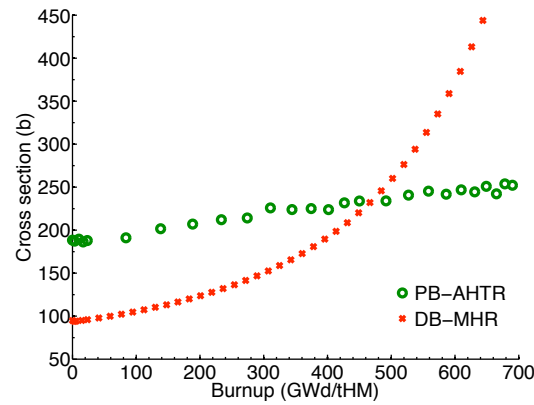


Figure 5.5 Comparison of the ^{241}Pu effective fission cross section as a function of burnup for the PB-AHTR and the DB-MHR.

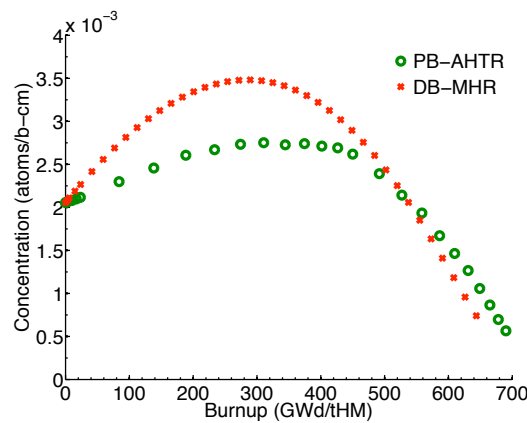


Figure 5.6 Comparison of ^{241}Pu concentration in fuel kernels as a function of burnup in the PB-AHTR and the DB-MHR.

Figure 5.7 and Figure 5.8 compare, respectively, the radiotoxicity and the decay-heat associated with the spent fuel of these deep-burn systems per ton of TRU that is initially loaded in the core. As expected, the PB-AHTR and DB-MHR spent fuel properties are similar. The same figures show also the radiotoxicity and the

decay-heat in 1 ton of TRU from LWRs that is sent directly to the repository. For the first hundred years the fission products decay is dominant and deep-burn systems' spent fuel has larger radiotoxicity and decay-heat; after that the situation is reversed up to 100 thousand years. After about one million years differences become very small. Therefore the main advantages of the deep-burn are the reduction of the ^{237}Np inventory—a major contributor to the long term dose in the vicinity of the repository—and the better resources utilization—about 650 GWd are generated from one ton of otherwise waste.

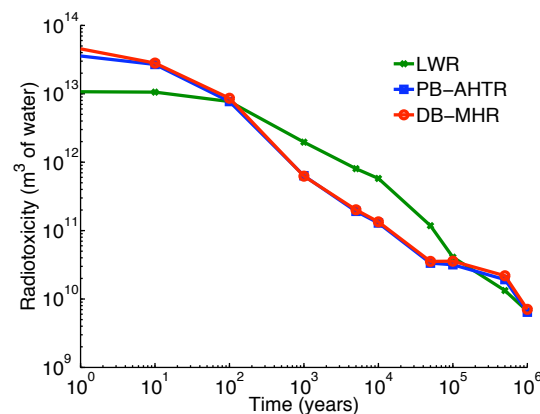


Figure 5.7 Comparison of spent fuel radiotoxicity per metric ton of initial TRU as a function of decay time after discharge.

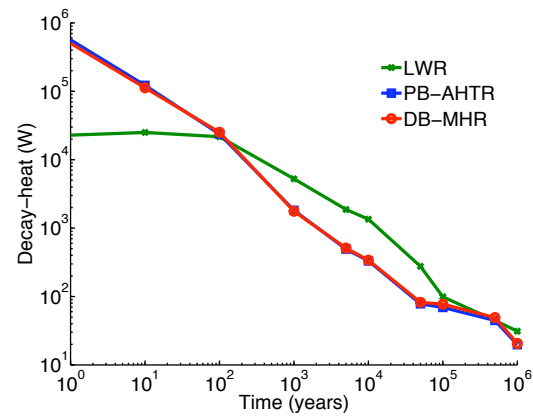


Figure 5.8 Comparison of spent fuel decay-heat per metric ton of initial TRU as a function of decay time after discharge.

6. Modular PB-AHTR

The PB-AHTR project at U.C. Berkeley adopted a modular approach in 2008, in which the core is composed of hexagonal graphite assembly—Pebble Channels Assemblies (PCAs), containing 18 to 19 channels through which pebbles and coolant flow (Bardet, et al. 2008). Among the advantages of using PCAs are: (1) increased HM loading per pebble, because moderation is also provided by the PCA structural graphite, and consequent fuel fabrication and spent fuel volume reduction; (2) reduced coolant volume fraction in the core; (3) multiple channels configuration for multi-zone pebbles recirculation approach; (4) channels for control rods insertion in the central region of the core.

This chapter presents a preliminary study of the MPB-AHTR, including the effects of triple heterogeneity, attainable burnup, and power peaking factors.

6.1 Triple heterogeneity

6.1.1 Steady-state analysis

The Modular PB-AHTR introduces a third level of heterogeneity generated by the confinement of pebbles into physically separated channels; this heterogeneity is superimposed on those introduced by pebbles and by the coated-particles. The effect of this third level of heterogeneity was studied considering a unit cell model, illustrated in Figure 6.1, that consists of a section from the channels region of a PCA (Figure 2.4 and Figure 2.5) to which reflective boundary conditions are applied (infinite array of infinite long PCAs).

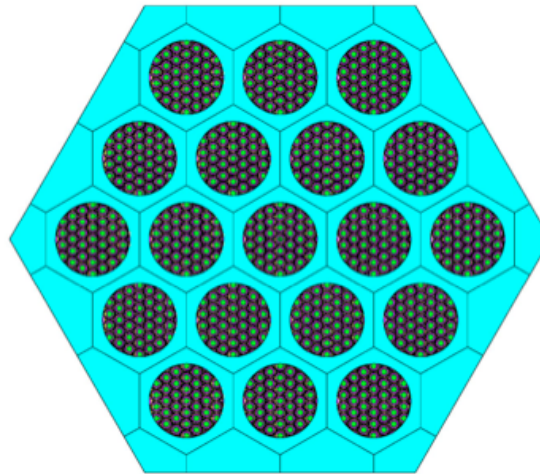


Figure 6.1 Horizontal cross section of a Pebble Channel Assembly (PCA).

The pebbles are annular; the central graphite spherical core is 1.60 cm in diameter and the fuel particles are dispersed in a 0.45 cm thick annular region that is

surrounded by a 0.25 cm thick graphite shell. With these dimensions, the central graphite kernel occupies 15.2% of the volume of the pebble, the annular fuel region occupies 42.7%, and the shell 42.1%. The density of the carbon matrix in which the TRISO particles are dispersed and of the central core is set at 1 kg/m^3 , the kernel diameter is $425 \text{ }\mu\text{m}$ and the packing fraction 35%.

To evaluate the effects of triple heterogeneity, the MPB-AHTR was compared with the integral PB-AHTR single pebble model (6.0 cm diameter pebbles, 60% bed packing factor), with both loaded with clean fuel—10% enriched uranium. The modular design has a lower pebble bed packing factor, 55%, due to the effects of the ordered packing of pebbles against the pebble channel walls. Figure 6.2 illustrates the infinite multiplication factor for the two systems as a function of C/HM. It appears that in the modular design k_∞ is above 1.5 over the entire C/HM range considered, whereas in the integral design it is always below this value. This happens because (1) enhanced parasitic neutron capture in the liquid salt of the integral design in which the flibe volume fraction is nearly double, and (2) enhanced spatial self-shielding of the modular design that increases its η value. Figure 6.3 shows that the neutron absorption by the coolant is larger in the integral design even if compared to the combined absorption of coolant and structure of the modular design. This difference becomes smaller for low C/HM. The integral design was found to reach the maximum attainable burnup with C/HM 350-400. For the modular design, instead, the TRISO particles packing factor limits C/HM; considering a maximum packing factor of 50%,

C/HM must be larger than 400.

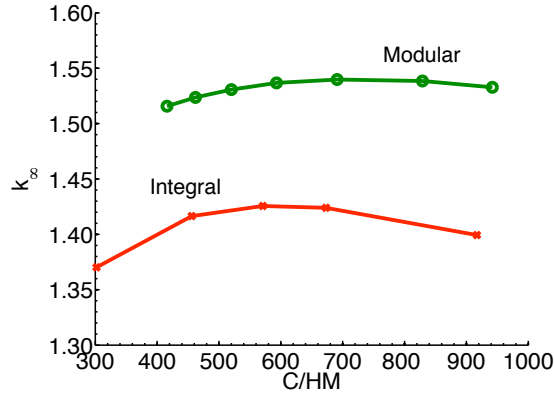


Figure 6.2 BOL infinite multiplication factor as a function of graphite-to-heavy metal atom ratio in a unit cell model of the PB-AHTR modular and integral design.

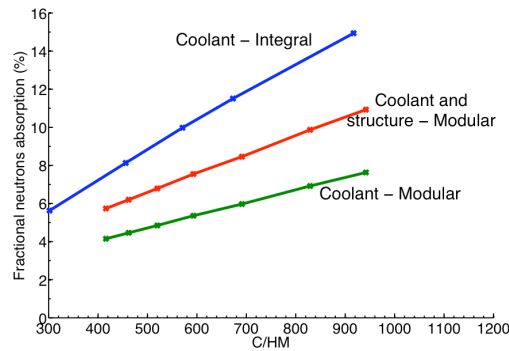


Figure 6.3 Comparison of the fraction of neutrons absorbed by the coolant only, and by the coolant and the PCA structure in the PB-AHTR modular design with the neutrons fraction absorbed by the coolant in the integral design.

For a more balanced comparison, we also analyzed the two designs using the same pebble geometry—3 cm diameter annular pebbles. Table 6.1 and Table 6.2 summarize the neutronic properties and the neutron balance at BOL of the modular PB-AHTR design with 35% TRISO particle packing factor compared to the baseline integral design. Two options were considered for the integral design: Case 1 features

the same C/HM as the modular design—590; Case 2 features C/HM that maximizes the attainable burnup—360. Table 6.2 shows that the coolant absorption is strongly reduced in the MPB-AHTR because the fraction of the core volume that it occupies is half of that in the integral design. The enhanced spatial self-shielding of the modular design increases the resonance escape probability and, hence, enhances η . Reducing the TRISO packing factor has the same effect for the integral design (Case 1), but the fuel amount is small and the salt absorption increases. Data reported in Table 6.1 explain this phenomenon: the modular design and the Case 1 integral design have similar η but f is significantly smaller for the integral design. In Case 2 the large packing factor makes the fuel more competitive against the salt for absorbing neutrons. The salt absorption drops to 8.60% from 13.08% of Case 1 and f is closer to that of the modular design. The drawback is that the spectrum becomes harder and η gets smaller.

Figure 6.4 compares the neutron spectra in the fuel for the three cases. The integral design Case 1 has a larger thermal flux compared to the modular design even though they feature the same C/HM ratio; the larger amount of salt provides extra moderation in the integral case. Case 2 features smaller C/HM than the modular design and its thermal flux is correspondingly lower. The fast flux component of Case 2 is also lower than that of the modular design because of its smaller liquid salt volume fraction. The lower thermal and fast fluxes of the integral design (Case 2) are balanced by a larger epithermal flux component.

Table 6.1 Comparison of selected BOL neutronic properties for the PB-AHTR modular and integral design; the integral design Case 1 features same C/HM as the modular design, while Case 2 features the TRISO packing factor that maximizes attainable burnup.

Parameter	Modular	Integral – Case 1	Integral – Case 2
C/HM	590	590	360
TRISO packing factor	35.0%	8.4%	14.0%
Bed packing factor	55%	60%	60%
HM load (g/pebble)	2.59	0.62	1.04
Leakage (%)	6%	3%	3%
$k_{\infty} (\sigma)$	1.53673 (0.00039)	1.36831 (0.00043)	1.37010 (0.00047)
η	1.67	1.62	1.50
f	0.92	0.85	0.91
^{235}U effective 1-g capture xs (b)	22.8	26.2	21.4
^{238}U effective 1-g capture xs (b)	3.3	4.5	4.7
^{235}U effective 1-g fission xs (b)	114.0	132.5	101.8
^{238}U effective 1-g fission xs (b)	0.03	0.02	0.02
^{235}U capture-to-fission xs ratio	0.200	0.197	0.210
^{238}U capture-to-fission xs ratio	129.82	273.34	234.8

Table 6.2 Comparison of neutron absorption in the core components at BOL for the PB-AHTR modular and integral design; the integral design Case 1 features same C/HM as the modular design, while Case 2 features the packing factor that maximizes attainable burnup.

Parameter	Core region	Modular	Integral Case 1	Integral Case 2
Volume fraction	Fuel	0.47%	0.28%	0.47%
	Coatings and matrix	9.68%	25.34%	25.15%
	Central graphite core	3.61%	9.10%	9.10%
	Shell	10.02%	25.28%	25.28%
	Coolant	19.46%	40.00%	40.00%
	Structure	56.77%	-	-
Neutron absorption	Fuel	91.25%	82.50%	89.50%
	Coatings and matrix	0.79%	2.97%	1.03%
	Central graphite core	0.07%	0.25%	0.15%
	Shell	0.35%	1.20%	0.72%
	Coolant	5.36%	13.08%	8.60%
	Structure	2.19%	-	-

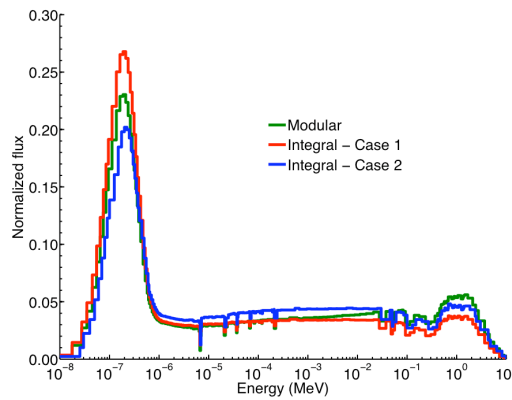


Figure 6.4 Comparison of the neutron spectrum in the fuel of the PB-AHTR modular and integral designs; the integral design Case 1 features the same C/HM as the modular design, while Case 2 features the TRISO packing factor that maximizes attainable burnup.

6.1.2 Spatial self-shielding in the channels

To study the effect of the third level of heterogeneity on the pebbles depletion, a test case featuring 325 μm diameter kernels and 40% packing factor (C/HM 794) was considered. The channels were divided into nine concentric radial zones for which the depletion analysis was performed independently. Table 6.3 gives selected properties as a function of the radial position in the channels. The kernel power and the CR, slightly, peak toward the outer region of the channels as the spatial self-shielding causes a drop of the ^{238}U effective capture cross ($\sim 20\%$). In contrast to what was found for the kernels and pebbles, the ^{235}U cross sections also drop ($\sim 13\%$) towards the center of the channel, not because of self-shielding but because the pebbles close to the channel wall experience a more thermal spectrum (Figure 6.5).

Table 6.3 BOL pebbles properties as a function of the channels radial region.

Property	Zone outer diameter (cm)								
	3.8	5.8	7.8	9.8	11.8	13.8	15.8	17.8	19.8
Local-to-average kernel power ratio	0.91	0.92	0.93	0.94	0.95	0.97	0.99	1.02	1.05
CR	0.151	0.151	0.150	0.149	0.148	0.147	0.146	0.148	0.157
^{235}U fission cross section (b)	86.5	87.2	87.8	88.8	90.1	91.4	93.6	95.8	98.4
^{235}U capture cross section (b)	18.3	18.4	18.5	18.7	18.9	19.2	19.6	20.0	20.5
^{238}U capture cross section (b)	3.9	4.0	4.0	4.0	4.0	4.1	4.1	4.3	4.7

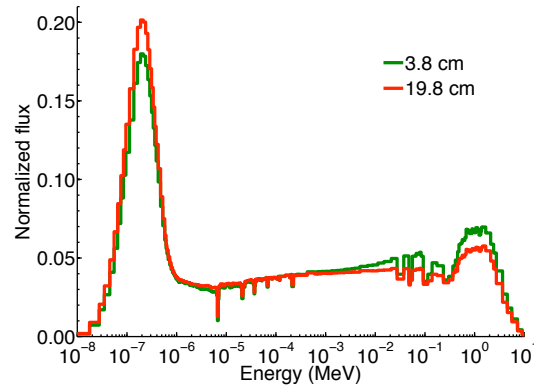


Figure 6.5 Comparison of the BOL neutron spectrum in the center and in the outermost region of the channel.

The power peaking becomes smaller with burnup (Figure 6.6) because the outer region burns faster and the CR across the channel is relatively flat. After about 140 EFPD the power starts peaking at the center of the channels.

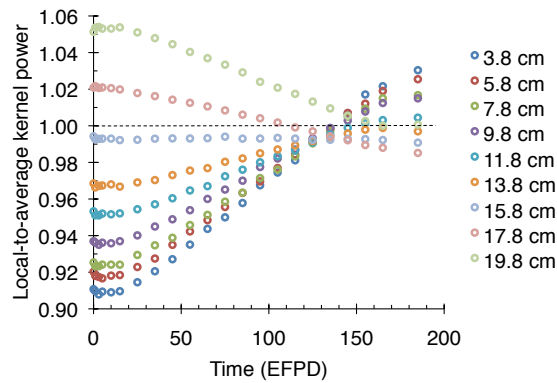


Figure 6.6 Local kernel power-to-average kernel power ratio as a function of channel radial region and residence time.

6.2 Attainable burnup and power peaking factor

The MPB-AHTR attainable burnup was determined as a function of TRISO packing factor for 19.9% enriched uranium fuel and 30 MW/m³ power density. This value, about three times larger than the power density adopted for the integral design, was found to guarantee adequate response during transients (Griveau, et al. 2007). The methodology described in Chapter 2 was applied for this analysis dividing the core into 16 radial and 12 axial regions in order to estimate the power peaking factors.

Table 6.4 gives the results obtained for 325 µm diameter fuel kernels. Increasing the TRISO packing factor up to 50% not only increases attainable burnup, but also reduces the power load per kernel. Currently design practice for TRISO fuels limits peak kernel powers to 400 mW (Sterbentz, et al. 2004) and all designs in Table 6.4 moderately exceed this limit. In addition, the loading of more TRISO particles increases the pebble's average density above the buoyancy limit value of 1.65 kg/m³—assuming a graphite lower density limit of 1 kg/m³.

An ongoing study is evaluating the feasibility of increasing the peak kernel power limit for the MPB-AHTR, because the fuel in this reactor operates at peak temperatures approximately 300°C below the peak temperatures that occur in MHRs.

Table 6.4 MPB-AHTR properties for selected TRISO particle packing factor—325 μm kernel diameter, 19.9% enrichment, 30 MW/m^3 .

Property	TRISO particles packing factor		
	40%	45%	50%
C/HM	794	707	637
Burnup (GWd/tHM)	215	217	219
Residence time (EFPD)	256	269	301
HM load (g/pebble)	1.94	2.18	2.43
Average pebble density (kg/m^3)	1.594	1.630	1.665
TRISO particles per pebble	$1.16 \cdot 10^4$	$1.31 \cdot 10^4$	$1.45 \cdot 10^4$
Average kernel power (mW)	154	137	123
Peak kernel power (mW)	554	488	438
Kernel power peaking factor	3.60	3.56	3.56

The kernel size can be reduced in order to increase the number of particles per pebble and thus reduce the peak power per kernel (Table 6.5). This approach is effective for reducing the peak power, but it significantly penalizes the attainable burnup. Furthermore, the C/HM for a given TRISO packing factor becomes very large and this may make the coolant and void reactivity coefficients unacceptable. The reactivity coefficients for these designs need yet to be evaluated.

The preliminary results presented above suggest that the power density at which the MPB-AHTR can operate must be below the target value of 30 MW/m^3 .

Table 6.5 MPB-AHTR properties for selected TRISO particles packing factor—225 μm kernel diameter, 19.9% enrichment, 30 MW/m³.

Property	TRISO particles packing factor		
	40%	45%	50%
C/HM	1,546	1,376	1,241
Burnup (GWd/tHM)	182	190	196
Residence time (EFPD)	104	120	140
HM load (g/pebble)	1.00	1.12	1.25
Average pebble density (kg/m ³)	1.540	1.569	1.598
TRISO particles per pebble	$1.80 \cdot 10^4$	$2.03 \cdot 10^4$	$2.25 \cdot 10^4$
Average kernel power (mW)	99	88	79
Peak kernel power (mW)	304	284	267
Kernel power peaking factor	3.07	3.23	3.38

7. Conclusions

This project investigated the neutronic characteristics of the Pebble Bed Advanced High Temperature Reactor, a novel concept that combines liquid salt (flibe) cooling and TRISO coated-particles fuel technology. Both a large, “integral” core design, and a smaller, high-power density “modular” core design were studied. In contrast to modular helium reactors (MHRs), liquid salt cooled HTRs provide improved passive decay-heat removal capability across a wide range of power levels and can operate at four to six times higher power density and at atmospheric pressure. However, from the neutronics point of view flibe is not transparent to neutrons like helium. Flibe acts as both a neutron moderator and an absorber—even when highly enriched lithium (only 4 ppm ^6Li) is used. In the integral pebble bed reactor designs the coolant occupies 40% of the core volume and 20% in the modular design. For the PB-AHTR this translates into ~8% neutrons lost in flibe in the integral design, and ~4% in the modular design. Therefore the main feasibility issue of this novel reactor concept is the ability to compensate for the positive reactivity feedback associated

with the reduced parasitic neutron absorption due the coolant temperature rise by the spectrum hardening effect that also results from the coolant temperature increase. In addition the neutron capture in the coolant imposes a burnup penalty that needs to be estimated.

To address these issues we had to determine the pebbles' time dependent composition and the core equilibrium fuel composition. The computational tools available were either obsolete or not capable to correctly model all the physical phenomena—double or triple heterogeneity effects, use of salt instead helium, problem dependent cross sections. To overcome these limitations we have chosen a universal and flexible tool—MCNP, for steady-state neutronic analysis and coupled with ORIGEN2.2 time-dependent code for depletion analysis. Two new methodologies were developed for implementation with the MCNP-ORIGEN code system in order to compute the pebble time dependent and the core equilibrium composition. (1) A simplified single pebble methodology for scoping analysis, that is capable to span a large range of design variables combinations in a relatively short time. (2) A full 3D core methodology for refined analyses accounting for more details such as reflectors, axial and radial burnup distribution, pebbles recirculation schemes, and power peaking factors.

A parametric analysis performed for the integral PB-AHTR design covered a wide range of fuel kernel diameters and graphite-to-heavy metal atom ratios (C/HM), determining attainable burnup and reactivity coefficients. It was found that with 10%

enriched uranium fuel: (1) burnup can reach ~ 130 GWd/tHM; (2) the maximum burnup is attained with C/HM values in the 300-400 range that defines the optimal moderation region; (3) spatial self-shielding enables larger kernels to reach slightly larger burnup.

Multiple reactivity feedback mechanisms were investigated: coolant temperature, coolant small and full voiding, fuel temperature, and moderator temperature. Particular attention was devoted to the analysis of the coolant temperature coefficient and to the multiple physical phenomena that are associated with it. When flibe's temperature rises, its density decreases and therefore the system loses a neutron absorber and a moderator. Less absorption means a positive reactivity change; less moderation means a neutron spectrum hardening that results in a negative reactivity change if the system is under-moderated, but a positive reactivity effect if over-moderated. For the integral PB-AHTR design the boundary between under-moderated and over-moderated designs occurs in the 300-400 C/HM range, depending on the fuel kernel diameter. The same C/HM values also offer the maximum burnup—as should be expected, from the optimally moderated designs. The coolant temperature increase also causes a hardening of the thermal neutron spectrum and the consequent reactivity change depends on the fuel composition—mainly on the fissile plutonium concentration—and is mostly negative. The small coolant void reactivity response resembles the temperature effect, except for the shift of the thermal flux to higher energies. For the void reactivity coefficient to be negative the C/HM must be below the optimal

moderation range.

Once the neutronic feasibility of the PB-AHTR was established, its performance was compared to that of alternative options for HTRs, including the helium-cooled pebble bed reactor and prismatic fuel reactors, both gas-cooled and liquid salt-cooled. It was found that neutrons absorbed in the coolant do not penalize the attainable burnup in the PB-AHTR as compared to the other designs. Compared with the gas-cooled pebble bed design that offers the maximum burnup (5% TRISO packing factor), it was found that for the integral design the contribution to moderation of the flibe enables to load ~2.5 times more fuel per pebble, meaning ~2.5 more energy generated per pebble, less pebbles to fabricate and smaller spent fuel volume to handle.

Optimized PBMR designs feature an HM loading of 9 g per pebble (11.2% TRISO packing factor) that penalizes the attainable burnup, but also reduces the fuel fabrication cost and the spent fuel volume. Comparing the PB-AHTR with this optimized PBMR design it was found that the spent fuel generated by the integral PB-AHTR design is almost halved (Table 7.1).

Comparing the PB-AHTR to LWRs (Table 7.1) it was found that the PB-AHTR requires about 30% less natural uranium and about 20% less SWU (Separative Work Units) per unit of electric energy generated, whereas the optimized PBMR requires the same separative work and uses only 10% less natural uranium than typical LWRs.

Table 7.1 Performance comparison of the integral PB-AHTR design with the LWR and the optimized PBMR.

Property	LWR	PB-AHTR	PBMR ^a
Burnup (GWd/tHM)	55	117 ^b	80
Enrichment (%)	5.0	10.0	8.1
C/HM	-	363	425
HM load per pebble (g)	-	10.06	9.00
Thermal efficiency (%)	33	46	42
Natural uranium consumption ^c (kg/MWe-day)	0.630	0.439	0.565
Separative work consumption (SWU/MWe-day)	0.397	0.321	0.399
Depleted uranium generation (kg/MWe-day)	0.575	0.421	0.535
Relative natural uranium consumption	1.00	0.70	0.90
Relative SWU consumption	1.00	0.81	1.00
Relative spent fuel volume	-	0.56	1.00

^a (Matzner and Wallace 2005); ^b Accounting for 2% excess reactivity necessary to compensate for the xenon transient after an abrupt power reduction from 100% to 40%; ^c Tails assay 0.3%.

The PB-AHTR can also be designed to operate as a TRU incinerator, as proposed for helium cooled “deep-burn” reactors. It was found that in a single pass through the core ~66% of the TRU from LWR spent fuel can be fissioned and this burnup is slightly better (3%) as compared to that obtained using helium-cooled systems.

A preliminary analysis of a modular design option for the PB-AHTR was also undertaken. In this variant the core consists of hexagonal graphite blocks with multiple channels for pebbles and coolant flow. The coolant volume fraction is reduced to about half as compared to the integral design and smaller annular pebbles are used to operate at higher power density. The MPB-AHTR introduces a third level of heterogeneity—coated-particles, pebbles, channels—that enhances spatial

self-shielding. The power density at which the MPB-AHTR can operate is limited by the power that coated-particles can withstand; the current limit is set at ~ 400 mW. Multiple power peaking factors make the maximum power that a TRISO particle experiences as high as ~ 3.5 times the core average fuel kernel power. Because the number of fuel particles that can be loaded per pebble is limited by the maximum packing factor or possibly by the density limit on the pebble, the MPB-AHTR will need to operate at a power density below 30 MW/m^3 .

Follow-on studies of the PB-AHTR will have to include multiple aspects. The attainable burnup and reactivity coefficients analysis need to be calculated on a full core scale in order to evaluate the importance of all design details, including effect of the reflector, axial burnup distribution, and detailed temperature distribution. The pebbles recirculation scheme needs to be optimized; among the options to be considered is full mixing versus recirculation of relatively high burnup pebbles in the central part of the core. The pebbles out-of-core residence time needs to be accounted for as well. The control and shutdown system likewise needs to be designed in detail—a preliminary analysis not presented here verified its potential effectiveness.

References

- Albornoz, Felipe, and Sergio Korochinsky. "MCNP Modelling of the PBMR Equilibrium Core." *PHYSOR 2006*. Vancouver, BC, Canada, 2006.
- Bardet, P., et al. "The Pebble Recirculation Experiment (PREX) for the AHTR." *GLOBAL 2007*. Boise, Idaho, USA, 2007.
- Bardet, P., J. T. Franklin, K. Lee, M. Toulouse, and P. F. Peterson. "The Pebble Recirculation Experiment (PREX) for the AHTR." *GLOBAL 2007*. Boise, Idaho, USA, 2007.
- Bardet, Philippe, Edward Blandford, Massimiliano Fratoni, Aurelie Niquille, Ehud Greenspan, and Peterson F. Per. "Design, Analysis and Development of the Modular PB-AHTR." *ICAPP '08*. Anaheim, CA USA, 2008.
- Brown, Forrest B., W. R. Martin, W. Ji, J. L. Conlin, and J. C. Lee. "Stochastic geometry and HTGR modeling for MCNP5." *ANS Monte Carlo 2005 Topical Meeting*. Chattanooga, TN, USA, 2005.
- Clarno, Kevin T., and Jess C. Gehin. "Physics Analysis of the LS-VHTR: Salt Coolant and Fuel Block Design." *PHYSOR '06*. Vancouver, BC, Canada, 2006.
- Cogliati, Joshua J., and Abderrafi M. Ougouag. "Pebbles: A computer code for modeling packing, flow, and recirculation of pebbles in a Pebble Bed Reactor." *HTR2006*. Johannesburg, South Africa, 2006.
- Croff, Allen G. "ORIGEN2: A Versatile Computer Code for Calculating the Nuclide Compositions and Characteristics of Nuclear Materials." *Nuclear Technology* 62 (1983): 335-352.
- de Zwaan, S. J. "The Liquid Salt Temperature Pebble Bed Reactor." M.Sc. Thesis, Delft University of Technology, The Netherlands, 2005.
- Forsberg, C. W., P. F. Peterson, and P. S. Pickard. "Molten-Salt-Cooled Advanced High-Temperature Reactor for Production of Hydrogen and Electricity." *Nuclear Technology* 144 (2003): 289-302.
- Forsberg, Charles W., Per F. Peterson, and R. A. Kochendarfer. "Design Options for the Advanced High-Temperature Reactor." *ICAPP '08*. Anaheim, CA USA, 2008.
- Fratoni, Massimiliano, and Ehud Greenspan. "Determination of the equilibrium composition of cores with continuous fuel feed and removal using MOCUP." *Joint International Topical Meeting on Mathematics & Computation and Supercomputing in Nuclear Applications*. Monterey, CA USA, 2007.
- Goluoglu, S., N. F. Landers, L. M. Petrie, and D. F. Hollenbach. "CSAS: Control

- Module for Enhanced Criticality Safety Sequences." ORNL/TM-2005/39, Oak Ridge National Laboratory, 2006.
- Gougar, Hans D. "The Application of the PEBBED Code Suite to the PBMR-400 Coupled Code Benchmark." INL/EXT-06-11842, Idaho National Laboratory, Idaho Falls, Idaho, 2006.
- Griveau, A., F. Fardin, H. Zhao, and P. F. Peterson. "Transient Thermal Response of the PB-AHTR to Loss of Forced Cooling." *GLOBAL 2007*. Boise, Idaho, USA, 2007.
- Izenon, Michael G. "Effects of Fuel Particle and Reactor Core Design." PhD Thesis, Massachusetts Institute of Technology, 1987.
- Izenon, Micheal G. "Effect of fuel particle and reactor core design on Modular HTGR source terms." PhD Thesis, Nuclear Engineering Department, Massachusetts Institute of Technology, 1987.
- Kadak, A., and D. A. Petti. "Modular Pebble Bed Reactor Project University Research Consortium Annual Report." INEEL and MIT, USA, 2000.
- Kim, T. K., T. A. Taiwo, and W. S. Yang. "Preliminary Neutronic Studies for the Liquid-Salt-Cooled Very High Temperature Reactor (LS-VHTR)." Argonne National Laboratory, USA, 2005.
- Kovacs, W. J., K. Bongartz, and D. Goodin. "TRISO-Coated HTGR Fuel Pressure-Vessel Performance Models." GA-A16807, 1983.
- Massimo, Luigi. *Physics of High-Temperature Reactors*. Pergamon Press, 1976.
- Matzner, Dieter, and Edward Wallace. "PBMR moves forward, with higher power and horizontal turbine." *Modern Power Systems*, February 2005: 11-15.
- Milosevic, M., E. Greenspan, and J. Vujic. "New Monte Carlo Procedures and Cross-Section Libraries for Fuel Burnup in Innovative Reactor Designs." *Joint International Topical Meeting on Mathematics & Computation and Supercomputing in Nuclear Applications*. Avignon, France, 2005.
- Moore, R. L., B. G. Schnitzler, C. A. Wemple, R. S. Babcock, and D. E. Wessel. "MOCUP: MCNP-ORIGEN2 Coupled Utility Program." Idaho National Engineering Laboratory, USA, 1995.
- Pohl, Peter. "The Importance of the AVR Pebble-Bed Reactor for the Future of Nuclear Power." *PHYSOR-2006*. Vancouver, BC, Canada, 2006.
- Rodriguez, C., A. Baxter, D. McEachern, M. Fikani, and F. Venneri. "Deep-Burn: making nuclear waste transmutation practical." *Nuclear Engineering and Design*, no. 222 (2003): 299-317.
- Sterbentz, James W., Bren Phillips, Robert L. Sant, Gray S. Chang, and Paul D. Bayless. "Reactor Physics Parametric and Depletion Studies in Support of TRISO Particle Fuel Specification for the Next Generation Nuclear Plant."

INEEL/EXT-04-02331, Idaho National Laboratory, 2004.

Terry, William K. "Modular Pebble-Bed Reactor Project." INEEL/EXT-01-01623, Idaho Falls, Idaho, 2001.

Teuchert, E., U. Hansen, and K. A. Haas. "V.S.O.P.-Computer Code System for Reactor Physics and Fuel Cycle Simulation." KFA-IRE, 1980.

Venneri, Francesco. "MHR core block design PUMA core specification." General Atomics, 2007.

X-5 Monte Carlo Team. "MCNP - A General Monte Carlo N-Particle Transport Code, Version 5." Los Alamos National Laboratory, 2003.

Appendix A. MOCUP

MOCUP (Moore, et al. 1995)—MCNP-ORIGEN Coupled Utility Program—is a set of scripts that couples MCNP (X-5 Monte Carlo Team 2003) and ORIGEN2 (Croff 1983) to solve time dependent depletion problems. MCNP provides flux and reaction rates for each of the nuclides to be depleted inside each zone of interested (limited to 50). These are utilized to calculate effective one-group cross sections to input in ORIGEN2 together with the initial fuel composition. ORIGEN2 performs the depletion analysis according to the time and power or flux provided in the input and output the depleted materials composition at the end of the time step. These updated compositions are transferred back to MCNP to determine a new set of cross sections. The process is iterated for as many time steps as required by the user.

MOCUP performs its function through three utilities (Figure A.1): `mcnpPRO`, `origenPRO`, `compPRO`. The first utility in the sequence, `mcnpPRO`, reads MCNP input, output, and metal (a summary file that contains tallies values); from the input it takes the concentration of each nuclide to be tracked (it must be in atoms/b-cm) and

the tally identification numbers where to read flux and reaction rates; from the output it takes the volumes; from the metal takes fluxes and reaction rates. The tallies that provide these quantities require a mandatory formatting for the program to recognize them.

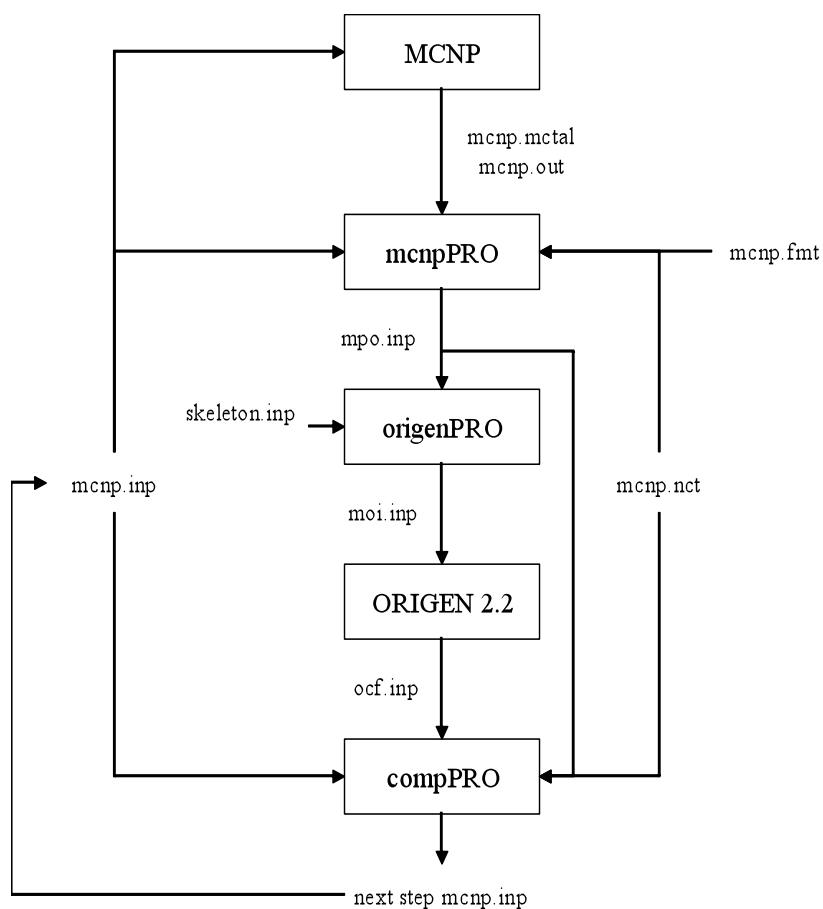


Figure A.1 MOCUP flow chart.

The `mcnpPRO` utility calculates the effective one-group cross sections and stores them into files named `mpo.time_step.delpetion_zone` where `time_step` is a number that

indicates the depletion step and *depletion_zone* is a letter that indicates to which depletion zone it pertains. These files beside cross sections contain a set of information on the zone (volume, total density, flux).

Once mcnpPRO is completed, the mpo files content is passed to the next utility, origenPRO, which uses all those data to fill an incomplete ORIGEN2 input. This file is called skeleton and needs to be compiled by the user with the information for the depletion, in particular what type of computation will be performed—constant flux or constant power—for how long and at what power or flux. The ORIGEN2 package contains default cross sections library that can be utilized, but also gives the option to the user to input customized cross section either creating a full new library (~1600 nuclides) or choosing one of the default library and replacing only selected cross sections. MOCUP takes advantage of the last option and the origenPRO utility completes the skeleton file with the cross section calculated from the MCNP data, to make an ORIGEN2 input. In the same skeleton file, the user has to input the default library that will be applied for all nuclides and all reactions for which customized cross sections are not provided. Once this reading/writing process is complete, origenPRO terminates launching ORIGEN2.

The last utility in the sequence, compPRO, reads the compositions of the depleted materials stored in files called *ocf.depletion_zone.time_step* where *depletion_zone* is a number identifying the depletion zone and *time_step* is the depletion step number. A new MCNP input is created from the initial one updating the compositions of the

depleted zones.

The process, repeated for each time step, is always the same, except at the first step. When the depletion starts ORIGEN2 reads the materials compositions from the MCNP input, but this contains a limited set of nuclides (~100) compared to those that are generated in the depletion process. The set of nuclides tracked in MCNP is selected to accurately determine the system multiplication factor and those nuclides that are not tracked are considered not influential to that purpose, but at every step their composition would be reset. To avoid this, ORIGEN2 starting from the second step reads the input compositions from the ocf files described above. The same files are the source of compositions for the MCNP input, but while MCNP takes only selected nuclides, ORIGEN2 takes all of them.

The MOCUP version in use at UC Berkeley includes a number of improvements added to the original version. In particular an extra script is used to modify the ^{241}Am (n, γ) branching ratio to ^{242}Am and $^{242\text{m}}\text{Am}$ according to the user need (Milosevic, Greenspan and Vujic 2005) and another script determine the power distributions among the depletion zones using MCNP fission rate tallies (Fratoni and Greenspan 2007).

Appendix B. Sample inputs

Single pebble with reflective boundary conditions.

```

PB-AHTR single pebble
c
c ccccccccccccccccccccccccccccccccccccccccccccccccccccccccc
c
c      Description: PB-AHTR
c      Fuel Uranium Oxy-Carbide
c      Coolant Flibe (0.0004% Li-6)
c      TRISO Packing Factor 12.5%
c      Initial Enrichment 10%
c      Graphite Matrix Density 1.60 g/cc
c      Fuel kernel diameter 425 microm
c      Tallies:      for MOCUP
c      Author:      Massimiliano Fratoni
c      Date:        00/00/0000
c
c ccccccccccccccccccccccccccccccccccccccccccccccccccccccccc
c
c      Pebbles Lattice
31  0      -31 32 -33 34 -35 36 -37 38
           fill=6
                                     imp:n=1
c
c      Pebble
c      Active volume
21  0      -21
           fill=7
                                     u=-6
                                     imp:n=1
c      Shell
22 22 -1.74      -22 21
                                     u=-6 tmp=8.29946E-08 imp:n=1
c      Coolant
23 23 8.34284E-02      22
                                     u=6 tmp=7.99787E-08 imp:n=1
c      TRISO particles lattice - Simple Cubic
11  0      -11 12 -13 14 -15 16
           lat=1      fill=8
                                     u=7
                                     imp:n=1

```

```

c
c  TRISO particles
c  Fuel kernel
100 1  7.084586E-02  -1          u=8  tmp=9.24733E-08  imp:n=1
c  Matrix and coatings mix
2   2  8.017935E-02   1          u=8  tmp=8.81648E-08  imp:n=1
c
99  0          31:-32:33:-34:35:-36:37:-38          imp:n=0
c

c *****
c
c  SURFACES
c
c  Fuel: TRISO Layers
1   so  2.125E-02  $  Kernel radius
c
c  Fuel Particles Lattice
11  px  6.73007E-02
12  px -6.73007E-02
13  py  6.73007E-02
14  py -6.73007E-02
15  pz  6.73007E-02
16  pz -6.73007E-02
c
c  Pebble
21  so  2.5  $ Inner radius
22  so  3.0  $ Outer radius
c
c  Pebbles Lattice
*31 px  3.007647
*32 px -3.007647
*33 p   1.  1.732050808  0.  6.015294
*34 p   1.  1.732050808  0. -6.015294
*35 p  -1.  1.732050808  0.  6.015294
*36 p  -1.  1.732050808  0. -6.015294
*37 pz  3.007647
*38 pz -3.007647
c

c *****
c
c  MATERIALS
c
c  Fuel Mix (800 C - Scattering Kernel at 727 C)
m1  6000.16c 1.180764E-02
    8016.16c 3.542293E-02
    92234.92c 1.000000E-24
    92235.94c 2.361529E-03
    92236.92c 1.000000E-24
    92237.92c 1.000000E-24
    92238.94c 2.125376E-02
    92239.42c 1.000000E-24
    93236.63c 1.000000E-24

```

93237.63c	1.000000E-24
93238.63c	1.000000E-24
93239.63c	1.000000E-24
94236.92c	1.000000E-24
94237.92c	1.000000E-24
94238.92c	1.000000E-24
94239.94c	1.000000E-24
94240.94c	1.000000E-24
94241.94c	1.000000E-24
94242.94c	1.000000E-24
94243.92c	1.000000E-24
94244.92c	1.000000E-24
95241.63c	1.000000E-24
95601.63c	1.000000E-24
95242.63c	1.000000E-24
95243.88c	1.000000E-24
95244.63c	1.000000E-24
96242.63c	1.000000E-24
96243.63c	1.000000E-24
96244.63c	1.000000E-24
96245.63c	1.000000E-24
96246.63c	1.000000E-24
96247.63c	1.000000E-24
96248.63c	1.000000E-24
97249.63c	1.000000E-24
98249.63c	1.000000E-24
98250.63c	1.000000E-24
35081.63c	1.000000E-24
36083.63c	1.000000E-24
36084.63c	1.000000E-24
37085.63c	1.000000E-24
37087.63c	1.000000E-24
39089.63c	1.000000E-24
40091.92c	1.000000E-24
40092.92c	1.000000E-24
40093.92c	1.000000E-24
40094.92c	1.000000E-24
40095.92c	1.000000E-24
40096.92c	1.000000E-24
42095.63c	1.000000E-24
42097.63c	1.000000E-24
42098.63c	1.000000E-24
42100.63c	1.000000E-24
43099.63c	1.000000E-24
44101.63c	1.000000E-24
44102.63c	1.000000E-24
44103.63c	1.000000E-24
44104.63c	1.000000E-24
45103.92c	1.000000E-24
45105.92c	1.000000E-24
46104.63c	1.000000E-24
46105.63c	1.000000E-24
46108.63c	1.000000E-24
47109.92c	1.000000E-24

```

48110.63c 1.000000E-24
48113.92c 1.000000E-24
48114.92c 1.000000E-24
49115.63c 1.000000E-24
53127.92c 1.000000E-24
53129.92c 1.000000E-24
54131.92c 1.000000E-24
54132.92c 1.000000E-24
54134.92c 1.000000E-24
54135.92c 1.000000E-24
55133.92c 1.000000E-24
55134.92c 1.000000E-24
55135.92c 1.000000E-24
55137.92c 1.000000E-24
57139.63c 1.000000E-24
59141.63c 1.000000E-24
60143.63c 1.000000E-24
60144.63c 1.000000E-24
60145.63c 1.000000E-24
60146.63c 1.000000E-24
60147.63c 1.000000E-24
60148.63c 1.000000E-24
60150.63c 1.000000E-24
61147.63c 1.000000E-24
61148.63c 1.000000E-24
61149.63c 1.000000E-24
62147.63c 1.000000E-24
62149.63c 1.000000E-24
62150.63c 1.000000E-24
62151.63c 1.000000E-24
62152.63c 1.000000E-24
63153.63c 1.000000E-24
63154.63c 1.000000E-24
63155.63c 1.000000E-24
64155.92c 1.000000E-24
64156.92c 1.000000E-24
64157.92c 1.000000E-24

```

```

c
c   Single isotopes for depletion
m101 92234.92c 1.
m102 92235.94c 1.
m103 92236.92c 1.
m104 92237.92c 1.
m105 92238.94c 1.
m106 92239.42c 1.
m107 93236.63c 1.
m108 93237.63c 1.
m109 93238.63c 1.
m110 93239.63c 1.
m111 94236.92c 1.
m112 94237.92c 1.
m113 94238.92c 1.
m114 94239.94c 1.
m115 94240.94c 1.

```

m116	94241.94c	1.
m117	94242.94c	1.
m118	94243.92c	1.
m119	94244.92c	1.
m120	95241.63c	1.
m121	95601.63c	1.
m122	95242.63c	1.
m123	95243.88c	1.
m124	95244.63c	1.
m125	96242.63c	1.
m126	96243.63c	1.
m127	96244.63c	1.
m128	96245.63c	1.
m129	96246.63c	1.
m130	96247.63c	1.
m131	96248.63c	1.
m132	97249.63c	1.
m133	98249.63c	1.
m134	98250.63c	1.
m201	35081.63c	1.
m202	36083.63c	1.
m203	36084.63c	1.
m204	37085.63c	1.
m205	37087.63c	1.
m206	39089.63c	1.
m207	40091.92c	1.
m208	40092.92c	1.
m209	40093.92c	1.
m210	40094.92c	1.
m211	40095.92c	1.
m212	40096.92c	1.
m213	42095.63c	1.
m214	42097.63c	1.
m215	42098.63c	1.
m216	42100.63c	1.
m217	43099.63c	1.
m218	44101.63c	1.
m219	44102.63c	1.
m220	44103.63c	1.
m221	44104.63c	1.
m222	45103.92c	1.
m223	45105.92c	1.
m224	46104.63c	1.
m225	46105.63c	1.
m226	46108.63c	1.
m227	47109.92c	1.
m228	48110.63c	1.
m229	48113.92c	1.
m230	48114.92c	1.
m231	49115.63c	1.
m232	53127.92c	1.
m233	53129.92c	1.
m234	54131.92c	1.
m235	54132.92c	1.

```

m236  54134.92c  1.
m237  54135.92c  1.
m238  55133.92c  1.
m239  55134.92c  1.
m240  55135.92c  1.
m241  55137.92c  1.
m242  57139.63c  1.
m243  59141.63c  1.
m244  60143.63c  1.
m245  60144.63c  1.
m246  60145.63c  1.
m247  60146.63c  1.
m248  60147.63c  1.
m249  60148.63c  1.
m250  60150.63c  1.
m251  61147.63c  1.
m252  61148.63c  1.
m253  61149.63c  1.
m254  62147.63c  1.
m255  62149.63c  1.
m256  62150.63c  1.
m257  62151.63c  1.
m258  62152.63c  1.
m259  63153.63c  1.
m260  63154.63c  1.
m261  63155.63c  1.
m262  64155.92c  1.
m263  64156.92c  1.
m264  64157.92c  1.
c
c   Coatings and matrix mix
m2      6000.16c  7.633883E-03
        6000.15c  7.137042E-02
        14000.16c 1.175043E-03
mt2     grph.64t
c
c   Graphite (690 C-Scattering Kernel at 727 C)
m22     6000.14c  1.
mt22    grph.64t
c
c   Salt in the Core - 2LiF-BeF2 - (655 C)
m23     3006.14c  9.73386E-08
        3007.14c  2.38358E-02
        4009.14c  1.19185E-02
        9019.60c  4.76740E-02
c
c
c
c   TALLIES
c
c   begin_mocup_flux_tallies
c   time dependent flux
fc14    volume average flux tally
f14:n

```

```

      100
c    end_mocup_flux_tallies
c
c    begin_mocup_reaction_rate_tallies
c    time dependent reaction rates
fc114 Reaction rates
f114:n
      100
fm114 (1 101 (16) (17) (19:20) (102))$
      (1 102 (16) (17) (18) (102))$
      (1 103 (16) (17) (19:20) (102))$
      (1 104 (16) (17) (18) (102))$
      (1 105 (16) (17) (19:20) (102))$
      (1 106 (16) (17) (18) (102))$
      (1 107 (16) (17) (18) (102))$
      (1 108 (16) (17) (18) (102))$
      (1 109 (16) (17) (19:20) (102))$
      (1 110 (16) (17) (18) (102))$
      (1 111 (16) (17) (19:20) (102))$
      (1 112 (16) (17) (19:20) (102))$
      (1 113 (16) (17) (19:20) (102))$
      (1 114 (16) (17) (18) (102))$
      (1 115 (16) (17) (19:20) (102))$
      (1 116 (16) (17) (18) (102))$
      (1 117 (16) (17) (18) (102))$
      (1 118 (16) (17) (18) (102))$
      (1 119 (16) (17) (19:20) (102))$
      (1 120 (16) (17) (18) (102))$
      (1 121 (16) (17) (18) (102))$
      (1 122 (16) (17) (18) (102))$
      (1 123 (16) (17) (19:20) (102))$
      (1 124 (16) (17) (18) (102))$
      (1 125 (16) (17) (18) (102))$
      (1 126 (16) (17) (18) (102))$
      (1 127 (16) (17) (18) (102))$
      (1 128 (16) (17) (18) (102))$
      (1 129 (16) (17) (18) (102))$
      (1 130 (16) (17) (18) (102))$
      (1 131 (16) (17) (19:20) (102))$
      (1 132 (16) (17) (18) (102))$
      (1 133 (16) (17) (18) (102))$
      (1 134 (16) (17) (18) (102))$
      (1 201 (16) (17) (18) (102))$
      (1 202 (16) (17) (18) (102))$
      (1 203 (16) (17) (18) (102))$
      (1 204 (16) (17) (18) (102))$
      (1 205 (16) (17) (18) (102))$
      (1 206 (16) (17) (18) (102))$
      (1 207 (16) (17) (18) (102))$
      (1 208 (16) (17) (18) (102))$
      (1 209 (16) (17) (18) (102))$
      (1 210 (16) (17) (18) (102))$
      (1 211 (16) (17) (18) (102))$
      (1 212 (16) (17) (18) (102))$

```

(1	213			(102))\$
(1	214	(16)	(17)	(102))\$
(1	215	(16)	(17)	(102))\$
(1	216	(16)	(17)	(102))\$
(1	217	(16)		(102))\$
(1	218			(102))\$
(1	219	(16)	(17)	(102))\$
(1	220			(102))\$
(1	221	(16)	(17)	(102))\$
(1	222	(16)		(102))\$
(1	223			(102))\$
(1	224	(16)	(17)	(102))\$
(1	225			(102))\$
(1	226			(102))\$
(1	227	(16)	(17)	(102))\$
(1	228	(16)	(17)	(102))\$
(1	229	(16)	(17)	(102))\$
(1	230	(16)	(17)	(102))\$
(1	231	(16)	(17)	(102))\$
(1	232	(16)	(17)	(102))\$
(1	233			(102))\$
(1	234	(16)	(17)	(102))\$
(1	235	(16)	(17)	(102))\$
(1	236	(16)	(17)	(102))\$
(1	237			(102))\$
(1	238	(16)		(102))\$
(1	239			(102))\$
(1	240			(102))\$
(1	241			(102))\$
(1	242	(16)	(17)	(102))\$
(1	243	(16)	(17)	(102))\$
(1	244	(16)	(17)	(102))\$
(1	245	(16)	(17)	(102))\$
(1	246	(16)	(17)	(102))\$
(1	247	(16)	(17)	(102))\$
(1	248	(16)	(17)	(102))\$
(1	249	(16)	(17)	(102))\$
(1	250	(16)	(17)	(102))\$
(1	251	(16)	(17)	(102))\$
(1	252			(102))\$
(1	253			(102))\$
(1	254	(16)	(17)	(102))\$
(1	255	(16)	(17)	(102))\$
(1	256			(102))\$
(1	257	(16)	(17)	(102))\$
(1	258	(16)	(17)	(102))\$
(1	259	(16)	(17)	(102))\$
(1	260	(16)	(17)	(102))\$
(1	261	(16)	(17)	(102))\$
(1	262	(16)		(102))\$
(1	263	(16)		(102))\$
(1	264	(16)		(102))\$

c end_mocup_reaction_rate_tallies
c

```

c
c
kcode 100000 1.0 3 103
prtmp 103 103 103
ksrc 0. 0. 0.
print
mode n
c
c *****
c

```

Full core Modular PB-AHTR.

Modular Pebble Bed Advanced High Temperature Reactor

```

c
c ccccccccccccccccccccccccccccccccccccccccccccccccccccccccccccccc
c
c      Description: Modular PB-AHTR
c      Fuel Uranium Oxy-Carbide
c      Coolant Flibe (0.0004% Li-6)
c      TRISO Packing Factor 40.0%
c      Initial Enrichment 19.9%
c      Graphite Matrix Density 1.00 g/cc
c      Tallies: omitted
c      Author: Massimiliano Fratoni
c      Date: 00/00/0000
c
c ccccccccccccccccccccccccccccccccccccccccccccccccccccccccccccccc
c
c      Core
71  0      -71 61 62 63 64 65 66 -905 909
          701 702 703 704 705 706 707 708 709 710
          711 712 713 714 715 716 717 718 719 720
          721 722 723 724 725 726 727 728 729 730
          fill=1
72  0      -71 61 62 63 64 65 66 -901 904
          701 702 703 704 705 706 707 708 709 710
          711 712 713 714 715 716 717 718 719 720
          721 722 723 724 725 726 727 728 729 730
          fill=2
73  0      -71 61 62 63 64 65 66 -904 905
          701 702 703 704 705 706 707 708 709 710
          711 712 713 714 715 716 717 718 719 720
          721 722 723 724 725 726 727 728 729 730
          fill=3
          imp:n=1
c
c      Reflector
74  72 -1.74      -72 71 -901 909
          701 702 703 704 705 706 707 708 709 710
          711 712 713 714 715 716 717 718 719 720
          721 722 723 724 725 726 727 728 729 730
          tmp=7.52393E-08 imp:n=1

```

```

c
c   Control/shut-down rods
701 5 8.34284E-02 -701 -901 909 tmp=7.99787E-08 imp:n=1
702 5 8.34284E-02 -702 -901 909 tmp=7.99787E-08 imp:n=1
703 5 8.34284E-02 -703 -901 909 tmp=7.99787E-08 imp:n=1
704 5 8.34284E-02 -704 -901 909 tmp=7.99787E-08 imp:n=1
705 5 8.34284E-02 -705 -901 909 tmp=7.99787E-08 imp:n=1
706 5 8.34284E-02 -706 -901 909 tmp=7.99787E-08 imp:n=1
707 5 8.34284E-02 -707 -901 909 tmp=7.99787E-08 imp:n=1
708 5 8.34284E-02 -708 -901 909 tmp=7.99787E-08 imp:n=1
709 5 8.34284E-02 -709 -901 909 tmp=7.99787E-08 imp:n=1
710 5 8.34284E-02 -710 -901 909 tmp=7.99787E-08 imp:n=1
711 5 8.34284E-02 -711 -901 909 tmp=7.99787E-08 imp:n=1
712 5 8.34284E-02 -712 -901 909 tmp=7.99787E-08 imp:n=1
713 5 8.34284E-02 -713 -901 909 tmp=7.99787E-08 imp:n=1
714 5 8.34284E-02 -714 -901 909 tmp=7.99787E-08 imp:n=1
715 5 8.34284E-02 -715 -901 909 tmp=7.99787E-08 imp:n=1
716 5 8.34284E-02 -716 -901 909 tmp=7.99787E-08 imp:n=1
717 5 8.34284E-02 -717 -901 909 tmp=7.99787E-08 imp:n=1
718 5 8.34284E-02 -718 -901 909 tmp=7.99787E-08 imp:n=1
719 5 8.34284E-02 -719 -901 909 tmp=7.99787E-08 imp:n=1
720 5 8.34284E-02 -720 -901 909 tmp=7.99787E-08 imp:n=1
721 5 8.34284E-02 -721 -901 909 tmp=7.99787E-08 imp:n=1
722 5 8.34284E-02 -722 -901 909 tmp=7.99787E-08 imp:n=1
723 5 8.34284E-02 -723 -901 909 tmp=7.99787E-08 imp:n=1
724 5 8.34284E-02 -724 -901 909 tmp=7.99787E-08 imp:n=1
725 5 8.34284E-02 -725 -901 909 tmp=7.99787E-08 imp:n=1
726 5 8.34284E-02 -726 -901 909 tmp=7.99787E-08 imp:n=1
727 5 8.34284E-02 -727 -901 909 tmp=7.99787E-08 imp:n=1
728 5 8.34284E-02 -728 -901 909 tmp=7.99787E-08 imp:n=1
729 5 8.34284E-02 -729 -901 909 tmp=7.99787E-08 imp:n=1
730 5 8.34284E-02 -730 -901 909 tmp=7.99787E-08 imp:n=1
c
c   Shutdown rods
61 5 8.34284E-02 -61 -901 906 tmp=7.99787E-08 imp:n=1
610 51 -1.74 -61 -906 909 tmp=7.99787E-08 imp:n=1
62 5 8.34284E-02 -62 -901 906 tmp=7.99787E-08 imp:n=1
620 51 -1.74 -62 -906 909 tmp=7.99787E-08 imp:n=1
63 5 8.34284E-02 -63 -901 906 tmp=7.99787E-08 imp:n=1
630 51 -1.74 -63 -906 909 tmp=7.99787E-08 imp:n=1
64 5 8.34284E-02 -64 -901 906 tmp=7.99787E-08 imp:n=1
640 51 -1.74 -64 -906 909 tmp=7.99787E-08 imp:n=1
65 5 8.34284E-02 -65 -901 906 tmp=7.99787E-08 imp:n=1
650 51 -1.74 -65 -906 909 tmp=7.99787E-08 imp:n=1
66 5 8.34284E-02 -66 -901 906 tmp=7.99787E-08 imp:n=1
660 51 -1.74 -66 -906 909 tmp=7.99787E-08 imp:n=1
c
c   Module - Lower plenum
51 51 -1.74 -51 52 -53 54 -55 56 -905 909
u=1 tmp=7.99787E-08 imp:n=1
lat=2 fill=-2:2 -2:2 0:0
1 4r
1 1r 11 11 1
1 11 19 11 1

```

```

          1          11  11          1 1r
                                1 4r
c
c  Module - Upper plenum
52  51  -1.74          -51 52 -53 54 -55 56 -901 904
                                u=2    tmp=7.99787E-08 imp:n=1
      lat=2    fill=-2:2 -2:2 0:0
      2 4r
      2 1r      12  12      2
      2      12  20  12  2
      2      12  12      2 1r
                                2 4r
c
c  Module - Channels
53  51  -1.74          -51 52 -53 54 -55 56 -904 905
                                u=3      tmp=7.99787E-08
imp:n=1
      lat=2    fill=-2:2 -2:2 0:0
      3 4r
      3 1r      13  14      3
      3      15  21  16  3
      3      17  18      3 1r
                                3 4r
c
c  ----- Outer PCAs -----
c
c  Defueling chute
511 53  8.66354E-02  -40 -901 902          u=12          imp:n=1
c  Exit coolant flow channels
512 52  8.66354E-02   40 -901 902          u=12 tmp=8.38563E-08 imp:n=1
c  Upper pebble plenum
513 0          -57 -902 903          u=12          imp:n=1
      fill=126
c  Exit coolant flow channels
514 52  8.66354E-02   57 -902 903          u=12 tmp=8.38563E-08 imp:n=1
c  Upper pebble plenum
515 0          -58 -903 904          u=12          imp:n=1
      fill=126
c  Graphite structure
516 51  -1.74          58 -903 904          u=12 tmp=8.38563E-08 imp:n=1
c
c  Channels
541 0          -50 -904 905          u=13          imp:n=1
      fill=22
c
531 51  -1.74          -41 42 -43 44 -45 46          u=22          imp:n=1
      lat=2    fill=-3:3 -3:3 0:0
      22 6r
      22 2r      33  35  37      22
      22 1r      34  36  38  40  22
      22      33  36  39  41  42  22
      22      35  38  41  43      22 1r
      22      37  40  42      22 2r
                                22 6r

```

c Channels							
542	0		-50 -904 905		u=14		imp:n=1
			fill=23				
532	51	-1.74	-41 42 -43 44 -45 46		u=23		imp:n=1
		lat=2	fill=-3:3 -3:3 0:0				
		23	6r				
		23	2r	33 35 37		23	
		23	1r	34 36 38 40		23	
		23		33 36 39 41 42		23	
		23		35 38 41 43		23 1r	
		23		37 40 42		23 2r	
						23 6r	
c Channels							
543	0		-50 -904 905		u=15		imp:n=1
			fill=24				
533	51	-1.74	-41 42 -43 44 -45 46		u=24		imp:n=1
		lat=2	fill=-3:3 -3:3 0:0				
		24	6r				
		24	2r	33 35 37		24	
		24	1r	34 36 38 40		24	
		24		33 36 39 41 42		24	
		24		35 38 41 43		24 1r	
		24		37 40 42		24 2r	
						24 6r	
c Channels							
544	0		-50 -904 905		u=16		imp:n=1
			fill=25				
534	51	-1.74	-41 42 -43 44 -45 46		u=25		imp:n=1
		lat=2	fill=-3:3 -3:3 0:0				
		25	6r				
		25	2r	33 35 37		25	
		25	1r	34 36 38 40		25	
		25		33 36 39 41 42		25	
		25		35 38 41 43		25 1r	
		25		37 40 42		25 2r	
						25 6r	
c Channels							
545	0		-50 -904 905		u=17		imp:n=1
			fill=26				
535	51	-1.74	-41 42 -43 44 -45 46		u=26		imp:n=1
		lat=2	fill=-3:3 -3:3 0:0				
		26	6r				
		26	2r	33 35 37		26	
		26	1r	34 36 38 40		26	
		26		33 36 39 41 42		26	
		26		35 38 41 43		26 1r	
		26		37 40 42		26 2r	
						26 6r	
c Channels							
546	0		-50 -904 905		u=18		imp:n=1
			fill=27				
536	51	-1.74	-41 42 -43 44 -45 46		u=27		imp:n=1
		lat=2	fill=-3:3 -3:3 0:0				
		27	6r				

	27	2r		33	35	37		27	
	27	1r		34	36	38	40	27	
	27		33	36	39	41	42	27	
	27			35	38	41	43	27	1r
	27				37	40	42	27	2r
								27	6r
c									
c	Fuel Channels - Zone 1								
413	0			-40				u=33	imp:n=1
				fill=136					
443	51	-1.74		40				u=33 tmp=7.99787E-08	imp:n=1
c	Fuel Channels - Zone 2								
414	0			-40				u=34	imp:n=1
				fill=146					
444	51	-1.74		40				u=34 tmp=7.99787E-08	imp:n=1
c	Fuel Channels - Zone 3								
415	0			-40				u=35	imp:n=1
				fill=156					
445	51	-1.74		40				u=35 tmp=7.99787E-08	imp:n=1
c	Fuel Channels - Zone 4								
416	0			-40				u=36	imp:n=1
				fill=166					
446	51	-1.74		40				u=36 tmp=7.99787E-08	imp:n=1
c	Fuel Channels - Zone 5								
417	0			-40				u=37	imp:n=1
				fill=176					
447	51	-1.74		40				u=37 tmp=7.99787E-08	imp:n=1
c	Fuel Channels - Zone 6								
418	0			-40				u=38	imp:n=1
				fill=186					
448	51	-1.74		40				u=38 tmp=7.99787E-08	imp:n=1
c	Fuel Channels - Zone 7								
419	0			-40				u=39	imp:n=1
				fill=196					
449	51	-1.74		40				u=39 tmp=7.99787E-08	imp:n=1
c	Fuel Channels - Zone 8								
420	0			-40				u=40	imp:n=1
				fill=206					
450	51	-1.74		40				u=40 tmp=7.99787E-08	imp:n=1
c	Fuel Channels - Zone 9								
421	0			-40				u=41	imp:n=1
				fill=216					
451	51	-1.74		40				u=41 tmp=7.99787E-08	imp:n=1
c	Fuel Channels - Zone 10								
422	0			-40				u=42	imp:n=1
				fill=226					
452	51	-1.74		40				u=42 tmp=7.99787E-08	imp:n=1
c	Fuel Channels - Zone 11								
423	0			-40				u=43	imp:n=1
				fill=236					
453	51	-1.74		40				u=43 tmp=7.99787E-08	imp:n=1
c									
c	Lower pebble plenum								
519	0			-59	-905	906		u=11	imp:n=1

```

                                fill=116
c   Graphite structure
520 51 -1.74          59 -905 906          u=11 tmp=7.52393E-08 imp:n=1
c   Salt plenum
521 5  8.34284E-02   -59 -906 907          u=11 tmp=7.52393E-08 imp:n=1
c   Graphite structure
522 51 -1.74          59 -906 907          u=11 tmp=7.52393E-08 imp:n=1
c   Salt plenum
523 5  8.34284E-02   -60 -907 908          u=11 tmp=7.52393E-08 imp:n=1
c   Graphite structure
524 51 -1.74          60 -907 908          u=11 tmp=7.52393E-08 imp:n=1
c   Coolant inlet
525 5  8.34284E-02   -40 -908 909          u=11 tmp=7.52393E-08 imp:n=1
c   Graphite structure
526 51 -1.74          40 -908 909          u=11 tmp=7.52393E-08 imp:n=1
c
c   ----- Central PCA -----
c
c   Defueling chute
571 53 8.66354E-02   -40 -901 902          u=20          imp:n=1
c   Exit coolant flow channels
572 52 8.66354E-02   40 -901 902          u=20 tmp=8.38563E-08 imp:n=1
c   Upper pebble plenum
573 0          -57 -902 903          u=20          imp:n=1
                                fill=326
c   Exit coolant flow channels
574 52 8.66354E-02   57 -902 903          u=20 tmp=8.38563E-08 imp:n=1
c   Upper pebble plenum
575 0          -58 -903 904          u=20          imp:n=1
                                fill=326
c   Graphite structure
576 51 -1.74          58 -903 904          u=20 tmp=8.38563E-08 imp:n=1
c   Channels region
577 0          -50 -904 905          u=21          imp:n=1
                                fill=71
c
578 51 -1.74          -41 42 -43 44 -45 46          u=71          imp:n=1
    lat=2    fill=-3:3 -3:3 0:0
          71 6r
          71 2r          73 73 73          71
          71 1r          73 74 74 73          71
          71          73 74 75 74 73 71
          71          73 74 74 73          71 1r
          71          73 73 73          71 2r
                                71 6r
c
c   Fuel Channels - Zone 1c
463 0          -40          u=73          imp:n=1
                                fill=336
493 51 -1.74          40          u=73 tmp=7.99787E-08 imp:n=1
c   Fuel Channels - Zone 2c
464 0          -40          u=74          imp:n=1
                                fill=346
494 51 -1.74          40          u=74 tmp=7.99787E-08 imp:n=1

```

```

c   Fuel Channels - Zone 3c
465 0          -40          u=75          imp:n=1
      fill=356
495 51 -1.74      40          u=75 tmp=7.99787E-08 imp:n=1
c
c   Lower pebble plenum
579 0          -59 -905 906    u=19          imp:n=1
      fill=316
c   Graphite structure
580 51 -1.74      59 -905 906    u=19 tmp=7.52393E-08 imp:n=1
c   Salt plenum
581 5  8.34284E-02 -59 -906 907    u=19 tmp=7.52393E-08 imp:n=1
c   Graphite structure
582 51 -1.74      59 -906 907    u=19 tmp=7.52393E-08 imp:n=1
c   Salt plenum
583 5  8.34284E-02 -60 -907 908    u=19 tmp=7.52393E-08 imp:n=1
c   Graphite structure
584 51 -1.74      60 -907 908    u=19 tmp=7.52393E-08 imp:n=1
c   Coolant inlet
585 5  8.34284E-02 -40 -908 909    u=19 tmp=7.52393E-08 imp:n=1
c   Graphite structure
586 51 -1.74      40 -908 909    u=19 tmp=7.52393E-08 imp:n=1
c
c   ----- Zone 1: lower plenum, outer PCAs -----
c
c   Pebbles Lattice
118 0          -31 32 -33 34 -35 36 -37 38
      lat=2    fill=117          u=116          imp:n=1
c
c   Pebble
114 3 -1.          -21          u=117 tmp=9.24733E-08 imp:n=1
115 0          -22 21          u=117          imp:n=1
      fill=118
116 4 -1.74      -23 22          u=117 tmp=8.29946E-08 imp:n=1
117 5  8.34284E-02 23          u=117 tmp=7.99787E-08 imp:n=1
c
c   TRISO particles lattice - Simple Cubic
113 0          -11 12 -13 14 -15 16
      lat=1    fill=119          u=118          imp:n=1
c
c   TRISO particles components
111 11 7.077220E-02 -1          u=119 tmp=9.24733E-08 imp:n=1
112 2  6.183102E-02 1          u=119 tmp=8.81648E-08 imp:n=1
c
c   ----- Zone 2: upper plenum, outer PCAs -----
c
c   Pebbles Lattice
128 0          -31 32 -33 34 -35 36 -37 38
      lat=2    fill=127          u=126          imp:n=1
c
c   Pebble
124 3 -1.          -21          u=127 tmp=9.24733E-08 imp:n=1
125 0          -22 21          u=127          imp:n=1
      fill=128

```

```

126 4 -1.74 -23 22 u=127 tmp=8.29946E-08 imp:n=1
127 5 8.34284E-02 23 u=127 tmp=7.99787E-08 imp:n=1
c
c TRISO particles lattice - Simple Cubic
123 0 -11 12 -13 14 -15 16
lat=1 fill=129 u=128 imp:n=1
c
c TRISO particles components
121 12 7.077220E-02 -1 u=129 tmp=9.24733E-08 imp:n=1
122 2 6.183102E-02 1 u=129 tmp=8.81648E-08 imp:n=1
c
c ----- Zone 3: channels 1, outer PCAs -----
c
c Pebbles Lattice
138 0 -31 32 -33 34 -35 36 -37 38
lat=2 fill=137 u=136 imp:n=1
c
c Pebble
134 3 -1. -21 u=137 tmp=9.24733E-08 imp:n=1
135 0 -22 21 u=137 imp:n=1
fill=138
136 4 -1.74 -23 22 u=137 tmp=8.29946E-08 imp:n=1
137 5 8.34284E-02 23 u=137 tmp=7.99787E-08 imp:n=1
c
c TRISO particles lattice - Simple Cubic
133 0 -11 12 -13 14 -15 16
lat=1 fill=139 u=138 imp:n=1
c
c TRISO particles components
131 13 7.077220E-02 -1 u=139 tmp=9.24733E-08 imp:n=1
132 2 6.183102E-02 1 u=139 tmp=8.81648E-08 imp:n=1
c
c ----- Zone 3: channels 2, outer PCAs -----
c
c Pebbles Lattice
148 0 -31 32 -33 34 -35 36 -37 38
lat=2 fill=147 u=146 imp:n=1
c
c Pebble
144 3 -1. -21 u=147 tmp=9.24733E-08 imp:n=1
145 0 -22 21 u=147 imp:n=1
fill=148
146 4 -1.74 -23 22 u=147 tmp=8.29946E-08 imp:n=1
147 5 8.34284E-02 23 u=147 tmp=7.99787E-08 imp:n=1
c
c TRISO particles lattice - Simple Cubic
143 0 -11 12 -13 14 -15 16
lat=1 fill=149 u=148 imp:n=1
c
c TRISO particles components
141 14 7.077220E-02 -1 u=149 tmp=9.24733E-08 imp:n=1
142 2 6.183102E-02 1 u=149 tmp=8.81648E-08 imp:n=1
c
c ----- Zone 3: channels 3, outer PCAs -----

```

```

c
c Pebbles Lattice
158 0 -31 32 -33 34 -35 36 -37 38
      lat=2 fill=157 u=156 imp:n=1
c
c Pebble
154 3 -1. -21 u=157 tmp=9.24733E-08 imp:n=1
155 0 -22 21 u=157 imp:n=1
      fill=158
156 4 -1.74 -23 22 u=157 tmp=8.29946E-08 imp:n=1
157 5 8.34284E-02 23 u=157 tmp=7.99787E-08 imp:n=1
c
c TRISO particles lattice - Simple Cubic
153 0 -11 12 -13 14 -15 16
      lat=1 fill=159 u=158 imp:n=1
c
c TRISO particles components
151 15 7.077220E-02 -1 u=159 tmp=9.24733E-08 imp:n=1
152 2 6.183102E-02 1 u=159 tmp=8.81648E-08 imp:n=1
c
c ----- Zone 3: channels 4, outer PCAs -----
c
c Pebbles Lattice
168 0 -31 32 -33 34 -35 36 -37 38
      lat=2 fill=167 u=166 imp:n=1
c
c Pebble
164 3 -1. -21 u=167 tmp=9.24733E-08 imp:n=1
165 0 -22 21 u=167 imp:n=1
      fill=168
166 4 -1.74 -23 22 u=167 tmp=8.29946E-08 imp:n=1
167 5 8.34284E-02 23 u=167 tmp=7.99787E-08 imp:n=1
c
c TRISO particles lattice - Simple Cubic
163 0 -11 12 -13 14 -15 16
      lat=1 fill=169 u=168 imp:n=1
c
c TRISO particles components
161 16 7.077220E-02 -1 u=169 tmp=9.24733E-08 imp:n=1
162 2 6.183102E-02 1 u=169 tmp=8.81648E-08 imp:n=1
c
c ----- Zone 3: channels 5, outer PCAs -----
c
c Pebbles Lattice
178 0 -31 32 -33 34 -35 36 -37 38
      lat=2 fill=177 u=176 imp:n=1
c
c Pebble
174 3 -1. -21 u=177 tmp=9.24733E-08 imp:n=1
175 0 -22 21 u=177 imp:n=1
      fill=178
176 4 -1.74 -23 22 u=177 tmp=8.29946E-08 imp:n=1
177 5 8.34284E-02 23 u=177 tmp=7.99787E-08 imp:n=1
c

```

```

c  TRISO particles lattice - Simple Cubic
173 0          -11 12 -13 14 -15 16
      lat=1    fill=179                      u=178                      imp:n=1
c
c  TRISO particles components
171 17 7.077220E-02 -1                      u=179 tmp=9.24733E-08 imp:n=1
172 2 6.183102E-02 1                        u=179 tmp=8.81648E-08 imp:n=1
c
c  ----- Zone 3: channels 6, outer PCAs -----
c
c  Pebbles Lattice
188 0          -31 32 -33 34 -35 36 -37 38
      lat=2    fill=187                      u=186                      imp:n=1
c
c  Pebble
184 3 -1.          -21                      u=187 tmp=9.24733E-08 imp:n=1
185 0          -22 21                      u=187                      imp:n=1
      fill=188
186 4 -1.74        -23 22                  u=187 tmp=8.29946E-08 imp:n=1
187 5 8.34284E-02 23                      u=187 tmp=7.99787E-08 imp:n=1
c
c  TRISO particles lattice - Simple Cubic
183 0          -11 12 -13 14 -15 16
      lat=1    fill=189                      u=188                      imp:n=1
c
c  TRISO particles components
181 18 7.077220E-02 -1                      u=189 tmp=9.24733E-08 imp:n=1
182 2 6.183102E-02 1                        u=189 tmp=8.81648E-08 imp:n=1
c
c  ----- Zone 3: channels 7, outer PCAs -----
c
c  Pebbles Lattice
198 0          -31 32 -33 34 -35 36 -37 38
      lat=2    fill=197                      u=196                      imp:n=1
c
c  Pebble
194 3 -1.          -21                      u=197 tmp=9.24733E-08 imp:n=1
195 0          -22 21                      u=197                      imp:n=1
      fill=198
196 4 -1.74        -23 22                  u=197 tmp=8.29946E-08 imp:n=1
197 5 8.34284E-02 23                      u=197 tmp=7.99787E-08 imp:n=1
c
c  TRISO particles lattice - Simple Cubic
193 0          -11 12 -13 14 -15 16
      lat=1    fill=199                      u=198                      imp:n=1
c
c  TRISO particles components
191 19 7.077220E-02 -1                      u=199 tmp=9.24733E-08 imp:n=1
192 2 6.183102E-02 1                        u=199 tmp=8.81648E-08 imp:n=1
c
c  ----- Zone 3: channels 8, outer PCAs -----
c
c  Pebbles Lattice
208 0          -31 32 -33 34 -35 36 -37 38

```

```

      lat=2   fill=207                                u=206                imp:n=1
c
c   Pebble
204 3 -1.                -21                u=207 tmp=9.24733E-08 imp:n=1
205 0                    -22 21            u=207                imp:n=1
      fill=208
206 4 -1.74              -23 22            u=207 tmp=8.29946E-08 imp:n=1
207 5 8.34284E-02        23                u=207 tmp=7.99787E-08 imp:n=1
c
c   TRISO particles lattice - Simple Cubic
203 0                    -11 12 -13 14 -15 16
      lat=1   fill=209                                u=208                imp:n=1
c
c   TRISO particles components
201 20 7.077220E-02 -1                u=209 tmp=9.24733E-08 imp:n=1
202 2 6.183102E-02 1                  u=209 tmp=8.81648E-08 imp:n=1
c
c   ----- Zone 3: channels 9, outer PCAs -----
c
c   Pebbles Lattice
218 0                    -31 32 -33 34 -35 36 -37 38
      lat=2   fill=217                                u=216                imp:n=1
c
c   Pebble
214 3 -1.                -21                u=217 tmp=9.24733E-08 imp:n=1
215 0                    -22 21            u=217                imp:n=1
      fill=218
216 4 -1.74              -23 22            u=217 tmp=8.29946E-08 imp:n=1
217 5 8.34284E-02        23                u=217 tmp=7.99787E-08 imp:n=1
c
c   TRISO particles lattice - Simple Cubic
213 0                    -11 12 -13 14 -15 16
      lat=1   fill=219                                u=218                imp:n=1
c
c   TRISO particles components
211 21 7.077220E-02 -1                u=219 tmp=9.24733E-08 imp:n=1
212 2 6.183102E-02 1                  u=219 tmp=8.81648E-08 imp:n=1
c
c   ----- Zone 3: channels 10, outer PCAs -----
c
c   Pebbles Lattice
228 0                    -31 32 -33 34 -35 36 -37 38
      lat=2   fill=227                                u=226                imp:n=1
c
c   Pebble
224 3 -1.                -21                u=227 tmp=9.24733E-08 imp:n=1
225 0                    -22 21            u=227                imp:n=1
      fill=228
226 4 -1.74              -23 22            u=227 tmp=8.29946E-08 imp:n=1
227 5 8.34284E-02        23                u=227 tmp=7.99787E-08 imp:n=1
c
c   TRISO particles lattice - Simple Cubic
223 0                    -11 12 -13 14 -15 16
      lat=1   fill=229                                u=228                imp:n=1

```

```

c
c  TRISO particles components
221 22 7.077220E-02 -1          u=229 tmp=9.24733E-08 imp:n=1
222 2 6.183102E-02 1          u=229 tmp=8.81648E-08 imp:n=1
c
c  ----- Zone 3: channels 11, outer PCAs -----
c
c  Pebbles Lattice
238 0          -31 32 -33 34 -35 36 -37 38
    lat=2    fill=237          u=236          imp:n=1
c
c  Pebble
234 3 -1.          -21          u=237 tmp=9.24733E-08 imp:n=1
235 0          -22 21          u=237          imp:n=1
    fill=238
236 4 -1.74        -23 22          u=237 tmp=8.29946E-08 imp:n=1
237 5 8.34284E-02 23          u=237 tmp=7.99787E-08 imp:n=1
c
c  TRISO particles lattice - Simple Cubic
233 0          -11 12 -13 14 -15 16
    lat=1    fill=239          u=238          imp:n=1
c
c  TRISO particles components
231 23 7.077220E-02 -1          u=239 tmp=9.24733E-08 imp:n=1
232 2 6.183102E-02 1          u=239 tmp=8.81648E-08 imp:n=1
c
c  ----- Zone 1c: lower plenum, inner PCAs -----
c
c  Pebbles Lattice
318 0          -31 32 -33 34 -35 36 -37 38
    lat=2    fill=317          u=316          imp:n=1
c
c  Pebble
314 3 -1.          -21          u=317 tmp=9.24733E-08 imp:n=1
315 0          -22 21          u=317          imp:n=1
    fill=318
316 4 -1.74        -23 22          u=317 tmp=8.29946E-08 imp:n=1
317 5 8.34284E-02 23          u=317 tmp=7.99787E-08 imp:n=1
c
c  TRISO particles lattice - Simple Cubic
313 0          -11 12 -13 14 -15 16
    lat=1    fill=319          u=318          imp:n=1
c
c  TRISO particles components
311 31 7.077220E-02 -1          u=319 tmp=9.24733E-08 imp:n=1
312 2 6.183102E-02 1          u=319 tmp=8.81648E-08 imp:n=1
c
c  ----- Zone 2c: upper plenum, inner PCAs -----
c
c  Pebbles Lattice
328 0          -31 32 -33 34 -35 36 -37 38
    lat=2    fill=327          u=326          imp:n=1
c
c  Pebble

```

```

324 3 -1.          -21          u=327 tmp=9.24733E-08 imp:n=1
325 0              -22 21      u=327          imp:n=1
              fill=328
326 4 -1.74        -23 22      u=327 tmp=8.29946E-08 imp:n=1
327 5 8.34284E-02  23          u=327 tmp=7.99787E-08 imp:n=1
c
c  TRISO particles lattice - Simple Cubic
323 0              -11 12 -13 14 -15 16
      lat=1    fill=329          u=328          imp:n=1
c
c  TRISO particles components
321 32 7.077220E-02 -1          u=329 tmp=9.24733E-08 imp:n=1
322 2 6.183102E-02  1          u=329 tmp=8.81648E-08 imp:n=1
c
c  ----- Zone 3c: channels 1, inner PCAs -----
c
c  Pebbles Lattice
338 0              -31 32 -33 34 -35 36 -37 38
      lat=2    fill=337          u=336          imp:n=1
c
c  Pebble
334 3 -1.          -21          u=337 tmp=9.24733E-08 imp:n=1
335 0              -22 21      u=337          imp:n=1
              fill=338
336 4 -1.74        -23 22      u=337 tmp=8.29946E-08 imp:n=1
337 5 8.34284E-02  23          u=337 tmp=7.99787E-08 imp:n=1
c
c  TRISO particles lattice - Simple Cubic
333 0              -11 12 -13 14 -15 16
      lat=1    fill=339          u=338          imp:n=1
c
c  TRISO particles components
331 33 7.077220E-02 -1          u=339 tmp=9.24733E-08 imp:n=1
332 2 6.183102E-02  1          u=339 tmp=8.81648E-08 imp:n=1
c
c  ----- Zone 3c: channels 2, inner PCAs -----
c
c  Pebbles Lattice
348 0              -31 32 -33 34 -35 36 -37 38
      lat=2    fill=347          u=346          imp:n=1
c
c  Pebble
344 3 -1.          -21          u=347 tmp=9.24733E-08 imp:n=1
345 0              -22 21      u=347          imp:n=1
              fill=348
346 4 -1.74        -23 22      u=347 tmp=8.29946E-08 imp:n=1
347 5 8.34284E-02  23          u=347 tmp=7.99787E-08 imp:n=1
c
c  TRISO particles lattice - Simple Cubic
343 0              -11 12 -13 14 -15 16
      lat=1    fill=349          u=348          imp:n=1
c
c  TRISO particles components
341 34 7.077220E-02 -1          u=349 tmp=9.24733E-08 imp:n=1

```

```

342 2 6.183102E-02 1 u=349 tmp=8.81648E-08 imp:n=1
c
c ----- Zone 3c: channels 3, inner PCAs -----
c
c Pebbles Lattice
358 0 -31 32 -33 34 -35 36 -37 38
lat=2 fill=357 u=356 imp:n=1
c
c Pebble
354 3 -1. -21 u=357 tmp=9.24733E-08 imp:n=1
355 0 -22 21 u=357 imp:n=1
fill=358
356 4 -1.74 -23 22 u=357 tmp=8.29946E-08 imp:n=1
357 5 8.34284E-02 23 u=357 tmp=7.99787E-08 imp:n=1
c
c TRISO particles lattice - Simple Cubic
353 0 -11 12 -13 14 -15 16
lat=1 fill=359 u=358 imp:n=1
c
c TRISO particles components
351 35 7.077220E-02 -1 u=359 tmp=9.24733E-08 imp:n=1
352 2 6.183102E-02 1 u=359 tmp=8.81648E-08 imp:n=1
c
c -----
c
c External
99 0 72:901:-909 imp:n=0
c
c *****
c
c SURFACES
c
c Fuel: TRISO Layers
1 so 1.625E-02 $ Kernel
c
c Fuel Particles Lattice
11 px 4.02010E-02
12 px -4.02010E-02
13 py 4.02010E-02
14 py -4.02010E-02
15 pz 4.02010E-02
16 pz -4.02010E-02
c
c Pebble
21 so 0.80
22 so 1.25
23 so 1.50
c
c Pebbles Lattice
31 px 1.50382
32 px -1.50382
33 p 1. 1.732050808 0. 3.00765
34 p 1. 1.732050808 0. -3.00765

```

```

35 p    -1.  1.732050808  0.   3.00765
36 p    -1.  1.732050808  0.  -3.00765
37 pz    1.50382
38 pz   -1.50382
c
c  Fuel channel
40 cz    9.9
c  Fuel channel lattice
41 p    1.732050808  1.  0.   25.
42 p    1.732050808  1.  0.  -25.
43 py   12.5
44 py  -12.5
45 p   -1.732050808  1.  0.   25.
46 p   -1.732050808  1.  0.  -25.
c
c  Module
50 cz   73.
51 px   62.5
52 px  -62.5
53 p    1.  1.732050808  0.   125.
54 p    1.  1.732050808  0.  -125.
55 p   -1.  1.732050808  0.   125.
56 p   -1.  1.732050808  0.  -125.
57 kz  475.  0.33333
58 kz  531.  0.10890
59 kz -226.  0.02000
60 kz   15.2 0.44646
c
c  Control rods
61 c/z  62.5  58.25  9.9
62 c/z  81.7 -25.    9.9
63 c/z  19.2 -83.25  9.9
64 c/z -62.5 -58.25  9.9
65 c/z -81.7  25.    9.9
66 c/z -19.2  83.25  9.9
c
c  Control/shut-down rods
701 c/z  43.3 184.24  9.9
702 c/z  81.7 184.24  9.9
703 c/z 125.  159.24  9.9
704 c/z 139.9 130.77  9.9
705 c/z 139.9  80.77  9.9
706 c/z 183.2  55.77  9.9
707 c/z 202.4  25.    9.9
708 c/z 202.4 -25.    9.9
709 c/z 183.2 -55.77  9.9
710 c/z 139.9 -80.77  9.9
711 c/z 139.9 -130.77 9.9
712 c/z 125.  -159.24 9.9
713 c/z  81.7 -184.24 9.9
714 c/z  43.3 -184.24 9.9
715 c/z   0.  -159.24 9.9
716 c/z -43.3 -184.24 9.9
717 c/z -81.7 -184.24 9.9

```

```

718 c/z -125.  -159.24  9.9
719 c/z -139.9 -130.77  9.9
720 c/z -139.9  -80.77  9.9
721 c/z -183.2  -55.77  9.9
722 c/z -202.4  -25.    9.9
723 c/z -202.4   25.    9.9
724 c/z -183.2   55.77  9.9
725 c/z -139.9   80.77  9.9
726 c/z -139.9  130.77  9.9
727 c/z -125.   159.24  9.9
728 c/z  -81.7  184.24  9.9
729 c/z  -43.3  184.24  9.9
730 c/z    0.   159.24  9.9
c
c   Core
71  cz  192.
72  cz  300.
c
c   Axial levels
901 pz  501.  $ Coolant outflow
902 pz  458.8 $ Defueling chute's base
903 pz  400.  $ Top cone to defueling chute
904 pz  370.  $ Channels' top
941 pz  326.
942 pz  282.
943 pz  238.
944 pz  194.
905 pz  150.  $ Channels' bottom
906 pz  100.  $ Bottom of pebble bed
907 pz   80.  $ Base of lower cone
908 pz   30.  $ Inlet leg's top
909 pz    0.  $ Base
c
c   Channels' depletion zones
911 pz  296.667
912 pz  223.333
c

c *****
c
c   MATERIALS
c
c   Fuel (800 C) - Zone 1
m11    6000.16c 1.179536E-02
        8016.16c 3.538608E-02
        92234.92c 3.586117E-05
        92235.94c 4.694553E-03
        92238.94c 1.886031E-02
c
c   Fuel (800 C) - Zone 2
m12    6000.16c 1.179536E-02
        8016.16c 3.538608E-02
        92234.92c 3.586117E-05
        92235.94c 4.694553E-03

```

```

          92238.94c 1.886031E-02
c
c   Fuel (800 C) - Zone 3
m13    6000.16c 1.179536E-02
        8016.16c 3.538608E-02
        92234.92c 3.586117E-05
        92235.94c 4.694553E-03
        92238.94c 1.886031E-02

c
c   Fuel (800 C) - Zone 4
m14    6000.16c 1.179536E-02
        8016.16c 3.538608E-02
        92234.92c 3.586117E-05
        92235.94c 4.694553E-03
        92238.94c 1.886031E-02

c
c   Fuel (800 C) - Zone 5
m15    6000.16c 1.179536E-02
        8016.16c 3.538608E-02
        92234.92c 3.586117E-05
        92235.94c 4.694553E-03
        92238.94c 1.886031E-02

c
c   Fuel (800 C) - Zone 6
m16    6000.16c 1.179536E-02
        8016.16c 3.538608E-02
        92234.92c 3.586117E-05
        92235.94c 4.694553E-03
        92238.94c 1.886031E-02

c
c   Fuel (800 C) - Zone 7
m17    6000.16c 1.179536E-02
        8016.16c 3.538608E-02
        92234.92c 3.586117E-05
        92235.94c 4.694553E-03
        92238.94c 1.886031E-02

c   Fuel (800 C) - Zone 8
m18    6000.16c 1.179536E-02
        8016.16c 3.538608E-02
        92234.92c 3.586117E-05
        92235.94c 4.694553E-03
        92238.94c 1.886031E-02

c   Fuel (800 C) - Zone 9
m19    6000.16c 1.179536E-02
        8016.16c 3.538608E-02
        92234.92c 3.586117E-05
        92235.94c 4.694553E-03
        92238.94c 1.886031E-02

c
c   Fuel (800 C) - Zone 10
m20    6000.16c 1.179536E-02
        8016.16c 3.538608E-02
        92234.92c 3.586117E-05
        92235.94c 4.694553E-03

```

```

          92238.94c 1.886031E-02
c   Fuel (800 C) - Zone 11
m21    6000.16c 1.179536E-02
        8016.16c 3.538608E-02
        92234.92c 3.586117E-05
        92235.94c 4.694553E-03
        92238.94c 1.886031E-02
c   Fuel (800 C) - Zone 12
m22    6000.16c 1.179536E-02
        8016.16c 3.538608E-02
        92234.92c 3.586117E-05
        92235.94c 4.694553E-03
        92238.94c 1.886031E-02
c   Fuel (800 C) - Zone 13
m23    6000.16c 1.179536E-02
        8016.16c 3.538608E-02
        92234.92c 3.586117E-05
        92235.94c 4.694553E-03
        92238.94c 1.886031E-02

c
c
c   Fuel (800 C) - Zone 1c
m31    6000.16c 1.179536E-02
        8016.16c 3.538608E-02
        92234.92c 3.586117E-05
        92235.94c 4.694553E-03
        92238.94c 1.886031E-02

c
c   Fuel (800 C) - Zone 2c
m32    6000.16c 1.179536E-02
        8016.16c 3.538608E-02
        92234.92c 3.586117E-05
        92235.94c 4.694553E-03
        92238.94c 1.886031E-02

c
c   Fuel (800 C) - Zone 3c
m33    6000.16c 1.179536E-02
        8016.16c 3.538608E-02
        92234.92c 3.586117E-05
        92235.94c 4.694553E-03
        92238.94c 1.886031E-02

c
c   Fuel (800 C) - Zone 4c
m34    6000.16c 1.179536E-02
        8016.16c 3.538608E-02
        92234.92c 3.586117E-05
        92235.94c 4.694553E-03
        92238.94c 1.886031E-02

c
c   Fuel (800 C) - Zone 5c
m35    6000.16c 1.179536E-02
        8016.16c 3.538608E-02
        92234.92c 3.586117E-05
        92235.94c 4.694553E-03

```

```

          92238.94c 1.886031E-02
c
c   Coatings and matrix mix
m2      6000.16c 2.648600E-02
          6000.15c 3.116077E-02
          14000.16c 4.184244E-03
mt2     grph.64t
c
c   Graphite in the pebble core
m3      6000.16c 1.
mt3     grph.64t
c
c   Graphite in the pebble outer layer
m4      6000.14c 1.
mt4     grph.64t
c
c   Salt in the Core - 2LiF-BeF2 - (655 C)
m5      3006.14c 9.73386E-08
          3007.14c 2.38358E-02
          4009.14c 1.19185E-02
          9019.14c 4.76740E-02
c
c   Graphite in the structure
m51     6000.13c 1.
mt51    grph.73t
c
c   Graphite-salt (84-16) mix in the exit coolant flow channels region
m52     6000.15c 7.32869E-02
          3006.15c 1.55742E-08
          3007.15c 3.81373E-03
          4009.15c 1.90696E-03
          9019.15c 7.62784E-03
mt52    grph.64t
c
c   Graphite-salt (55-45) mix in the defueling chute
m53     6000.15c 7.32869E-02
          3006.15c 1.55742E-08
          3007.15c 3.81373E-03
          4009.15c 1.90696E-03
          9019.15c 7.62784E-03
mt53    grph.64t
c
c   Graphite in the reflector
m72     6000.12c 1.
mt72    grph.63t
c
c
c
c
kcode 2e6 1.0 5 155
print
mode n
c
c *****
c

```
